Journal of Science & Technology in the Tropics

Volume 5 Number 2 Dec 2009

JOSTT

DEDICATED TO THE ADVANCEMENT OF SCIENCE AND TECHNOLOGY RELATED TO THE TROPICS

Journal of Science & Technology in the Tropics

Volume 5 Number 2
Dec 2009
ISSN 1823-5034

Journal of Science & Technology in the Tropics Volume 5 Number 2 Dec 2009

CONTENTS

22	*Rhacophorus nigropalmatus*	1	-	Branches of small trees near forest trail	NP
23	*R. tunkui*	1	-	Branches of small tree along trails. (1 VSC)	NP
24	*Theloderma licin*	2	-	Tree trunk near nesting hole. (2 VSC)	NP
25	*Nyctixalus pictus*	1	-	On branch near stream. (1 VSC)	NP
	Microhylidae				
26	*Microhyla heymonsi*	-	1	Forest trail. Released.	NP
27	*Kalophrynus pleurostigma*	1	2	Forest floor near puddles. (1 VSC)	NP
	REPTILIA				
	LIZARDS				
	Agamidae				
28	*Aphaniotis fusca*	2	2	Branches of small plants. Released.	NP
29	*Bronchocela cristatella*	1	2	Branch of small plant. Released.	NP
30	*Draco (volans) sumatranus*	1	1	On tree trunk, using blow pipe by orang asli. (1 VSC)	NP
31	*D. melanopogon*	1	1	(1 VSC)	NP
32	*D. maximus*	-	1	(1 VSC)	NP
33	*Gonocephalus grandis*	1	-	On tree trunk near forest stream. Released.	NP
34	*G. bellii*	-	1	On tree trunk in forest (1 VSC)	NP
	Scincidae				
35	*Eutrophis multifasciata*	1	-	On forest floor. Released.	NP
36	*E. refigera*	1	-	On forest floor. (1 VSC)	NP
	Gekkonidae				
37	*Gekko smithii*	1	2	On tree trunks. Released.	NP
38	*Cyrtodactylus consobrinus*	2	2	On tree trunks. Released.	NP
39	*C. quadrivirgatus*	5	2	On tree trunks. (1 VSC)	NP
	Varanidae				
40	*Varanus salvator*	S(2)	S(1)	On forest floor	P
	SNAKES				
	Pythonidae				
41	*Python reticulatus*	-	S(1)	In forest stream	P
	Colubridae				
42	*Ahaetulla prasina*	2	-	On tree branches	NP
43	*A. mysterizans*	1	-	On tree branches along trail. Released.	NP
44	*Calamaria gimletti*	1	-	On forest floor under dead log. Released. (1 VSC).	NP
45	*Boiga dendrophila*	-	2	On tree branches near forest streams. Released.	NP
46	*Dendrelaphis caudolineatus*	-	2	On tree branch. Released.	NP
47	*D. formosus*	1	-	On tree branch. Released.	NP
48	*D. pictus*	1	-	On tree branch. Released.	NP
49	*Gonysoma oxycephalus*	-	1	On tree branches along forest stream. Released.	NP
50	*Xenochropus triaoguligera*	-	1	Along forest stream. Released.	NP
51	*Lycodon subcinctus*	1	-	Bark of tree. (1 VSC)	NP
	Viperidae				
52	*Parias hageni*	1	1	On branches of plants in forest. Released.	NP
53	*Tropidolaemus wagleri*	-	1	On bamboo tree. Released.	NP
	TURTLES				
	Trionychidae				
54.	*Dogania subplana*	2	1	Stream by camp in area A and adjacent Sg. Lallang FR. Released.	NP

	Bataguridae				
55	*Hosesemys spinosa*	-	1	On forest floor along trail	NP
	Total no. of species	41	37		
	Number of individuals	115	73		

Appendix 2. Volant and non-volant mammal species examined and sighted in Broga and Sungei Lallang Forest Reserve, Hulu Langat during May and September 2003. MN & N: Mist net and Harp-trap; T: rat trap; S: Sighted; FP: Footprints; Q: Quills; P: Protected; TP: Totally protected; NP: Not protected; V: Vocalisation.

No.	Family/Species	Methods	Broga FR	Sg. Lallang FR	Legal status	Remarks
	INSECTIVORA					
	Erinaceidae					
1	*Echinosorex gymnurus*	T/S	1	1	NP	Swamp & forest stream. Released.
	PHOLIDOTA					
	Manidae					
2	*Manis javanica*	S	-	1	TP	Forest trail
	DERMOPTERA					
	Cynocephalidae					
3	*Cynocephalus variegatus*	S	-	2	TP	Resting at tree branches.
	SCANDENTIA					
	Tupaiidae					
4.	*Tupaia glis*	T	2	1	NP	Forest floor. Released.
5	*T. minor*	T	-	1	NP	On fallen log. Released.
	CHIROPTERA					
	Pteropodidae					
6	*Cynopterus brachyotis*	MN	7	5	NP	Released
7	*C. horsefieldii*	MN	4	3	NP	"
8	*Penthetor lucasi*	MN	1	5	NP	"
9	*Balionycteris maculata*	MN	4	7	NP	"
10	*Chironax melanocephalus*	MN	1	5	NP	"
11	*Megaerops ecaudatus*	MN	3	4	NP	(2 VSC)
12	*Macroglossus sobrinus*	MN	1	4	NP	(1 VSC)
13	*Eonycteris spelaea*	MN	4	8	NP	Released
	Emballonuridae					
14	*Emballonura monticola*	HT	1	4	NP	(1 VSC)
	Nycteridae					
15	*Nycteris javanica*	MN	1	1	NP	(1 VSC)
	Megadermatidae					
16	*Megaderma spasma*	MN	1	2	NP	(1 VSC)
	Rhinolophidae					
17	*Rhinolophus affinis*	MN	1	2	NP	(1 VSC)
18	*R. stheno*	HT	-	5	NP	(1 VSC)
19	*R. macrotis*	HT	7	10	NP	(2 VSC)
20	*R. trifoliatus*	MN	2	-	NP	Released
21	*R. lepidus*	HT	3	4	NP	(1 VSC)

22	*R. luctus*	MN	1	1	NP	Released
	Hipposideridae					
23	*Hipposideros bicolor*	HT	2	4	NP	(2 VSC)
24	*H. galeritus*	HT	-	3	NP	(1 VSC)
25	*H. ridleyi*	HT	-	2	NP	(1 VSC)
26	*H. cervinus*	HT	1	1	NP	(1 VSC)
27	*H. armiger*	MN	-	1	NP	Released
28	*H. larvatus*	MN	4	6	NP	Released
29	*H. diadema*	MN	1	-	NP	Released
	Vespertilionidae					
30	*Myotis muricola*	HT	2	3	NP	(1 VSC)
31	*Tylonycteris robustula*	HT	1	-	NP	Released
32	*Pipistrellus tenuis*	HT	-	1	NP	(1 VSC)
33	*Glischropus tylopus*	HT	-	1	NP	Released
34	*Murina suilla*	HT	2	2	NP	(1 VSC)
35	*Kerivoula minuta*	HT	-	1	NP	(1 VSC)
36	*K. intermedia*	HT	-	1	NP	"
37	*K. papillosa*	HT	1	4	NP	Released
	Molossidae					
38	*Tadarida mops*	HT	-	1	NP	
	PRIMATES					
	Lorisidae					
39	*Nycticebus coucang*	S	-	2	TP	On branch of trees
	Cercopithecidae					
40	*Macaca fascicularis*	S	-	+	P	On branch of trees
41	*M. nemestrina*	S	-	7	P	On forest floor
42	*Semnopithecus obscurus*	S	-	2	TP	On canopy
43	*Prebystis femoralis*	S	-	2	TP	On canopy
	Hylobatidae					
44	*Hylobates lar*	V	-	+	TP	Morning & late evening
	RODENTIA					
	Sciuridae					
45	*Ratufa bicolour*	S	1	2	TP	Canopy
46	*Callosciurus notatus*	T	2	2	NP	On forest floor. Released.
47	*C. caniceps*	T	1	2	NP	Released
48	*C. nigrovittatus*	T	-	2	NP	Released
49	*Sundasciurus tenuis*	T	1	3	P	On forest floor
50	*S. lowii*	T	1	2	NP	On forest floor
51	*Rhinosciurus laticaudatus*	T	-	1	NP	On forest floor
52	*Lariscus insignis*	T	2	3	NP	On forest floor
	Pteromyidae					
53	*Petaurista petaurista*	S	-	2	TP	Resting on tall tree.
54	*Iomys horsefieldii*	T	-	1	TP	Resting on tree in the undergrowth
55	*Hylopetes spadicus*	T	-	1	TP	On tree branch in the undergrowth
	Hystricidae					
56	*Hystrix brachyura*	Q	+	+	TP	Collected on forest floor

	Muridae					
57	*Rattus tiomanicus*	T	5	-	NP	Forest floor
58	*Sundamys muelleri*	T	6	4	NP	"
59	*Leopoldamys sabanus*	T	2	6	NP	"
60	*Niviventer cremoriventer*	T	1	4	NP	"
61	*Maxomys surifer*	T	2	7	NP	"
62	*M. rajah*	T	1	1	NP	"
63	*M. whiteheadi*	T	1	1	NP	"
	CARNIVORA					
	Mustelidae					
64	Mustela nudipes	S	1	-	TP	Forest stream
65	*Aonyx cinerea*	S	1	-	TP	Forest stream
	Viveridae					
66	*Prionodon linsang*	S	-	1	TP	Forest floor
67	*Paradoxurus hermaphroditus*	S/T	2	2	P	Tree branches. Released.
68	*Actogalidia trivirgata*	T	-	1	TP	Tree branches. Released.
	Herpestidae					
69	*Herpestes brachyurus*	T	-	1	TP	Forest floor
	Felidae					
70	*Prionailurus bengalensis*	S	1	2	TP	Forest floor
71	*P. planiceps*	S	1	-	TP	Forest stream
	ARTIODACTLYA					
	Suidae					
72	*Sus scrofa*	FP	+	+	P	Forest floor
	Tragulidae					
73	*Tragulus javanica*	shot	2	-	P	by Orang asli
74	*T. napu*	Shot	-	1	P	by Orang asli
	No. of spp.	-	47	66	-	
	No. of individuals		93	169		

Appendix 3. List of birds recorded in the Broga and Sg Lallang Forest Reserve, Hulu Langat during May and September 2003. R: Resident; R &M: Resident and Migrant; M: Migrant; LR(nt) Near Threatened; VU: Vulnerable; P: Protected; TP: Totally Protected; NP: Not Protected.

No.	Species	Status	Study area		Conservation concern	
			Broga F.R.	Sg. Lallang FR	Malaysian	Globally
	PHASIANIDAE					
1	*Gallus gallus*	R	+	-	P	_
2	*Argusianus argus*	R	-	+	TP	LR(nt)
	PICIDAE					
3	*Sasia abnormis*	R	-	+	TP	_
4	*Celeus brachyurus*	R	+	+	TP	_
5	*Picus miniaceus*	R	+	+	TP	_
6	*Picus puniceus*	R	-	+	TP	_
7	*Blythipicus rubiginosus*	R	+	+	TP	_

8	*Meiglyptes tristis*	R	+	+	TP	–
9	*Meiglyptes tukki*	R	-	+	TP	LR(nt)
10	*Hemicircus concretus*	R	-	+	TP	–
	MEGALAIMIDAE					
11	*Megalaima chrysopogon*	R	+	+	TP	–
12	*Megalaima mystacophanos*	R	-	+	TP	LR(nt)
13	*Megalaima australis*	R	+	+	TP	–
14	*Calorhamphus fuliginosus*	R	+	+	TP	–
	BUCEROTIDAE					
15	*Buceros rhinoceros*	R	+	+	TP	LR(nt)
16	*Buceros vigil*	R	-	+	TP	LR(nt)
17	*Anorrhinus galeritus*	R	-	+	TP	–
18	*Aceros comatus*	R	-	+	TP	LR(nt)
19	*Aceros undulates*	R	-	+	TP	–
	TROGONIDAE					
20	*Harpactes diardlii*	R	-	+	TP	LR(nt)
21	*Harpactes duvaucelii*	R	-	+	TP	LR(nt)
	ALCEDINIDAE					
22	*Alcedo euryzona*	R	-	+	TP	VU
23	*Ceyx rufidorsa*	R	-	+	TP	–
	HALCYONIDAE					
24	*Lacedo pulchella*	R	+	+	TP	–
25	*Actenoides concretus*	R	-	+	TP	LR(nt)
	MEROPIDAE					
26	*Nyctyornis amictus*	R	-	+	TP	–
27	*Merops viridis*	R&M	+	-	TP	–
	CUCULIDAE					
28	*Cuculus micropterus*	R&M	+	+	TP	–
29	*Cacomantis sonneratii*	R	+	+	TP	–
30	*Cacomantis merulinus*	R	+	+	TP	–
31	*Cacomantis sepulcralis*	R	+	+	TP	–
32	*Chrysococcyx xanthorhynchus*	R&M	-	+	TP	–
33	*Surniculus lugubris*	R&M	+	+	TP	–
34	*Cuculus fugax*					
35	*Phaenicophaeus diardi*	R	-	+	TP	LR(nt)
36	*Phaenicophaeus chlorophaeus*	R	-	+	TP	–
37	*Phaenicophaeus javanicus*	R	-	+	TP	–
38	*Phaenicophaeus curvirostris*	R	-	+	TP	–
	CENTROPODIDAE					
39	*Centropus sinensis*	R	+	–	TP	–
	PSITTACIDAE					
40	*Loriculus galgulus*	R	+	+	P	–

	APODIDAE					
41	*Rhaphidura leucospygialis*	R	+	+	TP	_
42	*Cypsiurus balasiensis*	R	+	+	TP	_
43	*Apus affinis*	R	+	+	TP	_
	HEMIPROCNIDAE					
44	*Hemiprocne longipennis*	R	+	+	TP	_
45	*Hemiprocne comata*	R	+	+	TP	_
	STRIGIDAE					
46	*Otus bakkamoena*	R	+	+	TP	_
47	*Bubo sumatrana*	R	-	+	TP	-
	BATRACHOSTOMIDAE					
48	*Batrachostomus javensis*	R	-	+	TP	_
	CAPRIMULGIDAE					
49	*Caprimulgus macrurus*	R	+	-	TP	_
	COLUMBIDAE					
50	*Chalcophaps indica*	R	+	+	P	_
51	*Treron vernans*	R	+	-	P	_
52	*Treron curvirostra*	R	+	+	P	_
	ACCIPITRIDAE					
53	*Spilornis cheela*	R	+	+	TP	_
54	*Spizaetus cirrhatus*	R	-	+	TP	_
55	*Spizaetus alboniger*	R	-	+	TP	_
	FALCONIDAE					
56	*Microhierax fringillarius*	R	+		TP	_
	EURYLAIMIDAE					
57	*Calyptomena viridis*	R	-	+	TP	LR(nt)
58	*Eurylaimus javanicus*	R	-	+	TP	_
59	*Eurylaimus ochromalus*	R	+	+	TP	LR(nt)
60	*Corydon sumatranus*	R	-	+	TP	_
	IRENIDAE					
61	*Irena puella*	R	+	+	TP	_
62	*Chloropsis sonnerati*	R	+	+	TP	_
63	*Chloropsis cyanopogon*	R	-	+	TP	LR(nt)
64	*Chloropsis cochinchinensis*	R	+	+	TP	_
	LANIIDAE					
65	*Lanius tigrinus*	M	+	-	TP	_
	CORVIDAE					
66	*Coracina fimbriata*	R	-	+	TP	_
67	*Pericrocotus flammeus*	R	+	+	TP	_
68	*Pericrocotus igneus*	R	+	+	TP	LR(nt)
69	*Hemipus picatus*	R	-	+	TP	_

70	*Hemipus hirundinaceus*	R	+	+	TP	_
	CORVIDAE					
71	*Dicrurus paradiseus*	R	+	+	TP	_
72	*Terpsiphone paradisi*	R&M	-	+	TP	_
73	*Aegithina viridissima*	R	+	+	TP	LR(nt)
74	*Aegithina lafresnayei*	R	+	+	TP	_
75	*Philentoma pyrhopterum*	R	-	+	TP	_
76	*Tephrodornis gularis*	R	+	+	TP	_
	MUSCICAPIDAE					
77	*Eumyias thalassina*	R	+	+	TP	_
78	*Copsychus saularis*	R	+	-	NP	_
79	*Copsychus malabaricus*	R	+	+	P	
80	*Enicurus ruficapillus*	R	-	+	TP	LR(nt)
	STURNIDAE					
81	*Gracula religiosa*	R	+	+	P	_
	SITTIDAE					
82	*Sitta frontalis*	R	-	+	TP	_
	PARIDAE					
83	*Melanochlora sultanea*	R	-	+	TP	_
	HIRUNDINIDAE					
84	*Hirundo rustica*	M	+	+	TP	_
85	*Hirundo tahitica*	R	+	+	TP	_
	PYCNONOTIDAE					
86	*Pycnonotus atriceps*	R	+	+	TP	_
87	*Pycnonotus melanicterus*	R	+	+	TP	_
88	*Pycnonotus squamatus*	R	+	+	TP	LR(nt)
89	*Pycnonotus cyaniventris*	R	-	+	TP	LR(nt)
90	*Pycnonotus finlaysoni*	R	+	-	TP	_
91	*Pycnonotus plumosus*	R	+	-	TP	_
92	*Pycnonotus simplex*	R	-	+	TP	_
93	*Pycnonotus brunneus*	R	+	+	TP	_
94	*Pycnonotus erythropthalmos*	R	+	+	TP	_
95	*Alophoixus bres*	R	-	+	TP	_
96	*Alophoixus phaeocephalus*	R	-	+	TP	_
97	*Tricholestes criniger*	R	+	+	TP	_
98	*Iole olivacea*	R	+	+	TP	LR(nt)
99	*Ixos malacensis*	R	-	+	TP	LR(nt)
100	*Hemixos* flavala	R	+	+	TP	_
	CISTICOLIDAE					
101	*Prinia rufescens*	R	+	-	TP	_
102	*Prinia flaviventris*	R	+	-	TP	_
	ZOSTEROPIDAE					
103	*Zosterops evertti*	R	+	-	TP	_
	SYLVIIDAE					
104	*Orthotomus sutorius*	R	+	+	TP	_
105	*Orthotomus atrogularis*	R	+	+	TP	_

106	*Orthotomus sericeus*	R	-	+	TP	–
107	*Phylloscopus borealis*	M	-	+	TP	–
108	*Phylloscopus coronatus*	M	-	+	TP	–
109	*Abroscopus superciliaris*	R	-	+	TP	–
110	*Malacocincla malaccensis*	R	-	+	TP	LR(nt)
111	*Malacocincla sepiarium*	R	-	+	TP	–
112	*Pellorneum capistratum*	R	-	+	TP	–
113	*Malacopteron magnirostre*	R	-	+	TP	–
114	*Stachyris poliocephala*	R	-	+	TP	–
115	*Stachyris maculata*	R	-	+	TP	LR(nt)
116	*Stachyris erythroptera*	R	-	+	TP	–
117	*Macronous gularis*	R	+	+	TP	–
118	*Macronous ptilosus*	R	+	+	TP	LR(nt)
119	*Yuhina zantholeuca*	R	-	+	TP	–
	NECTARINIDAE					
120	*Prionochilus maculatus*	R	-	+	TP	–
121	*Prionochilus percussus*	R	-	+	TP	–
122	*Dicaeum chrysorrheum*	R	-	+	TP	–
123	*Dicaeum trigonostigma*	R	+	+	TP	–
124	*Dicaeum concolor*	R	-	+	TP	–
125	*Anthreptes simplex*	R	+	+	TP	–
126	*Anthreptes rhodolaema*	R	-	+	TP	LR(nt)
127	*Anthreptes singalensis*	R	-	+	TP	–
128	*Hypogramma hypogrammicum*	R	-	+	TP	–
129	*Anthreptes temminckii*	R	-	+	TP	-
130	*Arachnothera longistra*	R	+	+	TP	–
131	*Arachnothera flavigaster*	R	-	+	TP	–
132	*Arachnothera chrysogenys*	R	-	+	TP	–
133	*Arachnothera affinis*	R	+	+	TP	–
134	*Arachnothera robusta*	R	+	+	TP	-
	ESTRILDINAE					
135	*Lonchura striata*	R	+	-	NP	–
	Total species at site		78	121		

Journal of Science and Technology in the Tropics (2009) **5**: 101-103

Gasteracantha crucigera (Araneae: Araneidae) from Maliau Basin, Sabah, Malaysia: an overlooked spiny-backed orb-weaver spider from Peninsular Malaysia

Yong Hoi Sen[1] **and Hirotsugu Ono**[2]
[1]Institute of Biological Sciences, University of Malaya, 50603 Kuala Lumpur, Malaysia
(Email: yong@um.edu.my)
[2]Department of Zoology, National Museum of Nature and Science, 3-23-1 Hyakunin-cho, Shinjuku-ku, Tokyo 169-0073, Japan
(Email: ono@kahaku.go.jp)

Received 30-08-2009; accepted 11-11-2009

Abstract Two female specimens of *Gasteracantha crucigera* Bradley, 1837 were collected around the Eucalyptus Camp in Maliau Basin, Sabah, Malaysia in 2006. This spiny-backed orb-weaver is a new record for Sabah and Borneo. Its occurrence in Peninsular Malaysia (then Malaya) was documented in 1944. Three other species of *Gasteracantha* – *G. diardi* (Lucas, 1835), *G. doriae* Simon, 1877 and *G. sturi* (Doleschall, 1857) – were also found in the Maliau Basin. *Gasteracantha sturi* is a new record for Malaysia and Borneo.

Keywords Malaysia, Borneo, Araneae, Araneidae, *Gasteracantha*, new records

INTRODUCTION

Spiders of the genus *Gasteracantha* Sundevall, 1833 are commonly known as spiny-backed orb-weavers and spiny orb-weavers because of the prominent spines on their abdomen. They are beautiful spiders with a hard flat abdomen ornamented with lateral spines and dorsal sigillae. Their spinnerets are elevated and enclosed by a thick flange.

Current taxonomic classification lists some 69 species of *Gasteracantha* in the world [1]. We report here the finding of *Gasteracantha crucigera* Bradley, 1837 in Maliau Basin, Sabah, Malaysia and an overlooked publication [2] regarding the occurrence of this species in Peninsular Malaysia. Other *Gasteracantha* species encountered in the Maliau Basin are highlighted.

MATERIALS AND METHODS

A scientific expedition to the Maliau Basin, Sabah, Malaysia was organized by the Academy of Sciences Malaysia and Sabah Foundation on 18-23 April 2006. The study site was around the Eucalyptus Camp, situated at N 04° 52' 18", E 116° 49' 35" and north-west of the Maliau Basin Conservation Area (MBCA) [3]. This area is about 950 m to 1000 m above sea level. The vegetation comprises lower montane forest and heath forest.

Spiders when encountered were photographed and where necessary were collected and preserved in ethanol. They were later identified using existing literature [e.g. 4, 5] and confirmed by H. Ono.

RESULTS AND DISCUSSION

Two female specimens of *G. crucigera* were encountered in the Maliau Basin – one specimen in the lower montane forest near the stream close to the camp site, and another specimen in the heath forest near the helipad (locations as indicated in [3]).

Gasteracantha crucigera had been referred to in earlier literature as *Gasteracantha crepidiphora* O. Pickard-Cambridge, 1879 and *Gasteracantha similis* Kulczyński, 1911 [1]. In practically all the current literature, it is stated to occur only in New Guinea [1]. An old publication [2] reporting the occurrence of this spiny-backed orb-weaver in Peninsular Malaysia, Java and New Guinea appears to have gone unnoticed.

JOURNAL OF SCIENCE AND TECHNOLOGY IN THE TROPICS

INSTRUCTIONS TO CONTRIBUTORS

JOSTT is a multi-disciplinary journal. It publishes original research articles and reviews on all aspects of science and technology relating to the tropics. All manuscripts are reviewed by at least two referees, and the editorial decision is based on their evaluations.

Manuscripts are considered on the understanding that their contents have not been previously published, and they are not being considered for publication elsewhere. The authors are presumed to have obtained approval from the responsible authorities, and agreement from all parties involved, for the work to be published.

Submission of a manuscript to JOSTT carries with it the assignment of rights to publish the work. Upon publication, the Publishers (COSTAM and ASM) retain the copyright of the paper.

Manuscript preparation

Manuscripts must be in English, normally not exceeding 3500 words. Type double spaced, using MS Word, on one side only of A4 size with at least 2.5 cm margins all round. Number the pages consecutively and arrange the items in the following order: title page, abstract, key words, text, acknowledgements, references, tables, figure legends.

Title page

Include (i) title, (ii) names, affiliations and addresses of all authors, (iii) running title not exceeding five words, and (iv) email of corresponding author.

Abstract and key words

The abstract, not more than 250 words, should be concise and informative of the contents and conclusions of the work. A list of not more than five key words must immediately follow the abstract.

Text

Original research articles should be organized as follows: Introduction, Materials and Methods, Results, Discussion, Acknowledgement, References. The International System of Units (SI) should be used. Scientific names and mathematical parameters should be in italics.

References

References should be cited in the text as numbers enclosed with square [ ] brackets. The use of names in the text is discouraged. In the reference section, the following examples should be followed:

1. Yong H.S., Dhaliwal S.S. and Teh K.L. (1989) A female Norway rat, *Rattus norvegicus*, with XO sex chromosome constitution. *Naturwissenschaften* **76**: 387-388.
2. Beveridge W.I.B. (1961) *The Art of Scientific Investigation*. Mercury Book, London.
3. Berryman A.A. (1987) The theory and classification of outbreaks. In Barbosa P. and Schultz J.C. (eds.) *Insect outbreaks* pp. 3-30. Academic Press, San Diego.

Tables

Tables should be typed on separate sheets with short, informative captions, double spacing, numbered consecutively with Arabic numerals, and do not contain any vertical lines. A table should be set up to fit into the text area of at most the entire page of the Journal.

Illustrations

Black-and-white figures (line drawings, graphs and photographs) must be suitable for high-quality reproduction. They must be no bigger than the printed page, kept to a minimum, and numbered consecutively with Arabic numerals. Legends to figures must be typed on a separate sheet. Colour illustrations can only be included at the author's expense.

Proofs and reprints

Authors will receive proofs of their papers before publication. Order for reprints must be made when returning the proofs.

Submission

Manuscripts should be submitted in triplicate (including all figures but not original artwork), together with a CD version of the text, to:

The Editorial Office
Journal of Science and Technology
in the Tropics
Room 1&2, 2nd Floor
Bangunan Sultan Salahuddin Abdul Aziz Shah
16 Jalan Utara, 46200 Petaling Jaya
Selangor Darul Ehsan
Malaysia

JOSTT is listed in Scopus

The 1944 paper by Kayashima [2] documented five specimens of *G. crucigera* from Peninsular Malaysia (Malaya then) – two specimens from Mount Ophir (now Gunung Ledang), Johor (collected by H. C. Abraham on 20 September 1920), one specimen from Gunung Tahan, Pahang (collected by W. A. O. Edward on 20 December 1921), one specimen from Gunung Kenering, Perak (collected by H. C. Abraham on 4 June 1924), and one specimen from Wray's Hill, Perak (collected by H. C. Abraham on 8 May 1932). However the specimens could not be located now. The carapace (cephalothorax) of these specimens measured 3.8-4.5 mm long and 3.1-4.0 mm wide, while the abdomen measured 5-7 mm long and 7-9.6 mm wide.

According to Izumi Kayashima's decription (in Japanese), pp. 9-10, *G. crucigera* (Fig. 1) possesses the following characteristics –

Carapace: Head is strongly raised and thorax is low and almost covered by the anterior edge of abdomen. Eyes eight in number and respectively on eye-tubercles, both anterior and posterior median eyes are situated in the centre of anterior edge of the head, while the lateral eyes are in the sides of the head. Chelicera very strong basally, furnished with six teeth on promargin of fang furrow, in order of their size, 5, 4, 3, 2, 1, 6, and five teeth on the retromargin, 5, 4, 3, 2, 1. Maxillae long rectangular, both the inner margins separated from each other wider apically. Labium is almost triangular. Sternum cuneiform, both the lateral margins round, a pair of pointed tubercles present in the anterior corners and two pairs of tubercles present in the middle of both lateral margins, the posterior end of sternum pointed and extending between coxae of legs IV. Legs short in comparison with the body size.

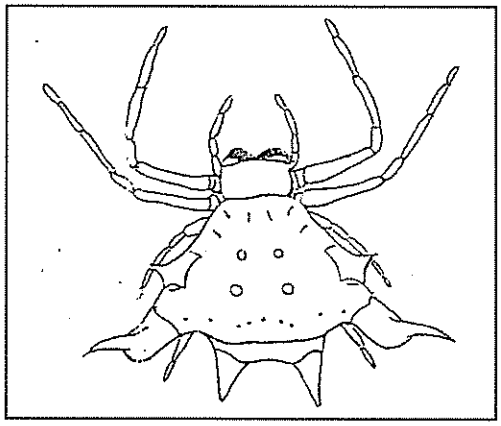

Figure 1. *Gasteracantha crucigera*, drawing by I. Kayashima (1944).

Abdomen: Trapezoid in dorsal view, the anterior margin half the width of the posterior margin, eight pairs of sigillae arranged as follows: the first pair on the anterior edge, the second pair in the corners, the third to the fifth pairs on lateral margins, the sixth to eighth pairs on the posterior margin. The anterior lateral apophysis of abdomen is small, the posterior lateral apophysis basally thick, with a curved spine distally, and the posterior median apophysis much larger and longer than the anterior lateral one. Abdomen inverted isosceles triangle in posterior view, with four horizontal ridges parallel to the posterior margin, and the posterior median apophyses appear between the first and the second ridges. Spinnerets cylindrical, extending vertically and situated at the apex of triangle.

Coloration: Carapace blackish brown, lighter along the anterior margin, chelicerae, maxillae and labium reddish brown, sternum reddish brown with yellowish brown tubercles looking like six spots along the margin. Palps and legs reddish brown, respectively darker distally. Abdomen light yellow dorsally, with reddish black sigillae and shiny black apophyses, venter dirty yellow with shiny black spinnerets.

The present finding of *G. crucigera* (Figs. 2, 3) in the Malaiau Basin, Sabah is the first record of this species in Borneo. In addition to *G. crucigera*, three other *Gasteracantha* species – *G. diardi* (Lucas, 1835), *G. doriae* Simon, 1877 and *G. sturi* (Doleschall, 1857) – were also found in the Maliau Basin. *Gasteracantha diardi* and *G. doriae* occur in Peninsular Malaysia as well as Borneo [2]. The other species, *G. sturi* has been recorded to occur only in Sumatra, Java and Moluccas [1]. It is therefore a new record for Malaysia and Borneo.

In addition to *G. crucigera*, eight other species were reported by Kayashima [2] – *G. arcuata* (Fabricius, 1793), now placed under the genus *Macracantha* Simon, 1864; *G. cuspidata* C. L. Koch, 1837; *G. diardi* (Lucas, 1835); *G. doriae* Simon, 1877; *G. hasselti* C. L. Koch, 1837; *G. kuhli* C. L. Koch, 1837; *G. mammosa* C. L. Koch, 1844, now placed under *Thelacantha brevispina* (Doleschall, 1857); and *G. mengei* Keyserling, 1864.

In recent years many new species and new records have been added to the spider fauna of Malaysia [e.g.

Figure 2. *Gasteracantha crucigera* from Maliau Basin, Sabah, Malaysia.

Figure 3. Ventral view of *Gasteracantha crucigera* from Maliau Basin, Sabah, Malaysia.

6-10]. Our materials at hand indicate that many more are yet to be documented.

Acknowledgements – Many thanks to the Academy of Sciences Malaysia and Sabah Foundation for supporting the expedition, and our respective institutions University of Malaya and the National Museum of Nature and Science for providing various facilities.

REFERENCES

1. Platnick N.I. (2009) *The world spider catalog, version 10.0*. American Museum of Natural History, online at http://research.amnh.org/entomology/spiders/catalog/index.html.
2. Kayashima I. (1944) A study of the spiders of the genus *Gasteracantha* from Malaya. *Archives of the Kuala Lumpur Museum, Selangor* **13**: 1-30 (2 plates). [in Japanese]
3. Ng Y.F., Yong H.S., Dow R.A. and Hämäläinen M. (2008) Dragonflies (Insecta: Odonata) from the Maliau Basin, Sabah, Malaysia. *Journal of Science and Technology in the Tropics* **4**: 13-18.
4. Koh J.K.H. (1989) *A guide to common Singapore spiders*. Singapore Science Centre, Singapore.
5. Murphy F. and Murphy J. (2000) *An introduction to the spiders of South East Asia*. Malaysian Nature Society, Kuala Lumpur.
6. Ono H. and Hashim R. (2008) Four new species of the Family Zodariidae (Araneae) from Malaysia. *Memoirs of the National Museum of Nature and Science, Tokyo* (45): 41-51.
7. Yong H.S. (2008) *Telamonia dimidiata* and *Phintella versicolor* (Arachnida: Salticidae): two new records for Peninsular Malaysia. *Journal of Science and Technology in the Tropics* **4**: 97-98.
8. Yong H.S. (2009) *Neoscona vigilans* (Arachnida: Araneae: Araneidae): a new record of orb-web spider from Peninsular Malaysia. *Journal of Science and Technology in the Tropics* **5**: 11-12.
9. Yong H.S. (2009) *Nephila antipodiana* (Araneae: Nephilidae) from Pahang: a new record for Peninsular Malaysia. *Journal of Science and Technology in the Tropics* **5**: 19-21.
10. Deeleman-Reinhold C.L. (2009) Description of the lynx spiders of a canopy fogging project in northern Borneo (Araneae: Oxyopidae), with description of a new genus and six new species of *Hamataliwa*. *Zoologische Medelingen Leiden* **83**: 673-700.

Journal of Science and Technology in the Tropics (2009) **5**: 105-110

Diversity of butterfly (Lepidoptera: Rhopalocera) communities at three habitats in Hulu Langat, Selangor, Peninsular Malaysia

Y. F. Ng* and O. Siti Mariam
Center of Insect Systemtics, School of Environment and Natural Resource Sciences
Faculty of Science and Technology, Universiti Kebangsaan Malaysia
43000 Bangi, Selangor D.E., Malaysia
(*E-mail: ng_yf@ukm.my)

Received 28-10-2009; accepted 12-11-2009

ABSTRACT Hulu Langat is located in Selangor, Peninsular Malaysia. The depletion of flora and fauna diversity has always been associated with the developments of infrastructure and urbanization. The present study was conducted to study the diversity of butterfly (Lepidoptera) of different habitats in Hulu Langat. The sampling of the butterfly was carried out from December 2008 until April 2009 at three habitats comprising of forested area (Gunung Nuang), recreational area (Sungai Congkak) and residential area (an indigenous village). A total of 598 individuals of butterflies belonging to 5 families and 102 species were recorded. The families recorded in this sampling are Hesperiidae, Lycaenidae, Nymphalidae, Papilionidae and Pieridae. The family Nymphalidae represented by 47 species (46.1%) was the most species rich family. In term of location, the forested area had the highest number of species (69 species), followed by recreational area (42 species) and residential area (33 species). The Shannon-Weiner index of species diversity of forested area was 3.74, followed by recreational area (H'=3.40) and residential area (H'=2.38). The species Evenness (E') of the forested and recreational areas was relatively higher compared to residential site. The species diversity and evenness of the sampling areas were discussed in this paper.

Keywords butterfly – diversity – similarity – habitat

INTRODUCTION

Butterfly is regarded as the most beautiful insect belonging to the order Lepidoptera, which also includes the moths. They are remarkably different from the other insects by their impressive coloration pattern and the body is fully covered by scales. There are about 15,000 species of butterflies (Rhopalocera) worldwide [1, 2]. Of this, about 1031 species are represented in Peninsular Malaysia [3]. Butterfly can be categorized into 5 families; Papilionidae, Pieridae, Nymphalidae, Lycaenidae, and Hesperiidae [3].

Butterflies can be beneficial or harmful insects. The beneficial butterflies comprise pollinators, predators and bioindicators of habitat quality [1, 4]. Many of the butterflies have high aesthetic value such as the Malay Lacewing (*Cethosia hypsea*). Due to this, butterflies have been collected as souvenirs for tourists and trade via internet by international collectors. The wildlife protection act is not comprehensive in protecting butterflies from overexploitation. For instance, only one species *Trogonoptera brookiana* is listed as protected species.

The butterflies coexist with the flora of an in-situ habitat. Changes in environment can affect the presence of butterflies. They are sensitive towards any changes in the environment [2, 5]. Ecosystem degradation can cause depletion in butterfly population [2]. The degradation of an ecosystem is usually due to logging activity, overgrazing and conversion of forest area into agriculture. Studies were done on butterflies to monitor the environment quality [6, 7]. In this paper, we attempt to study the diversity of butterflies in different habitats in Hulu Langat, Selangor.

MATERIALS AND METHODS

Collecting

Sampling of the butterfly in Hulu Langat was conducted from December 2008 until April 2009.

Sampling was done for two days duration of 4 replicate samplings at respective sampling site, and by two collectors. Collecting of butterfly was conducted by using a 30 cm diameter sweep net. Samplings were done in the morning from 9.00 a.m. to 1.00 p.m. and in the afternoon from 2.00 p.m. to 4.00 p.m. per day. All collected specimens were identified to species using available literature [1, 3, 8], and were deposited at the Center of Insects Systematics, Universiti Kebangsaan Malaysia.

Sampling sites

Forested area

This site is an undisturbed area consisting of dipterocarp forest of the Gunung Nuang Forest Reserve. Its summit marks the meeting point of three Malaysian states, Negeri Sembilan, Pahang and Selangor. There are three hiking routes to the peak – Kuala Pangson in Hulu Langat, Kampung Kemensah in Gombak and Bukit Tinggi in Bentong. The sampling site is located at 03° 12.593' N, 101° 50.607'E (Fig. 1).

Recreational area

This site is located adjacent and along the Congkak River and is a disturbed area with recreational activity and artificial landscapes. This recreation area consists of small patches of lowland dipterocarp forest. It is located at 03° 12.930' N, 101° 53.022'E and about 13 km away from Gunung Nuang (Fig. 1).

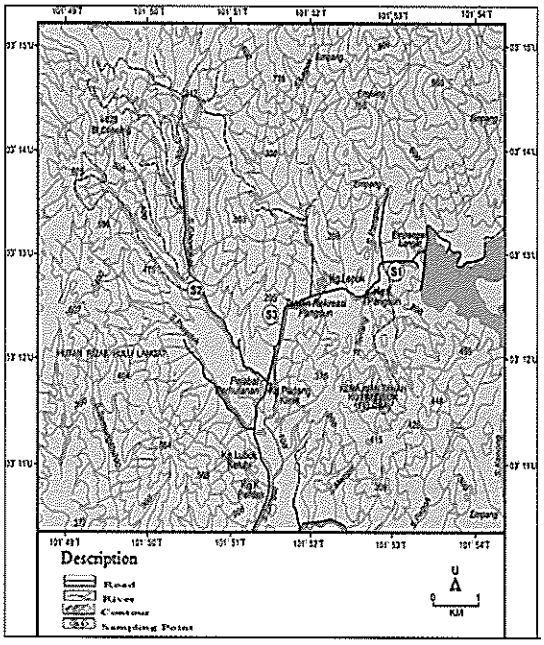

Figure 1. Location of study site: Forested area/ Gunung Nuang (S1), Recreational area/Sungai Congkak (S2), residential area/village (S3).

Residential area

The third site is located near the indigenous village, Hulu Langat, Selangor (Fig. 1), situated at 03° 12.45'N and 101° 51.56'E. There were some orchards of mango and rambutan, and small vegetable farms run by the villagers.

Data analysis

The total number of individuals for each species was recorded. Analyses of Shannon-Weiner diversity index (H') and species evenness index (E') were computed by using GW Basic Statistical Program [9].

RESULTS

A total of 598 individuals of 102 species of butterflies belonging to five families were recorded – Hesperiidae, Lycaenidae, Nymphalidae, Papilionidae and Pieridae. Table 1 shows the number of individuals and species, and their percentage in each family. Based on the number of individuals, the dominant families were constituted of Nymphalidae (48.7%) followed by Pieridae (30.3%), Lycaenidae (13.1%) and Hesperiidae (4.1%), and the least was Papilionidae (3.8%). On the species diversity, Nymphalidae was the most species rich family, represented by 46.1%, followed by Pieridae (17.6%), Lycaenidae (13.7%) and the least was Papilionidae which was represented by 9.8% of the total of 102 species (Table 1).

The residential area yielded the most number of butterfly with 307 individuals and the second was the forested area by 196 individuals (Table 2). *Yptima ceylonica*, the common three ring butterfly was the most dominant in number of individuals with 89 individuals of the total. Forty five species were represented by only one specimen each; this included the banded swallowtail butterfly *Papilio demolion* and the great egg-fly butterfly *Hypolimnas bolina*.

The number of species also differed among the sampling habitats with the most number of species collected from the forested area with a total of 69 species followed by recreational area (42 species) and residential area (33 species). The Shannon-Weiner index of species diversity of forested area was 3.74, followed by recreational area (H'=3.40) and

Table 1. Number of individuals, species and percentage of each butterfly family in Hulu Langat, Selangor.

Family	Number of Individuals	Percentage (%)	Number of species	Percentage (%)
Hesperiidae	25	4.1	13	12.8
Lycaenidae	78	13.1	14	13.7
Nymphalidae	291	48.7	47	46.1
Papilionidae	23	3.8	10	9.8
Pieridae	181	30.3	18	17.6
Total	598	100.00	102	100.00

Table 2. Number of individuals of each species in forested, recreational and residential areas of Hulu Langat.

	Taxon	Habitat			Total (n)
		Forested area	Recreational area	Residential area	
	Family: Hesperiidae				
1.	*Ampittia dioscorides camertes*	0	0	2	2
2.	*Ancistroides nigrita maura*	2	0	0	2
3.	*Astictopterus jama jama*	3	0	0	3
4.	*Iambrix salsala salsala*	2	0	0	2
5.	*Matapa aria*	0	1	0	1
6.	*Notocrypta paralysos varians*	1	0	0	1
7.	*Parnara bada*	2	0	0	2
8.	*Potanthus juno*	1	0	0	1
9.	*Potanthus omaha omaha*	1	0	2	3
10.	*Potanthus trachala tytleri*	1	0	0	1
11.	*Psolos fuligo fuligo*	2	0	0	2
12.	*Taractrocera archias quinta*	2	0	1	3
13.	*Taractrocera ardonia*	1	0	1	2
	Family: Lycaenidae				
14.	*Anthene emolus goberus*	1	0	0	1
15.	*Arhopala epimuta epiala*	0	1	0	1
16.	*Castalius roxus pothus*	18	0	0	18
17.	*Catochrysops panormus exiguus*	1	1	0	2
18.	*Cheritra freja frigga*	1	1	0	2
19.	*Curetis tagalica labuana*	1	0	0	1
20.	*Jamides elpis pseudelpis*	1	0	0	1
21.	*Jamides celeno aelianus*	11	2	0	13
22.	*Lampides boeticus*	1	0	0	1
23.	*Loxura atymnus fuconius*	0	0	2	2
24.	*Poritia sumatrae sumatrae*	0	1	0	1
25.	*Spindasis lohita senama*	1	0	1	2
26.	*Zeltus amasa maximinianus*	1	0	0	1
27.	*Zizula hylax pygmaea*	11	0	21	32
	Family: Papilionidae				
28.	*Atrophaneura coon doubledayi*	1	0	0	1
29.	*Atrophaneura varuna varuna*	2	0	0	2
30.	*Graphium agetes*	1	0	0	1
31.	*Graphium bathycles bathycloides*	0	1	0	1
32.	*Graphium delessertii delessertii*	3	0	0	3
33.	*Graphium sarpedon luctatius*	1	1	0	2
34.	*Pachliopta aristolochiae asteris*	1	0	0	1
35.	*Papilio demolion demolion*	0	0	1	1
36.	*Papilio polytes romulus*	1	0	1	2
37.	*Trogonoptera brookiana albescens*	2	7	0	9
	Family: Pieridae				
38.	*Appias indra plana*	2	2	0	4

39.	*Appias libythea olferna*	0	0	69	69
40.	*Appias lyncida vasava*	8	10	2	20
41.	*Appias nero figulina*	1	0	0	1
42.	*Catopsilia pyranthe pyranthe*	0	0	2	2
43.	*Cepora iudith malaya*	3	0	0	3
44.	*Eurema ada iona*	0	1	1	2
45.	*Eurema andersonii andersonii*	1	0	0	1
46.	*Eurema blanda snelleni*	2	0	2	4
47.	*Eurema hecabe contubernalis*	2	3	14	19
48.	*Eurema lacteola lacteola*	5	2	8	15
49.	*Eurema sari sodalis*	1	1	1	3
50.	*Eurema simulatrix tecmessa*	3	3	0	6
51.	*Gandaca harina distanti*	5	1	1	7
52.	*Hebomoia glaucippe aturia*	0	1	0	1
53.	*Leptosia nina nina*	5	2	15	22
54.	*Pathysa (Paranticopsis) delessertii delessertii*	0	1	0	1
55.	*Pareronia valeria lutescens*	1	0	0	1
	Family: Nymphalidae				
56.	*Ariadne ariadne ariadne*	0	0	1	1
57.	*Athyma nefte subrata*	1	0	0	1
58.	*Charaxes bernadus crepax*	1	0	0	1
59.	*Chersonesia rahria rahria*	0	1	0	1
60.	*Cirrochroa emalea emalea*	1	0	0	1
61.	*Cirrochroa orissa orissa*	0	1	0	1
62.	*Cupha erymanthis lotis*	1	1	0	2
63.	*Cyrestis nivea nivalis*	1	0	0	1
64.	*Danaus hamata*	7	0	0	7
65.	*Doleschallia bisaltide pratipa*	1	3	1	5
66.	*Elimnias penanga penanga*	0	1	0	1
67.	*Elymnias panthera panthera*	1	0	0	1
68.	*Euploea radamanthus*	2	0	0	2
69.	*Euploea mulciber*	1	0	0	1
70.	*Euthalia kanda marana*	0	1	0	1
71.	*Euthalia monina monina*	1	1	0	2
72.	*Faunis canens arcesilas*	0	3	0	3
73.	*Hypolimnas anomala*	1	0	0	1
74.	*Hypolimnas bolina*	0	0	1	1
75.	*Ideopsis gaura perakana*	1	0	0	1
76.	*Lasippa tiga siaka*	0	1	0	1
77.	*Lexias pardalis dirteana*	0	10	0	10
78.	*Mycalesis horsfieldi hermana*	0	1	0	1
79.	*Mycalesis janardana sagittigera*	3	4	0	7
80.	*Mycalesis maianeas maianeas*	0	1	0	1
81.	*Mycalesis mineus macromalayana*	10	5	6	21
82.	*Mycalesis mineus mineus*	0	0	1	1
83.	*Mycalesis perseus cepheus*	0	0	1	1
84.	*Neptis hylas*	2	0	0	2
85.	*Orsotriaena medus cinerea*	1	0	10	11
86.	*Phaedyma columella singa*	3	0	2	5
87.	*Phalanta alcippe alcesta*	0	1	0	1
88.	*Precis almana javana*	3	0	3	6
89.	*Precis iphita horsfieldi*	2	0	0	2
90.	*Precis orithya wallacei*	0	0	13	13
91.	*Ragadia makuta siponta*	0	3	0	3
92.	*Xanthotaenia busiris busiris*	0	2	0	2
93.	*Tanaecia flora flora*	0	1	0	1
94.	*Terinos terpander robertsia*	0	3	0	3

95.	*Thaumantis odana pishuna*	0	2	0	2
96.	*Tirumala septentrionis septentrionis*	1	0	0	1
97.	*Yptima baldus newboldi*	12	5	38	55
98.	*Yptima ceylonica*	8	0	81	89
99.	*Yptima fasciata torone*	0	1	0	1
100.	*Yptima pandocus corticaria*	1	0	1	2
101.	*Yptima philomela philomela*	1	0	0	1
102.	*Yptima savara tonkiniana*	12	0	1	13
	Total individual	196	95	307	598
	Total number of species	69	42	33	
	Cumulative number of species				102
	Shannon-Weiner Index (H')	3.74	3.40	2.38	
	Evenness Index (E')	0.89	0.91	0.68	

residential area (H'=2.38). The species evenness (E') of the forested and recreational areas was relatively higher compared to the residential site.

DISCUSSION

The total number of species collected in this study constituted about 9.89% (102 species) of the total 1031 species of butterflies in Peninsular Malaysia [3]. Within such a short sampling duration and with only four replications, the number of butterflies recorded from Hulu Langat is considered satisfactory. A long term sampling covering a great variety of habitats and ecosystems would certainly yield more butterfly species. The Nymphalidae were the most abundant family with a total of 291 individuals that constituted 48.7% of the total. This was in accordance with the ability of the butterflies to survive in both shade and open areas [8], which tantamount to the habitats characteristics of all sampling sites (forest, garden and open area). In term of location, the residential area which was characterized by open area had the largest number of individuals (307 individuals). This was largely contributed by two commonest butterflies, *Yptima ceylonica* (81 individuals) and *Appias libythea olferna* (69 individuals). This can be explained by common species having more individuals than rare species and had the ability to survive in all kinds of environment [10].

The results also revealed that forested area (69 species) yielded more butterfly species than recreational area (42 species) and residential area (33 species). This result was to be expected as the forested area was highly heterogeneous in terms of vegetation elements and complex habitat which offered a variety of niches and supported high number of butterfly species [11]. More species of the Nymphalidae and Pieridae in forested area shows both the generalist and habitat preference butterflies [8, 12]. The species richness of butterflies indicates the habitat quality due to their sensitivity to changes of host plant and nectar sources [4, 13]. The Shannon-Weiner index showed similar mode of diversity value with highest in forested area (H'=3.74), the recreation area (H'=3.40) and the lowest was residential area (H'=2.38). Lower H' in residential area is attributed by low species evenness index dominated by two butterflies species, *Yptima ceylonica* and *Appias libythea olferna*. The result also reflected a homogenous habitat in the residential area which offers less food resources and shelters.

The present study shows that the habitat quality influences the abundance and species diversity of butterfly. The forested area which is situated in Gunung Nuang is ecologically important for the insect fauna besides as a water catchment area for the Langat Dam supplying water to Kuala Lumpur.

Acknowledgements – The authors would like to thank the Forestry Department of Selangor State for permission to conduct the samplings at Gunung Nuang Forest Reserve. This research is funded by UKM-GUP-ASPL-07-04-048.

REFERENCES

1. Corbet A.S. and Pendlebury H.M. (1956) *The Butterflies of the Malay Peninsula* (2nd Ed.). Oliver and Boyd, London.

2. Holloway J.D., Bradley J.D. and Carter D.J. (1987) *Lepidoptera*. British Museum Natural History, London.

3. Corbet A.S. and Pendlebury H.M. (1992) *The Butterflies of the Malay Peninsula* (4th Ed.). Oliver and Boyd, London.
4. Nelson S.M. (2007) Butterflies (Papilionoidea and Hesperioidea) as potential ecological indicators of riparian quality in the semi-arid western United Sates. *Ecological Indicators* **7**: 469-480.
5. Ozden O., Ciesta W.M., Fuller W.J. and Hodgson D.J. (2008) Butterfly diversity in Mediterranean islands and in Pentadaktylos *Pinus brutia* forets of Cyprus. *Biodiversity Conservation* **17**: 2821-2832.
6. Devy M.S. and Davidar P. (2001) Response of wet forest butterflies to selective logging in Kalakad-Mundanthurai Tiger Reserve: Implications for conservation. *Current Science* **80**: 400-405.
7. Sawchik J., Dufrene M. and Lebrun P. (2005) Distribution patterns and indicator species of butterfly assemblages of wet meadows in southern Belgium. *Belgian Journal of Zoology* **135**: 43-52.
8. Fleming W.A. (1975) *Butterflies of West Malaysia and Singapore*. Longman, Malaysia.
9. Robinson, G.S. (1991) *Alpha, PC Version GW Basic*. Natural History Museum, London.
10. Shelton M.D. and Edwards C.R. (1983) Effects of weeds on the diversity and abundance of insects in soybeans. *Environmental Entomology* **12**: 296-299.
11. Ramos, F, A. 2000. Nymphalid butterfly communities in an Amazonian forest fragment. *Journal of Research on the Lepidoptera* 35: 29-41.
12. Yong, H. S. (1984) *Malaysian Butterflies: An Introduction*. Tropical Press, Kuala Lumpur.
13. Thomas J.A., Bourn N.A.D., Clarke R.T., Stewart K.E., Simcox D.J., Pearman G.S., Curtis R. and Goodyear B. (2001) The quality and isolation of habitat patches both determine where butterflies persist in fragmented landscapes. *Proceeding of Royal Society of London Bulletin* **268**: 1791-1796.

Journal of Science and Technology in the Tropics (2009) **5**: 111-116

Generalized lag synchronization in chaotic systems

Prasanta Chatterjee[1*], Swarup Poria[2] and Anindita Tarai[3]
[1]Department of Mathematis, Visva Bharati University, Santiniketan-731 235, India
Present address: Plasma Research Laboratory, Department of Physics, University of Malaya, 50603Kuala Lumpur, Malaysia
(E-mail: prasantachatterjee1@rediffmail.com)
[2]Department of Applied Mathematics, University of Calcutta, Kolkata, West Bengal, India
[3]Department of Mathematics, Aligunj R.R.B. High School, Midnapore (West), West Bengal, India

Received: 10-07-2009, accepted 24-07-2009

ABSTRACT This paper introduces generalized lag synchronization (GLS) of two chaotic dynamical systems, which includes complete synchronization, anti synchronization, lag synchronization, general projective synchronization and full state hybrid lag projective synchronization (FSHLPS). Systematic GLS schemes are proposed respectively for the continuous and discrete dynamical systems. Finally, simulation results are given to verify the effectiveness of the developed schemes.

Keywords generalized lag synchronization – chaotic systems – continuous – discrete

INTRODUCTION

The phenomenon of synchronization of coupled chaotic systems has received a great deal of attention in the last fifteen years. Synchronization is found in a variety of natural systems like fireflies, chirping crickets, and neural systems. It is also useful for secure communication, ecological systems, and artificial systems of information science in order to enable a well coordinated behavior in time. Pecora and Carroll [1] introduced the mechanism for complete synchronization of chaotic systems in 1990. Let us consider two dynamical systems which are uni-directionally coupled as follows.

$dx/dt = F(x)$ *drive system* (a)
$dy/dt = G(x,y)$ *response system* (b)

These two systems are called synchronized completely if $\lim_{t\to\infty}(y_i - x_i) = 0$ for all i.

The idea of generalized synchronization (GS) was proposed by Rulkov, Sushchik and Tsimring [2] in 1995. The systems (a) and (b) are said to be synchronized in the generalized sense if $\lim_{t\to\infty}(y_i - f(x_i)| = 0 \ \forall \ i$. In 1996 Kocarev and Parlitz [3] formulated a condition for the occurrence of GS of continuous dynamical systems. Yang and Chua [4] proposed GS of continuous dynamical systems via linear transformations in 1999. Anti synchronization (AS) was observed by Kim *et al.* [5] in chaotic oscillators.

The systems (a) and (b) are anti synchronized if $\lim_{t\to\infty}(y_i + x_i) = 0$ for all i. The lag synchronization (LS) was observed by Rosenblum *et al.* [6] in 1997. The systems (a) and (b) are said to be lag synchronized if $\lim_{t\to\infty}|y_i - x_i(t - \tau)| = 0$ for all i. LS has more practical application as time delay is inevitable in the real world. It is well known that instantaneous signal processing is not physical because any real physical signal will take some time to flow from the transmitter to the receiver. We call the above defined lag synchronization as complete lag synchronization (CLG). Mainieri and Rehacek [7] reported projective synchronization such that $\lim_{t\to\infty}(y_i / x_i) = \alpha$ for all, where α is a real constant. Qunjiao, Zhang and Lu [8] reported FSHLPS of chaotic systems. Two systems are in full state hybrid lag projection synchronization (FSHLPS) if $\lim_{t\to\infty}(y_i(t)/x_i(t-\tau)) = \alpha_i$ for all I, where α_i's are real constants and not necessarily all equal.

In this paper, we introduce a new kind of chaos synchronization as generalized lag synchronization (GLS). The drive system (a) and response system (b) are said to be generalized lag synchronized if there exist a nonzero constant matrix Λ (not necessarily

Journal of Science and Technology in the Tropics (2009) **5**: 85

Editorial

REBRANDING JOSTT

The Journal of Science and Technology in the Tropics was launched by COSTAM five years ago with a view to communicate research findings of particular relevance to the tropics. Two issues have been published annually.

JOSTT has been successfully listed in SCOPUS and we are pursuing its listing in ISI, hopefully within three years.

The Editorial Board comprises about 20 eminent scientists covering different scientific disciplines.

JOSTT is supported by the Academy of Sciences Malaysia (ASM), and a Steering Committee comprising representatives of ASM and COSTAM to manage the Journal. The Steering Committee at its recent meeting reviewed the progress made by the Journal and took steps to increase its circulation.

The Steering Committee also felt that the Journal should have its own character and uniqueness and not be just another Science and Technology journal.

The journal therefore will welcome research papers of relevance to the tropics not only from senior scientists but also from the young ones (below 40 years). Each issue of the Journal will dedicate some pages to articles contributed by young scientists who will receive special commendations for papers accepted for publication.

Scientists are also encouraged to submit short communications for quick dissemination of their research findings.

The journal will also invite award winning scientists to contribute review articles highlighting the research work which won them the Award.

Datuk Dr Mohinder Singh JP
President COSTAM and Co-Chairman JOSTT

Journal of Science and Technology in the Tropics (2009) 5: 111-116

diagonal) such that $\lim_{t\to\infty}(y_i - \Lambda x_i(t-\tau)) = 0$, $\tau \geq 0$ Obviously, the FSHLPS is a special case of GLS as FSHLPS can be obtained from GLS by choosing λ as a diagonal matrix. Now choosing the matrix Λ equals to I, $-I$ and αI respectively one can obtain complete lag synchronization, anti-lag synchronization and projective lag synchronization respectively. Dynamical schemes are proposed to realize the GLS. Results are illustrated using the continuous systems of hyper-chaotic Rossler system [9], hyper-chaotic Lorenz system [10], the discrete systems of the 3-D generalized Hennon map [11] and 3-D Baier-Klein map [12]. The numerical simulation results are presented to show the effectiveness of the developed method.

GLS SCHEMES

First we shall propose the GLS scheme for continuous chaotic (hyperchaotic) systems. Consider a class of n-dimensional chaotic (hyperchaotic) systems in the form of

$$dx/dt = F(x) \quad (1)$$

where

$x(t) = (x_1(t), x_2(t),..., x_n(t))^T \in \Re^n$

is the state vector and $F(x) = (f_1(x), f_2(x), f_n(x))^T \in \Re^n$ is a continuous nonlinear vector function. We consider system (1) as drive system. The response system is taken as

$$dy/dt = G(y)U(t) \quad (2)$$

where

$y(t) = (y_1, y_2, y_3,..., y_n)^T \in \Re^n$,

$G(y) = (g_1(y), g_2(y),..., g_n(y))^T \in \Re^n$ and

$U(t) = (u_1(t), u_2(t),..., u_n(t))^T \in \Re^n$ is

the controller vector to be determined for synchronization.

Let us define the error vector of the GLS as $e(t) = y(t) - \Lambda x(t-\tau)$, where $e(t) = (e_1(t), e_2(t), e_3(t),..., e_n(t))^T \in \Re^n$ and Λ is an $n \times n$ real matrix. Therefore the error system is

$$de/dt = G(y) - \Lambda F(x(t-\tau)) + U(t) \quad (3)$$

Now our task is to choose suitable

$U(t) = V(e(t)) + H(x(t-\tau), y(t))$, where $V(e(t)) = (v_1 e(t), v_2 e(t)),..., v_n(e(t))^T \in \Re^n$ such that the above error system is reduced to the following form

$$de/dt = Pe(t) \quad (4)$$

where P is a $n \times n$ constant matrix.

Theorem 1

If all eigenvalues of the matrix P have negative real part, *i.e* they lie on the left half of the complex plane, the chaotic system (1) would be generalized lag synchronized with chaotic system (2).

Now, consider an n-dimensional discrete chaotic system as

$$x(k+1) = Ax(k) + F(x(k)) \leftrightarrow \textit{drive system} \quad (5)$$

and

$$y(k+1) = By(k) + G(Y(k)) + U \leftrightarrow \textit{slave system} \quad (6)$$

where

$x(t) = (x_1(t), x_2(t),..., x_n(t))^T \in \Re^n$ and

$y(t) = (y_1, y_2, y_3,..., y_n)^T \in \Re^n$,

are the state vectors, $F(x(k))$ and $G(Y(k))$ are continuous nonlinear vector functions and k is the discretized time. A and B are $n \times n$ matrices and U is the vector controller to be suitable chosen later for the synchronization.

Now, we define the error vector for GLS as $e(k) = y(k) - \Lambda x(t-\tau)$ where Λ is an $n \times n$ real matrix, and $\tau \in N$ is the time delay. Then the time evolution of the error system is given by

$$\begin{aligned} e(k+1) &= y(k+1) - \Lambda x(k+1-\tau) \\ &= By(k) + Gy(k) - \Lambda A x(k-\tau) - \Lambda F(x(t-\tau)) + U \\ &= Be(k) + (B\Lambda - \Lambda A)x(k-\tau) + G(y(k)) - \Lambda F(x(k \\ &\quad -\tau)) + U \end{aligned} \quad (7)$$

Now we choose the vector controller U as

$$U = Le(k) - G(y(k)) + \Lambda F(x(k-\tau)) + (\Lambda A - B\Lambda) x(k-\tau) \quad (8)$$

where L_{ij} is an $n \times n$ unknown matrix to be designed. Substituting equation (8) into (7), we obtain the simplified form of the error system as

$$e(k+1) = Pe(k) \quad (9)$$

Theorem 2

The real constants l_{ij} are chosen in such a manner that all eigenvalues of the matrix P having modulus less than 1 then system (7) would be generalized lag synchronized with the system (8).

EXAMPLES OF GLS

Continuous case

The Rossler and Lorenz systems are continuous dynamical systems with different structures. The four dimensional Rossler system is

$$dy_1/dt = -x_1 - x_1$$

$$dy_2/dt = x_1 + a_1 x_2 + x_4$$

$$dy_3/dt = x_1 x_3 + b_1$$

$$dy_4/dt = -c_1x_3 + d_1x_4 \quad (10)$$

This system is hyperchaotic for $a_1 = 0.25$, $b_1 = 3.0$, $c_1 = 0.5$ and $d_1 = 0.05$.

The response system is taken as the hyperchaotic Lorenz system presented by Li et al [14]. The controlled hyperchaotic Lorenz system is described by the following equations

$$\begin{aligned} dy_1/dt &= a(y_1 - y_2) + u_1(t) \\ dy_2/dt &= by_1 + cy_2 - y_1y_3 + y_4 + u_2(t) \\ dy_3/dt &= -dy_3 + y_1y_2 + y_4 + u_2(t) \\ dy_4/dt &= -ry_1 + u_4(t) \end{aligned} \quad (11)$$

This system is hyper-chaotic for the parameters

a=35, b=7, c=12, d=3 and r=5 and $u_1(t) = u_2(t) = u_3(t) = u_4(t) = 0$

Let us define the generalized lag synchronization error states as

$$e_i(t) = y_i(t) - \lambda_{i1}x_1(t-\tau) - \lambda_{i2}x_2(t-\tau) - \lambda_{i3}x_3(t-\tau)$$
$$i = 1,2,3,4 \quad (12)$$

We obtain the error system as

$$\begin{aligned} de_1/dt = {} & a(e_2 - e_1) + (-a\lambda_1 + a\lambda_{21} - \lambda_{12})x_1(t-\tau) + \\ & (-a\lambda_{12} + a\lambda_{22} + \lambda_{11} - a\lambda_{22})x_2(t-\tau) + \\ & (-a\lambda_{13} + a\lambda_{23} + \lambda_{11} - c_1\lambda_{14})x_3(t-\tau) + \\ & (-a\lambda_{14} + a\lambda_{24} - \lambda_{12} - d_1\lambda_{14})x_4(t-\tau) - \\ & \lambda_{13}x_1(t-\tau) - b_1\lambda_{13} + u_1(t) \end{aligned}$$

$$\begin{aligned} de_2/dt = {} & be_1 + ce_2 + e_4 + (-b\lambda_{11} + c\lambda_{21} + \lambda_{41} - \lambda_{22}) \\ & x_1 + (-b\lambda_{12} + c\lambda_{22} + \lambda_{42} + \lambda_{21} - a\lambda_{22})x_3(t-\tau) \\ & + (-b\lambda_{13} + c\lambda_{23} + \lambda_{43} + \lambda_{21}) + c_1\lambda_{24})x_3(t-\tau) \\ & + (-b\lambda_{14} + c\lambda_{23} + \lambda_{44} - \lambda_{22} + d_1\lambda_{24}) \\ & x_4(t-\tau) - \lambda_{23}x_1(t-\tau)\, x_3(t-\tau) - b_1\lambda_{23} \\ & -y_1y_2 + u_2(t) \end{aligned}$$

$$\begin{aligned} de_3/dt = {} & -de_3 + (-d\lambda_{31} - \lambda_{32})x_1(t-\tau) + (-d\lambda_{32} + \\ & \lambda_{31} - a\lambda_{32})x_2(t-\tau) + (-d\lambda_{33} + \lambda_{31} + c_1\lambda_{34}) \\ & x_3(t-\tau) + (-d\lambda_{34} - \lambda_{32} - d_1\lambda_{34})x_4(t-\tau) - \\ & \lambda_{33}x_1(t-\tau)\, x_3(t-\tau) + y_1y_2 - b_1\lambda_{23} + u_3(t) \end{aligned}$$

$$\begin{aligned} de_4/dt = {} & -re_1 + (-r\lambda_{41} - \lambda_{42})x_1(t-\tau) + (-r\lambda_{42} + \\ & \lambda_{41} - a\lambda_{42})x_2(t-\tau) + (-r\lambda_{43} + \lambda_{41} + d_1\lambda_{44}) \\ & x_4(t-\tau) - \lambda_{11}x_1(t-\tau)\, x_3(t-\tau) - b_1\lambda_{43} + \\ & u_3(t) \end{aligned} \quad (13)$$

Now, we choose the control function vector

$H(x(t-\tau), y(t)) =$

$(H_1(x(t-\tau), y(t)), H_2(x(t-\tau), y(t)),$
$H_3(x(t-\tau), y(t)), H_4(x(t-\tau), y(t))$

where

$$\begin{aligned} H_1 = {} & (-a\lambda_{11} + a\lambda_{21} - \lambda_{12})x_1(t-\tau) + \\ & (-a\lambda_{12} + a\lambda_{22} + \lambda_{11} - a\lambda_{12})x_2(t-\tau) + \\ & (-a\lambda_{13} + a\lambda_{23} + \lambda_{11} + c_1\lambda_{14})x_3(t-\tau) + \\ & (-a\lambda_{14} + a\lambda_{24} + \lambda_{12} - d_1\lambda_{14})x_4(t-\tau) + \\ & \lambda_{13}x_1(t-\tau) + b_1\lambda_{13} \end{aligned}$$

$$\begin{aligned} H_2 = {} & (-b\lambda_{11} + c\lambda_{21} + \lambda_{41} - \lambda_{22})x_1(t-\tau) \\ & - (b\lambda_{12} + c\lambda_{22} + \lambda_{42} + \lambda_{21} - c\lambda_{22})x_2(t-\tau) \\ & - (b\lambda_{13} + c\lambda_{23} + \lambda_{43} + \lambda_{21} + c_1\lambda_{24})x_3(t-\tau) \\ & + (b\lambda_{14} + c\lambda_{23} + \lambda_{44} - \lambda_{22} - d_1\lambda_{24})x_4(t-\tau) \\ & - \lambda_{23}x_1(t-\tau)\, x_3(t-\tau) - b_1\lambda_{23} + y_1y_2 \end{aligned}$$

$$\begin{aligned} H_3 = {} & (-d\lambda_{31} - \lambda_{32})x_1(t-\tau) + \\ & (-d\lambda_{32} + \lambda_{31} - a\lambda_{32})x_2(t-\tau) + \\ & (-d\lambda_{33} + \lambda_{31} + c_1\lambda_{34})x_3(t-\tau) + \\ & (-d\lambda_{34} - \lambda_{32} - d_1\lambda_{34})x_4(t-\tau) - \\ & \lambda_{33}x_1(t-\tau)x_3(t-\tau) + y_1y_2 - b_1\lambda_{33} \end{aligned}$$

$$\begin{aligned} H_4 = {} & (-r\lambda_{41} - \lambda_{42})x_1(t-\tau) + \\ & (-r\lambda_{42} + \lambda_{41} - a\lambda_{42})x_2(t-\tau) + \\ & (-r\lambda_{43} + \lambda_{41} + c_1\lambda_{44})x_3(t-\tau) + \\ & (-r\lambda_{44} - \lambda_{42} - d_1\lambda_{44})x_4(t-\tau) - \\ & \lambda_{43}x_1(t-\tau)x_3(t-\tau) - b_1\lambda_{43} \end{aligned} \quad (14)$$

And

$$A = \begin{pmatrix} a-1 & -2a & 0 & 0 \\ -b+1 & -1-c & 0 & -1 \\ 0 & 0 & d-1 & -d \end{pmatrix} \quad (15)$$

Therefore the controllers are given by,

$$= A(e_1(t), e_2(t), e_3(t), e_4(t))^T + H(x(t-\tau), y(t))$$

Now the dynamical system for the error is given as

$$\begin{aligned} de_1/dt &= -e_1 - ae_2 \\ de_2/dt &= e_1 - ae_2 \\ de_3/dt &= -e_3 - de_4 \\ de_4/dt &= ce_3 - e_4 \end{aligned} \quad (16)$$

Here

$$P = \begin{pmatrix} -1 & -a & 0 & 0 \\ 1 & -1 & 0 & 0 \\ 0 & -1 & -d & \end{pmatrix} \quad (17)$$

All eigenvalues of the matrix P have negative real part. Therefore $e_i(t) \to 0$ *as* $t \to \infty$ i.e, GLS between the Rossler system and Lorenz system is achieved.

Journal of Science and Technology in the Tropics (2009) 5: 111-116

Discrete case

We consider the driving system as the 3-D generalized Henon Map as the driving system

$$x_1(k+1) = b\,x_3(k)$$
$$x_2(k+1) = b(1+x_2(k) - ax_3^2(k))$$
$$x_3(k+1) = 1+x_1(k) - a\,(1+x_2(k) - ax_3^2(k))^2 \quad (18)$$

where $a = 0.158$ and $b = 0.06$. The 3-D Baier-Klein map is chosen as driving system

$$y_1(k+1) = -0.1x_3(k) - y_2(k)^2 + 1.76 + u_1$$
$$y_2(k+1) = y_2(k) + u_2$$
$$y_3(k+1) = y_2(k) + u_3 \quad (19)$$

Therefore the A B and $F(x(k))$, $G(x(k))$ in equations (5) and (6) are as follows

$$A = \begin{pmatrix} 0 & 0 & b \\ 0 & b & 0 \\ 1 & -2a & 0 \end{pmatrix},$$
$$B = \begin{pmatrix} 0 & 0 & -0.1 \\ 1 & 0 & 0 \\ 0 & 1 & 0 \end{pmatrix}, \quad (20)$$

$$F(x(k)) = \begin{pmatrix} 0 \\ b(1-ax_3(k)^2 \\ 1-a[1+x_2(k)^2+a^2x_3(k)^4-2ax_3(k)^2-2ax_2(k)x_3\,2ax_3(k)^2 \end{pmatrix} \quad (21)$$

$$G(x(k)) = \begin{pmatrix} -y_2(k)^2+1.76 \\ 0 \\ 0 \end{pmatrix} \quad (22)$$

Let us define the generalized lag synchronization error states as

$$e_i(k+1) = y_i(k+1) - \lambda_{i1}x_1(k+1-\tau) - \lambda_{i2}x_2(k+1-\tau) - \lambda_{i3}x_3(k+1-\tau) - \lambda_{i4}x_4(k+1-\tau)\ i = 1,2,3,4 \quad (23)$$

Here the error dynamics is given by

$$e_1(k+1) = -0.1e_3(k) - (0.1\lambda_{11}+\lambda_{13})x_1(k-\tau) + (-a\lambda_{12} + a\lambda_{22} + \lambda_{11} - a\lambda_{12})x_2(k-\tau) + (-a\lambda_{13} + a\lambda_{23} + \lambda_{11} + c_1\lambda_{14})x_3(k-\tau) + (-a\lambda_{14} + a\lambda_{24} - \lambda_{12} - d_1\lambda_{14})x_4(k-\tau) - x_1(k-\tau) - b_1\lambda_{13} + u_1(t)$$

$$e_2(k+1) = e_1(k) + (\lambda_{21}-\lambda_{23})x_1(k-\tau) + (-b\lambda_{22}+\lambda_{22}-2a\lambda_{22})x_2(k-\tau) + (\lambda_{23}-b\lambda_{21})x_3(t-\tau) + a(\lambda_{22}-2a\lambda_{23})x_3(k-\tau)^2 + a\lambda_{23}x_2(k-\tau)^2 - 2a^2\lambda_{23}x_2(k-\tau)x_3(k-\tau)^2 + \lambda\_23\,x_3(k-\tau)^4 - y_2(k)^2 + u_2$$

$$e_3(k+1) = e_2(k) + (\lambda_{31}-\lambda_{33})x_1(t-\tau)(-d\lambda_{32}+\lambda_{32} - 2a\lambda_{33})x_2(t-\tau) + (\lambda_{33}-b\lambda_{31})x_3(t-\tau) + a(\lambda_{32}-2a\lambda_{33})x_3(k-\tau)^2 + a\lambda_{33}x_2(k-\tau)^2 - 2a^2\lambda_{33}x2(k-\tau)x_3(k-\tau)^2 - x_3(k-\tau)^4 + y_2(k)^2 + a\lambda_{23} + u_3 \quad (24)$$

We made the following choice for the controllers

$$u_1 = -0.1e_1(k) - (0.1\lambda_{11}+\lambda_{13})x_1(k-\tau) + (0.1\lambda_{12}+b\lambda_{12}-2a\lambda_{13})x_2(k-\tau)\ (0.1\lambda_{13}+b\lambda_{11})x_3(k-\tau) - a(\lambda_{12}-2a\lambda_{13})x_3(k-\tau)^2 - a\lambda_{13}x_2(k-\tau)^2 + 2a^2\lambda_{13}x_2(k-\tau)x_3(k-\tau)^2 - a3\lambda_{13}x_3(k-\tau)^4 - y_2(k)^2 - a\lambda_{13} - 1.76$$

$$u_1 = -0.8e_2(k) + (\lambda_{21}-\lambda_{23})x_1(k-\tau) + (-b\lambda_{22}+\lambda_{22} - 2a\lambda_{22})x_2(k-\tau) - (\lambda_{23}-b\lambda_{21})x_3(t-\tau) - a(\lambda_{22} - 2a\lambda_{23})x_3(k-\tau)^2 - a\lambda_{23}x_2(k-\tau)^2 + 2a^2\lambda_{23}x_2(k-\tau)x_3(k-\tau)^2 - a^3\lambda_{23}x_3(k-\tau)^4 + y_2(k)^2 - a\lambda_{23}$$

$$u_3 = -7.5e_3(k) - e_2(k) - (\lambda_{31}-\lambda_{33})x_1(t-\tau) + (-d\lambda_{32}+\lambda_{32}-2a\lambda_{33})x_2(t-\tau) - (\lambda_{33}-b\lambda_{31})x_3(t-\tau) - a\lambda_{33}x_3(k-\tau)^2 + 2a^2\lambda_{33}x_2(k-\tau)x_3(k-\tau)^2 - a^3\lambda_{23}x_3(k-\tau)^4 + y_2(k)^2 + a\lambda_{23} \quad (25)$$

With the above choice of the controllers, the error system reduces to

$$e_1(k+1) = -0.7e_1(k) - 0.1e_3(k)$$
$$e_2(k+1) = e_1(k) - 0.8e_2(k)$$
$$e_3(k+1) = 0.75e_3 \quad (26)$$

We obtain

$$P = \begin{pmatrix} -0.7 & 0 & -0.1 \\ 1 & -0.8 & 0 \\ 0 & 1 & -0.75 \end{pmatrix} \quad (27)$$

Clearly all eigenvalues of the matrix P having modulus less than 1. Therefore, the generalized Henon map and 3-D Baier-Klein map will be generalized lag synchronized.

CONCLUSION

In this paper, we have introduced the new concept of generalized lag synchronization (GLS). GLS is more general than full state hybrid lag projective synchronization (FSHLPS). We have proposed the schemes for obtaining GLS between two chaotic systems for both discrete and continuous and discrete dynamical systems. There is no restriction on the delay parameter in our proposed method. The method is based on Lyapunov stability theory. Numerical simulation results for the time evolution of the GLS errors are shown in Figures 1-7.

GLS errors $e_1(t)$, $e_2(t)$, $e_3(t)$ and $e_4(t)$ for Rossler and Lorenz systems are shown in Figures 1 to 4

respectively. GLS errors $e_1(t)$, $e_2(t)$ and $e_3(t)$ between Hennon map and Baier-Klein map are shown in Fig.5 to Fig.7 respectively. Based on these figures our proposed scheme seemed to work very well.

Chaos synchronization between two remote chaotic systems actually means that some information has successfully been transmitted from one end to the other. This fact leads to the foundation of a chaos-based communication system. By keeping some part of the involved chaotic systems secret, a third party not knowing the secret key will not be able to reconstruct the information transmitted. To overcome the security problems of most traditional chaos-based secure communication schemes, one widely accepted measure is to use more complex chaotic systems rather than three dimensional systems. We hope our GLS scheme will be very useful for designing a more secure chaos based communication systems.

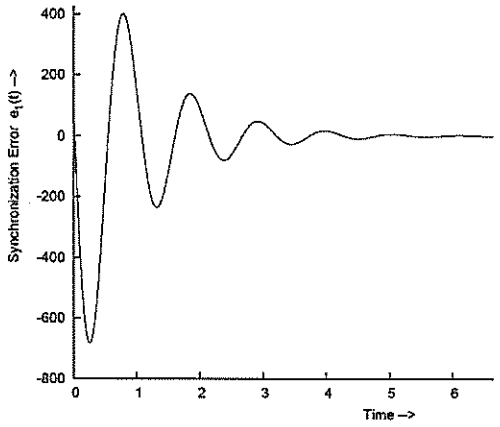

Figure 1. Time evolution of synchronization error $e_1(t)$ between Roseller system and Lorenz system.

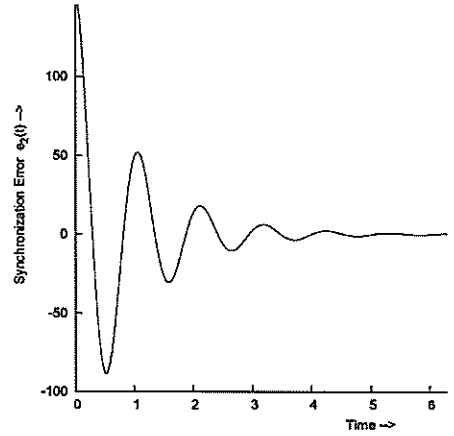

Figure 2. Time evolution of synchronization error $e_2(t)$ between Roseller system and Lorenz system.

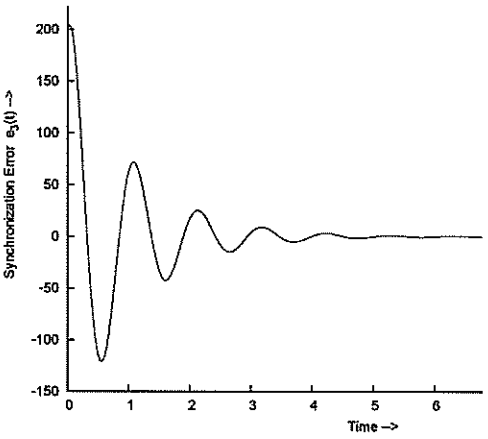

Figure 3. Time evolution of synchronization error $e_3(t)$ between Roseller system and Lorenz system.

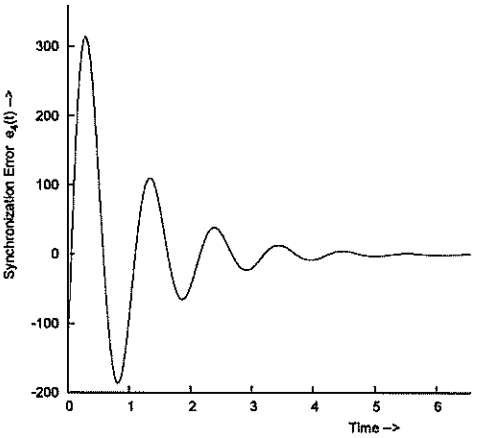

Figure 4. Time evolution of synchronization error $e_4(t)$ between Roseller system and Lorentz system.

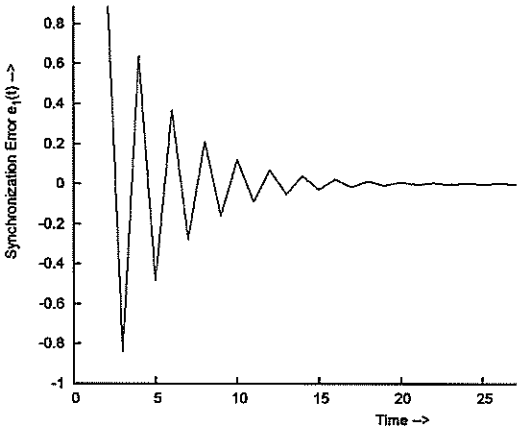

Figure 5. Time evolution of synchronization error $e_5(t)$ between Henon map and Baier-Klein map.

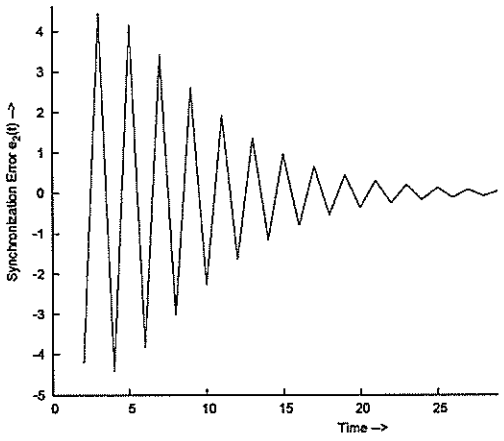

Figure 6. Time evolution of synchronization error $e_2(t)$ between Henon map and Baier Klein map.

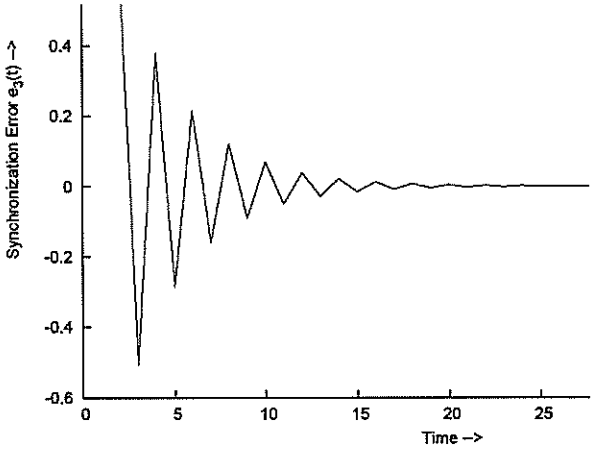

Figure 7. Time evolution of synchronization error $e_3(t)$ between Hennon map and Baier-Klein map.

REFERENCES

1. PecorraL.M.andCarrollT.L.(1990)Synchronization in chaotic systems. *Physical Review Letters* **64**: 821-824.
2. Rulkov N.F., Sushchik M.M., Tsimring L.S. and Abarbanel H.D.I. (1995) Generalized synchronization of chaos in directionally coupled chaotic systems. *Physical Reiew E* **51**: 980 - 994.
3. Kocarev L. and Parlitz U. (1996) Generalized synchronization, predictability, and equivalence of unidirectionally coupled dynamical systems. *Physical Review Letters* **76**: 1816 – 1819.
4. Yang T. and Chua L.O. (1999) Generalized synchronization of chaos via linear transformations. *International Journal of Bifurcation and Chaos* **9**: 1215-219.
5. Kim C.M., Rim S., Kye W.H., Ryu J.W. and Park Y.J. (2003) Anti synchronization of chaotic oscillators. *Physics Letters A* **320**: 139-46.
6. Rosenblum M.G., Pikovsky A.S. and Kurths J. (1997) From phase to lag synchronization in coupled chaotic oscillators. *Physical Review Letters* **78**: 4193.
7. Mainieri R. and Rehacek J. (1999) Projective synchronization in three-dimensional chaotic systems. *Physical Review Letters* **82**: 3042-3045.
8. Zhang Q. and Lu J. (2007) Full state hybrid lag projective synchronization in chaotic (hyperchaotic) systems. *Physics Letters A* **361**: 231
9. Rossler O.E., (1979) An equation for hyperchaos. *Physics Letters A* **71**: 155.
10. Li W.Y., Tang S. and Chen G. (2005) Hyperchaos evolved from generalized Lorenz equation. *Inernational Journal of Circuit Theory Appl*ications **33:** 235.
11. Stefanski K. (1998) Modelling chaos and hyperchaos with 3-D maps. *Chaos, Solitons and Fractals* **9**: 83-93.
12. Baier G. and Klein M. (1990) Maximum hyperchaos in generalized HÃnon maps. *Physics Letters A* **151**: 281-284.

Journal of Science and Technology in the Tropics (2009) **5**: 117-123

Treatment of water by dielectric barrier discharge

D. P. Subedi[1], R. B. Tyata[2], A. Khadgi[1] and C. S. Wong[3]
[1]Department of Natural Science, Kathmandu University, Dhulikhel, Nepal
(E-mail: deepaksubedi2001@yahoo.com)
[2]Department of Physics, Khwopa College, Dekocha, Bhaktapur, Nepal
[3]Plasma Research Laboratory, Physics Department, University of Malaya, 50603 Kuala Lumpur, Malaysia

Received 05-08-2009; accepted 10-09-2009

Abstract This research work reports the results concerning the generation of dielectric barrier discharge (DBD) in water and its use for the treatment of water collected from different sources in Kathmandu Valley, Nepal. The discharge has been produced by applying AC high voltage (up to 20 kV peak-to-peak) source of frequency 10–30 kHz across annular electrodes. The main objective of the work was to develop a system in which discharge through water could be produced for the purpose of direct treatment of the water. Water from different sources such as river, well, stone spout and tap was treated by this method. The general evaluation of the efficiency of the treatment for water disinfection was made. The experimental results show that the qualities of water such as pH, conductivity, chlorides and total hardness of water changed slightly after treatment. However, the coliforms and chemical oxygen demand (COD) were significantly reduced in the treated samples. A remarkable increase in the amount of dissolved oxygen (DO) was also observed after the treatment.

Keywords DBD – pH – conductivity – total hardness – coliforms – DO – COD

INTRODUCTION

The area of water purification by ozone synthesis is an industrially accepted application of electrical discharges [1, 2]. Ozone is required in huge quantities for drinking water and waste water treatment [3-5]. The major advantages of the ozonation process for water treatment are: (a) no need to store and handle toxic chemicals; (b) by-products of ozonation do not have any known adverse effects on health or the environment; (c) ozone is a stronger and faster-acting oxidizer; (d) ozone can safely destroy a broader range of organic contaminants; (e) ozone helps in the removal of colour, odour and suspended solid materials; and (f) ozone is far more efficient in killing bacteria, viruses, spores and cysts.

The ozonation process can be made more competitive by (a) improving the energy efficiency and ozone yield of the ozone generator, (b) developing better ozone-water contactors, and/or (c) catalyzing the chemical reactions of ozone [6]. Electrical discharges taking place in an air or oxygen environment convert oxygen into ozone. In addition to ozone, electrical discharges in air produce a variety of chemically active species, such as $O^{\cdot}$, $OH^{\cdot}$, $N^{\cdot}$, O^{*}_{3}, N^{*}_{2}, N^{*}, OH^{*}, O^{*}_{2}, O^{*}, O^{+}_{2}, N^{+}_{2}, N^{+}, O^{+} [7-10]. These species are short lived and decay before ozone enriched air/oxygen gets into water.

However, if the reactor is designed so that the electrical discharges take place in close proximity to the water surface or directly through the water, some of these species may get into water and destroy the pollutants. In this way, the water treatment unit becomes simpler as there will be no need for a separate electrical discharge reactor for ozone synthesis and tubing to carry ozone enriched air/oxygen. Furthermore, the intense electric fields necessary for electrical discharges are also poisonous to several kinds of microorganisms found in water and show a synergistic poisonous effect when combined with conventional disinfectants such as O_3 and H_2O_2 [11]. The electrical discharges in water may also produce ultraviolet (UV) radiation [12] and shock waves [13] which help in the destruction of pollutants [14]. For these reasons direct electrical discharges in water is clearly the best next-generation technology for water

treatment. This is environment friendly and may prove to be far more effective than conventional oxidants and disinfectants. Patrick *et al.* [15] have reported that conductivity and the total hardness remain at stable values before and after treatment. The WHO acceptable concentration of chloride in drinking water is 250 mg/L and the allowable concentration is 600 mg/L [16]. Bubnov *et al.* [17] have reported that chloride of rainfall runoff and snow melt runoff water decrease after treatment in electrical discharge. Electrical discharges are usually associated with intense electric fields, shock waves, UV radiation, O_3, H_2O_2, etc each of which can kill microorganisms. Therefore, a combination of these factors, as in the case of electrical discharges in water or air, may form a very effective sterilization medium [18-20].

EXPERIMENTAL SETUP

The water treatment system consists of a specially designed DBD with annular electrodes slightly modified so as to make it suitable for direct water treatment in a flow region. It consists of two electrodes: central and outer electrodes. The central electrode is made of brass rod (diameter is 3 mm, length 65 mm) and enclosed by an inner cylindrical glass tube. The outer electrode is made of aluminum foil which wraps around the outer cylindrical glass tube. The gap between the two dielectric layers is 3 mm through which water can easily flow. The water flow rate is controlled by two valves. The experimental setup for water treatment is depicted in Figures 1 and 2. Figure 3 shows the cross-sectional view of the annular electrode system in a DBD. An example of the discharge in water is illustrated in Figure 4

In the water treatment system, the flow of water is regulated by a stopper. The flow rate of water in this reactor is estimated at 0.2 cm^3 per second to 0.4 cm^3 per second. The contact time of the water with the discharge zone in the reactor is 12-24 s which is calculated using the relationship $\tau_{c,l} = [S \times l/g]$ seconds [17], where S is the cross-sectional area of the inter

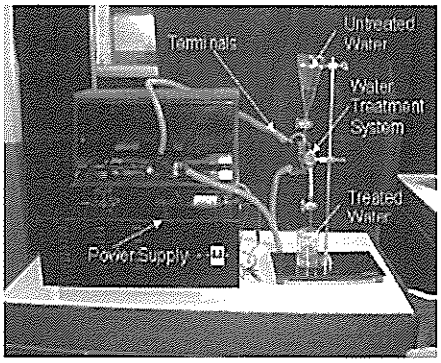

Figure 1. Experimental setup of the water treatment system.

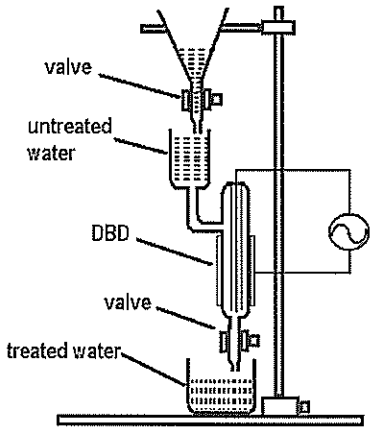

Figure 2. Schematic diagram of water treatment system.

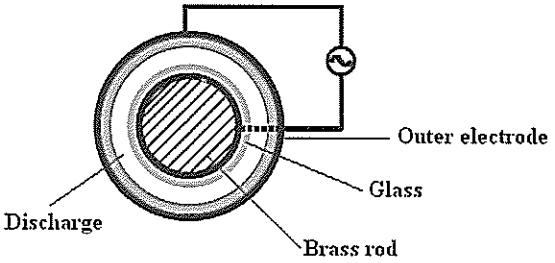

Figure 3. Cross-sectional view of the annular electrode system in a dielectric barrier discharge.

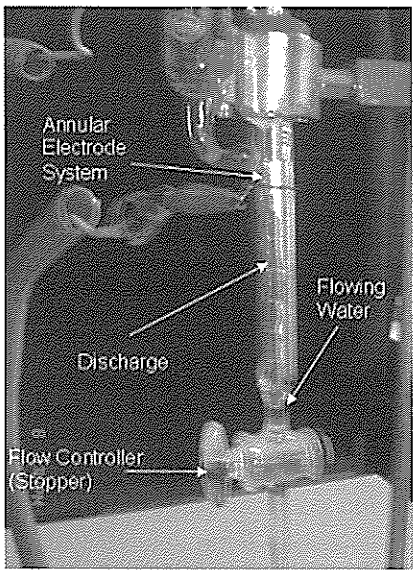

Figure 4. An example of discharge in water.

electrode gap (3 mm), *l* is the length of the reaction zone (6.5 cm) and *g* is the water flow rate in cm^3 per second. Experiments were performed on four types of drinking water: well, river, stone spout and tap.

SELECTION OF PARAMETERS

The physical, chemical and biological parameters of the water investigated in this study are summarized in Table 1. The analyses of the samples were carried out in the Microbiology Laboratory of Khwopa College, Bhaktapur, Nepal.

RESULTS AND DISCUSSION

Analysis of pH

The experimental results of pH analysis of untreated and treated water from well and river are shown in Figure 5, and from stone spout and tap are depicted in Figure 6. The pH value of water collected from river was in the range of 8.5 to 9.3. After the treatment, there was a slight increase in the pH value to the range of 9.1 to 9.3. For the samples collected from four different wells, the pH values varied from 6.8 to 7.8 before treatment. After the treatment the pH values remained in the range of 7 to 7.5 indicating almost no change in the pH values. In the case of water samples collected from stone spout, the pH values ranged from 8.7 to 8.9 while after treatment it showed a slight increase ranging from 8.8 to 9.4.

Conductivity

Results of conductivity measurement of untreated and discharge treated water from well and river are shown in Figure 7, while Figure 8 shows the results for the water samples from stone spout and tap. The conductivity of water collected from different rivers

Table 1. Parameters and the method used for analysis.

Serial No.	Physical parameters	Unit	Method/ Instrument used
1	pH	Scale	pH meter
2	Conductivity	µs/cm	Conductivity meter
3	Chloride	mg/L	Argentometric Titration Method
4	Total hardness	mg/L	EDTA titration
5	coliform	MPN/100mL	Most Probable Number (MPN) Test
6	Dissolved oxygen (DO)	mg/L	Winkler's iodometric method
7	Chemical oxygen demand (COD)	mg/L	Open air reflux method

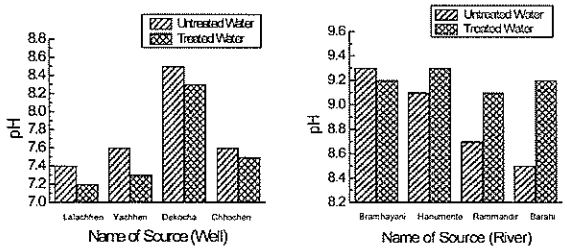

Figure 5. pH of untreated and discharge treated water from wells (a) and rivers (b).

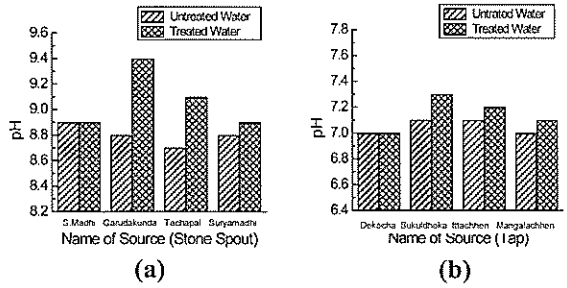

Figure 6. pH of untreated and discharge treated water from stone spout (a) and from tap (b).

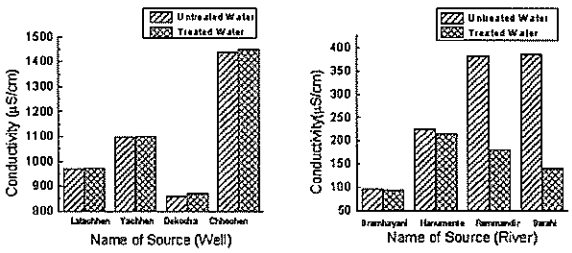

Figure 7. Conductivity of untreated and discharge treated water from wells (a) and river (b).

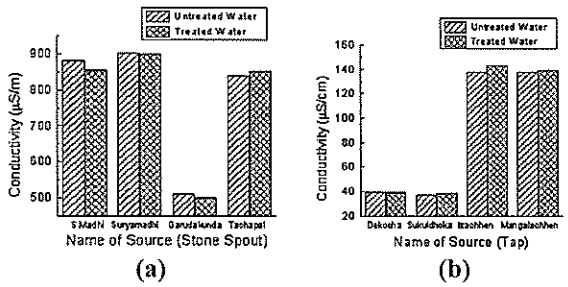

Figure 8. Conductivity of untreated and discharge treated water from stone spout (a) and tap (b).

was in the range of 98 to 386 μScm^{-1} before the treatment. After the treatment, the conductivity was reduced to 94 to 216 μScm^{-1}. The conductivity of water in Bramhayani River (98 μScm^{-1}) was very low compared to that of other rivers. After the treatment the conductivity of the water in this river was reduced to 94 μScm^{-1} whereas for the other rivers, the values of conductivity were in the range of 141 to 216 μScm^{-1}. For the samples collected from the wells, the conductivity ranged from 630 to 876 μScm^{-1}, but with a slight increase after treatment. In the case of water from stone spout, the conductivity ranged from 512 to 883 μScm^{-1}. There seems to be negligible effect of treatment on the conductivity of this source of water. Conductivity of tap water was very low (40 to 138 μScm^{-1}) compared to that of water from other sources. Moreover, there was almost no change in the values of conductivity after treatment for all the samples from four different taps.

Conductivity plays an important role in the generation of discharges and on the production of chemically active species. In deionized water, the discharge is relatively weak. It has been reported that a certain concentration of ion conductivity in the range of 10 to 80 μScm^{-1} may enhances conduction, resulting in a stronger discharge, higher current flow, longer streamer length and an increase in the production of chemically active species. Thus, an increase in the water conductivity further from the optimum value of 10 to 80 μScm^{-1} results in a faster compensation of the space charge electric field on the streamer-head (shorter streamer channel length) [21] and a decrease in the rate of production of chemically active species.

Chloride concentration

The concentration of chloride in water collected from well and river before and after treatment in DBD is depicted in Figure 9, and that for stone spout and tap in Figure 10. The concentration of chloride in the water from rivers selected in our study ranged from 12.8 to 38.2 mg/L. After the treatment, it was in the range of 14.2 to 21.3 mg/L. Water samples from wells had higher chloride concentration of 126.4 to 242.8 mg/L compared to water from the river. After the treatment, the concentration remained in the range of 127 to 242 mg/L. The concentration of chloride in the water from stone spout varied from 71 to 113 mg/L before treatment and it remained in the range of 63 to 113 mg/L after treatment, indicating a very weak effect. For tap water, chloride concentration was lowest, in the range of 8.5 to 38 mg/L. After the treatment, the concentration remained in the range of 14 to 42 mg/L showing a slight increase.

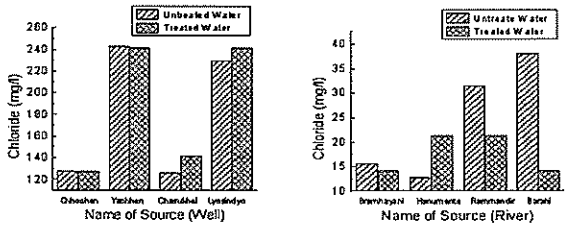

(a) (b)

Figure 9. Chloride concentration in untreated and discharge treated water from well (a) and river (b).

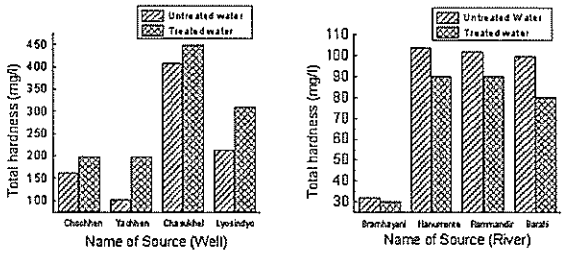

(a) (b)

Figure 11. Total hardness of untreated and discharge treated water from well (a) and river (b).

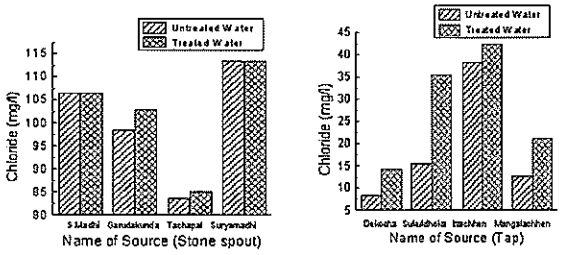

(a) (b)

Figure 10. Chloride concentration in untreated and discharge treated water from stone spout (a) and tap (b).

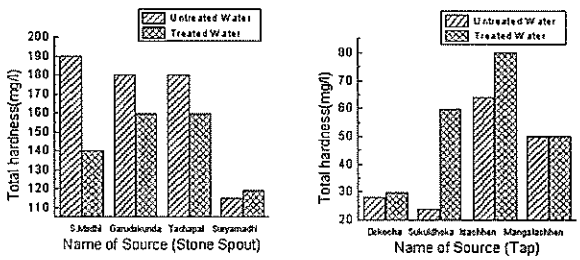

(a) (b)

Figure 12. Total hardness of untreated and discharge treated water from stone spout (a) and tap (b).

Total hardness

The total hardness in untreated and treated samples of water collected from well and river are shown in Figure 11, and that for the samples of water collected from stone spout and tap in Figure 12. The results show that the total hardness of water from the rivers varied from 34 to 104 mg/L before treatment. After the treatment, the hardness was in the range of 30 to 90 mg/L showing a slight reduction in the hardness. For the samples collected from wells, the hardness was quite high (102 to 408 mg/L) and it increased to the range of 200 to 450 mg/L after the treatment. In the case of samples from stone spout, their hardness ranged from 180 to 190 mg/L and after treatment it was reduced to 140 to 160 mg/L. Interestingly, the hardness of tap water was very low (28 to 64 mg/L) compared to the samples from the other sources. After the treatment in DBD there was a slight increase in hardness reaching to a range of 30 to 80 mg/L.

Coliform content

The coliform counts in untreated and discharge treated water samples collected from well and river are presented in Figure 13 and those from stone spout and tap in Figure 14. The coliform content varied widely in different rivers from 28 MPN/100 mL in Hanumante River to 2400 MPN/100 mL in Brahmayani River. After the treatment, the coliform count was reduced to 23-42 MPN/100 mL showing a significant reduction in the number due to the treatment. Similar results were observed in the samples from different wells. For untreated water the coliform count varied from 3 to 1100 MPN/100 mL, which was reduced to 3 to 460 MPN/100 mL after the treatment. For the water samples from stone spout, the coliform count ranged from 20 to 460 MPN/100 mL, and was reduced to 9 to 240 MPN/100 mL after the treatment. The number of coliform in tap water was relatively low (15 to 150 MPN/100 mL) compared to the samples from the other three sources. After the treatment, the coliform content decreased to 7 to 23 MPN/100 mL. These results are significant since the contamination of water by coliform is a major problem in most of the sources of water in the Kathmandu valley. This is the reason why the main focus of the present study was to investigate the effectiveness of DBD treatment in the elimination or at least reduction of coliform in water. In all the samples tested, a significant reduction in the number of coliform bacteria was observed after the treatment. This effective treatment in reducing the coliforms can be attributed to the effect of strong electric field, UV radiation and shockwaves in addition to the effect of ozone.

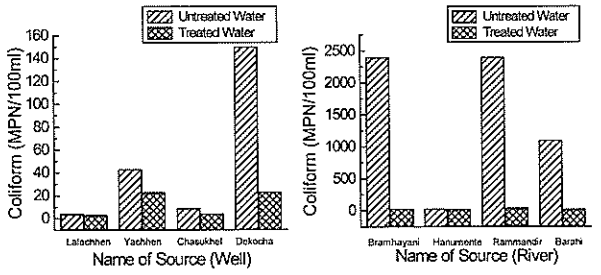

Figure 13. Coliform content in untreated and discharge treated water from well (a) and river (b).

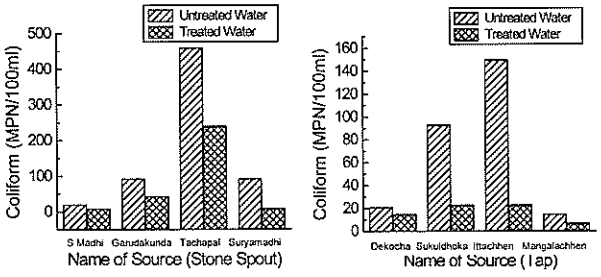

Figure 14. Coliform content in untreated and discharge treated water from stone spout (a) and tap (b).

DO and COD analysis

The dissolved oxygen (DO) of the water samples collected from stone spout and tube well are shown in Figure 15. The values of DO in water from stone spout varied from 7.7 to 8.1 mg/L before the treatment. After the treatment, there was an increase of DO for each sample. For the samples collected from different tube wells, the values of DO ranged from 1.12 to 1.80 mg/L before the treatment. After the treatment in DBD, the amount of DO increased to 1.64 to 4.76 mg/L. The increase in DO was due to the strong oxidizing nature of ozone.

The chemical oxygen demand (COD) in untreated and treated water from tube wells is shown in Figure 16. In this experiment, chemical oxygen demand in water decreased significantly after treatment in DBD. The observed effect of decrease in COD is very important from different technological application point of view. This result suggests the presence of series of chain reactions initiated by ozone dissolved in water. Due to these reactions large

organic molecules in water are fragmentized resulting in a decrease in COD.

Conclusion

Results on the DBD treatment of water samples collected from various sources show a significant reduction in the number of coliform bacteria and COD. DO in water samples increased after the treatment. Further investigations about the effects of DBD on different physical, chemical and biological parameters of drinking water are in progress. In summary, a DBD unit has been developed at relatively lower cost. The design of the system is scalable and can be modified according to the need. This type of low cost technology may help developing nations to provide clean drinking water and may be used in many other industrial applications. Future work in this laboratory will be focused on the generation of DBD in the environments of inert gases like helium and argon in addition to air. Radio frequency generator may also be used to improve the quality of the discharge. The work will be extended to the production of atmospheric pressure glow discharge (APGD) in the near future.

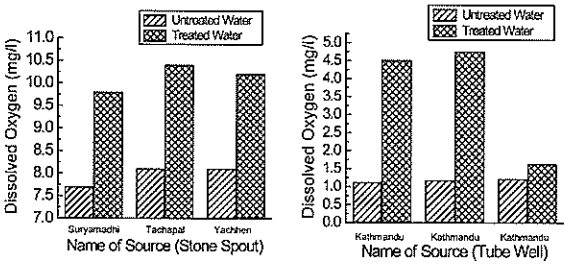

Figure 15. Dissolved oxygen (DO) in untreated and discharge treated water from stone spout (a) and tap (b).

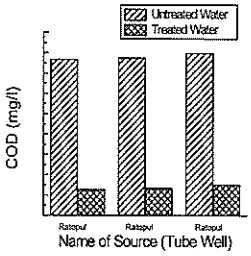

Figure 16. Chemical oxygen demand (COD) in untreated and discharge treated water from tube well.

Acknowledgement – This research was supported by the International Foundation for Science (IFS), Stockholm, Sweden, and the Organization for the Prohibition of Chemical Weapons, The Hague, The Netherlands, through grant No. W/4373-1. We would also like to thank Prof. V. Krishna Murthy of Department of Science and Humanities, PES Institute of Technology, Bangalore, India for his continuous support and valuable suggestion in different stages of the project work.

REFERENCES

1. Eliasson B., Hirth M. and Kogelschatz U. (1987) Ozone synthesis from oxygen in dielectric barrier discharges. *Journal Physics D: Applied Physics* **20**: 1421-1437.
2. Chang M.B. and Wu S.J. (1997) Experimental study on ozone synthesis via dielectric barrier discharges. *Ozone Science Engineering* **19**: 241-254.
3. Glaze W.H. (1987) Drinking-water treatment with ozone. *Environmental Scence and Technology* **21**: 224-230.
4. Rajeswari K.R., Noorsaadah A.R. and Wong C.S. (2001) Effect of temperature on the ozonation of textile waste effluent. *Coloration Technology* **117**: 95-97.
5. Kang J.W., Park H.S., Wang R.Y., Koga M., Kadokami K., Kim H.Y., Lee E.T. and Oh S.M. (1997) Effect of ozonation for treatment of micropollutants present in drinking water source. *Water Science and Technololgy* **36**: 299–307.
6. Malik M.A., Ghaffar A., and Malik S.A. (2001) Water purification by electrical discharges. *Plasma Sources Science and Technology* **10**: 82-91.
7. Eliasson B. and Kogelschatz U. (1991) Non-equilibrium plasma chemical processing. *IEEE Transaction on Plasma Science* **19**: 1063-1077.
8. Chang J.S., Lawless P.A. and Yamamoto T. (1991) Corona discharge processes. *IEEE Transaction on Plasma Science* **19**: 1152-1166.
9. Kulikovski A.A. (1997) Production of chemically active species in the air by a single positive streamer in a non uniform field. *IEEE Transaction on Plasma Science* **25**: 439-446.
10. Naidis G.V. (1997) Modeling of plasma chemical processes in pulsed corona discharges. *Journal of Physics D: Applied Physics* **30**: 1214-1218.
11. Ohshima T., Sato K., Terauchi H. and Sato M.

(1997) Physical and chemical modifications of high-voltage pulse sterilization. *Journal of Electrostatics* **42**: 159-166.

12. Robinson J.W., Ham M. and Balaster A.N. (1973) Ultraviolet radiation from electrical discharges in water. *Journal of Applied Physics* **44**: 72-75.
13. Sunka P., Babicky V., Clupek M. and Stuka C. (1995) Shock Waves@ Marseille III. In ed. Brun R. and Dumitrescu L.Z. (eds.) pp. 455-458. Berlin, Springer.
14. Willberg D.M., Lang P.S., Hochemer R.H., Kratel A. and Hoffman M.R. (1996) Electrohydraulic discharge reactor. *Environmental Science and Technology* **30**: 2526-2534.
15. Patrick N., Robert H., Pierre L. and Maurice L. (2007) An innovative process for the treatment of high loaded surface wtaer for small communities. *Journal of Environmental Engineering Science* **6**: 139-145.
16. World health Organization (2006) Chemical Fact Sheets, Chapter 12. In *Guidelines for drinking-water quality, 3rd edition*. Geneva, World Health Organization.
17. Bubnov A. G., Grinevich V. I., Kuvykin N. A. and Maslova O. N. (2004)The Kinetics of Plasma-induced degradation of Organic pollutants in sewage water. *High Energy Chemistry* **38**: 41–45.
18. Wang X.L., Mizuno A. and Katsura S. (1998) A novel sterilization method using pulsed discharge plasma. *Chinese Physics Letter* **15**: 41-42.
19. Smulders E.H.W.M., Van Heesch B.E.J.M. and Van Paasen S.S.V.B. (1998) Pulsed power corona discharge for air pollution control. *IEEE Transaction on Plasma Science* **26**: 1476-1484.
20. Efremov N.M., Adamiak B.Yu, Blochin V.I., Dadashev S. Ja, Dmitriev K.I., Semjonov V.N., Levashov V.F. and Jusbashev V.F. (2000) Experimental investigation of the action of pulsed electric discharges in liquids. *IEEE Transaction on Plasma Science*. **28**:224-229.
21. Sunka P., Babicky V., Clupek M., Lukes P., Simek M., Schmidt J. and Cernak M. (1999) Generation of chemically active species by electrical discharges in water. *Plasma Sources Science and Technology* **8**: 258-265.

Journal of Science and Technology in the Tropics (2009) **5**: 125-131

Structural breakdown and build-up in Sn/Ag/Cu paste suspensions

R. Durairaj* and Lam Wai Man
Department of Mechanical and Material Engineering, Faculty of Engineering and Science (FES), Universiti Tunku Abdul Rahman (UTAR), Jalan Genting Kelang, Setapak, 53300 kuala Lumpur, Malaysia
(*E-mail: rajkumar@utar.edu.my)

Received 08-09-2009; accepted 10-11-2009

Abstract Lead-free solder paste printing process accounts for majority of the assembly defects in the electronic manufacturing industry. In the stencil printing process, the solder paste must be able to withstand low and high shear rates, which results in continuous structural breakdown and build-up. The study investigates the thixotropic behaviour of lead-free solder pastes (Sn/Ag/Cu) using the structural kinetic model. The structural kinetic model was used to investigate the structural breakdown and build-up in the solder pastes. A hysteresis loop test and constant shear test is utilized to investigate the thixotropic behaviour of the pastes using parallel plate rheometry. In this study, the shear rates were increased from 0.01 s^{-1} to 50 s^{-1} and the second curve was a result of decreasing shear rate from 50 s^{-1} to 0.01 s^{-1}. For the constant shear test, the samples were subjected to five constant shear rates of 0.01 s^{-1}, 0.1 s^{-1}, 1 s^{-1}, 10 s^{-1} and 50 s^{-1}. The constant shear rate test was designed to study the structural breakdown and build-up of the paste materials. The data from the constant shear test was used to calculate the structural parameter, λ values for the solder paste samples. From this investigation, hysteresis loop test was shown to be an effective test method to differentiate the extent of structural recovery in the solder pastes. The results of the structural parameter values obtained from the kinetic model showed a good correlation to the breakdown and build-up of the paste structure.

Keywords lead-free – rheology – thixotropic – stencil printing – solder paste

INTRODUCTION

Solder paste is one of the most widely used interconnection materials in the surface mount technology assembly process. In order to achieve high volume and low cost production, the solder paste should ideally have the following properties: good flow characteristics (rheology), good printability (should be easily deposited), good adhesion (tackiness to hold components during pick and place operation), and good reflow characteristic [1]. These factors must be taken into consideration when selecting the solder paste for a given applications. Solder paste is a homogenous and stable suspension of solder alloy particles suspended in a flux/vehicle system. The flux/vehicle is a combination of solvents, thickeners, binders and fluxing agents [2, 3].

Solder pastes can be classified in two main ways [4]: firstly as a dense suspension; secondly as a homogeneous mixture. As a dense suspension, consisting of about 50% solid and 50% liquid (by volume), the paste can be described in terms of such attributes as volume fraction, particle size distribution and metal content. As a homogeneous and kinetically stable mixture [2], a solder paste can be described in terms of such properties as viscosity, normal forces, surface tension, and density. The constituents and the composition of a given solder paste can have a direct impact on the performance of the sub-processes in the surface mount assembly process – starting from the paste printing process through to the reflow soldering, to the cleaning, inspection and testing. Solder pastes consist of three main constituents [4], namely: (1) solder alloy particles which form the base for the metallic bond, (2) the flux system which helps to promote the formation of the metallic bond by providing a good wetting condition and for cleaning the surfaces, and (3) the vehicle carrier system which facilitates the binding together of the solder powder particles and the flux system together, and

for providing the desired rheological properties for processing and depositing the paste onto the printed circuit board (PCB).

Solder pastes are non-Newtonian fluids which exhibits thixotropic behaviour. The thixotropic is the characteristic of a suspension when it behaves as solids under very small applied stresses but under greater stresses become liquids. When the stresses are removed the suspension settles back into its original consistency. This property is particularly associated with certain colloids which form gels when left to stand but which become sols when stirred or shaken, due to a redistribution of the solid phase [5]. When the shear rate is applied to the system, two kinetic processes appear, breakdown due to applied shear and build-up because of Brownian movement and aggregation of suspended particles and the aggregation in the system is caused by the attractive forces such as van der Waals and repulsive forces due to steric and electrostatic effect on the particles. The repulsive force prevents the particles from approaching close to one another, and as a result, the particles are held together by weak physical bonds. When no force is exerted on the suspension, the particle aggregation can form a spatial network which creates an internal structure. When the suspension is sheared, these weak forces are broken, causing the network to break down into smaller aggregates. These aggregates can be broken down further into smaller flocs.

After a period of time, at a given shear rate, a dynamic equilibrium is reached between the growth and destruction of aggregate. The equilibrium structure is usually a function of the applied shear rate and tends towards greater structural breakdown at higher shear rates. When a thixotropic material is subject to increasing shear rates, the viscosity drops but when the shear rate is removed, the material structure recovers resulting in the hysteresis loop. The structural kinetics approach to the thixotropy, assumes the existence of a shear and time dependent structure [6]. According to this approach, a general mathematical form of the equations of state of a thixotropic material was proposed [6]. It is assumed that there is only one type of structure defined by a scalar parameter. The mathematical description of this phenomenon consists of two equations of state. The first one (constitutive equation) relates the shear stress τ and the shear rate γ with structure parameter, λ

$$\tau = f(\lambda, \dot{\gamma})\dot{\gamma} \qquad (1)$$

and the second one is the kinetics equation that expresses the rate of structural changes as a function of both the shear rate and the structure parameter,

$$\frac{d\lambda}{dt} = g(\lambda, \dot{\gamma}) \qquad (2)$$

In order to understand the structural break-down and build-up of the structure, the equation 2 could also be expressed as following [6]:

$$\frac{d\lambda}{dt} = -K_1(\dot{\gamma})\lambda + K_2(\dot{\gamma})(1-\lambda) \qquad (3)$$

Where $K_1(\dot{\gamma})$ and $K_2(\dot{\gamma})$ are shear rate dependent time parameters for the rate of structural breakdown and build-up of the structure, respectively. As it is usually defined, the structure parameter varies between $\lambda = 1$, corresponding to the initial structure fully developed, and $\lambda = 0$, corresponding to a completely collapsed state when the steady state is finally achieved [6]. The structure parameter can be written in terms of viscosity in a variety of forms, which depends on the proposed constitutive Eq. (1). A new expression relating the structural parameter, λ and the viscosity was proposed to study the step-up (breakdown) experiments and step-down (build-up) of a suspension as shown in Eq. (4) and (5) [7].

$$\lambda_u = \frac{\eta - \eta_e}{\eta_o - \eta_e} \qquad (4)$$

$$\lambda_d = \frac{\eta - \eta_o}{\eta_e - \eta_o} \qquad (5)$$

where λ_u and λ_d refer to step-up and step-down experiments, respectively. η_o and η_e are the values of the apparent viscosity at $t = 0$ and $t \to \infty$, respectively.

Previous studies have also shown that the solder pastes are thixotropic in nature [8-11]. In this paper, the thixotropic behaviour is studied through the structural kinetics model to understand the extent of structural breakdown and build-up in the different Sn/Ag/Cu pastes formulations.

Stencil printing process

In the electronic manufacturing industry, the stencil printing process (Fig. 1) is the most popular method to deposit paste material (solder paste and isotropic conductive adhesives) onto the printed circuit board (PCB). During the stencil printing process, the squeegee generates hydrodynamic pressures creating a paste roll and injects the paste into the apertures. In stencil printing process, two critical sub processes are the aperture filling and aperture release processes [12, 13]. Successful aperture filling and release will greatly depend on the rheology of the paste material

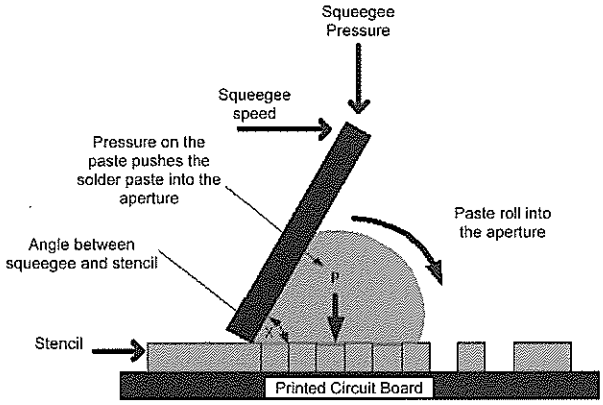

Figure 1. Stencil printing process.

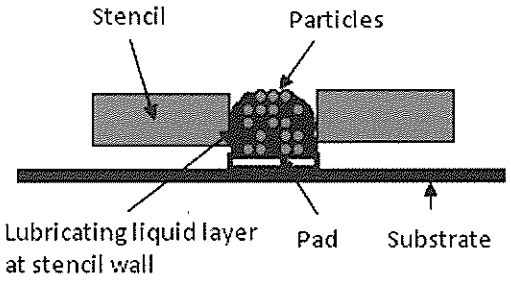

Figure 2. Aperture release process.

Table 1. Constituent of lead free solder pastes investigated.

Paste samples	Particle size distribution (μm)	Particle shape	Flux Medium	Solder alloys/materials
P1	20-45	Spherical	X1 (Rosin Mildly Activated)	96.5% Tin/3% silver/0.5% copper
P2	20-45	Spherical	X2 (Rosin Activated)	96.5% Tin/3% silver/0.5% copper
P3	20-45	Spherical	X3 (No Clean)	96.5% Tin/3% silver/0.5% copper

[14, 15]. When the paste is sheared by the squeegee, the viscosity of the paste must be low enough to flow into the aperture. During the aperture release process, the viscosity of the paste must be large enough to overcome the adhesion forces of the sidewall of the apertures. The aperture release process could be improved with the formation of a lubrication layer between the aperture and stencil wall. A good print is defined by the volume of the paste deposited on the interfaces i.e. the deposited volume is equal to the aperture volume. However in a manufacturing environment, the volume deposited is always less than the aperture volume. This is caused by the adhesion of the paste to the stencil aperture walls. Therefore, engineering a paste, which will easily flow through the aperture (Fig. 2), is critical in order to achieve consistent printing, which will ultimately reduce defects and increase production yield.

MATERIALS AND METHODS

Apparatus

A controlled stress rheometer (Model: Physica MCR 301) with a parallel plate geometry with a diameter of 25 mm and gap of 1.0 mm was used as a measuring device. Prior to loading a sample onto the rheometer, the solder pastes were hand mixed with a plastic spatula for about 1 to 2 min. A sample was loaded on the bottom plate and the top plate was then lowered to the desired gap height of 1.0 mm by squeezing the extra paste out from between the plates. The excess paste at the plate edges was neatly trimmed with a plastic spatula. Then the sample was allowed to rest for about 1 min before starting the test. Identical loading procedures were followed in all the tests. All tests were conducted at 25^{0}C with the temperature being controlled by a Peltier-Plate system.

Material and sample preparations

The solder pastes used for this investigation are shown in Table 1. The variable parameters included the flux medium, particle size and distribution and metal load content. Samples P1, P2 and P3 were stored in the fridge at 4^{0}C, while the room temperature (which could not be controlled) was monitored to average 24^{0}C and 35% humidity. Before each rheological measurement the samples were taken out and left about 8 hours to reach room temperature.

The flux performs three main functions during the soldering process. Firstly, the flux must provide a solderable surface by removing the organic and/ or oxide layers from the surfaces to be soldered. Secondly, the flux also serves to protect the cleaned surface by preventing re-oxidation of the surface at high temperatures (and this function is particularly important for lead-free soldering applications as the soldering temperatures are much higher than those used for Sn/Pb alloys). Finally, the flux also helps to facilitate heat transfer between the molten solder and the base metal on the substrate, enhancing the

wetting of molten solder onto the base. In addition to cleaning the surface, the flux must also remove any oxide on the solder alloys. Different types of rosin/resin materials are used for solder paste formulations to suit different applications. The rosin/resin material is dissolved in a suitable solvent; and activators may be added to enhance the fluxing activity of the flux. The fluxing strength depends on its molecular structure of the chemical, its physical properties and the surrounding medium.

Solder pastes used in these studies can also be classified on the basis of the flux activity and the nature of residues left after reflow soldering for example:

(a) Rosin Active (RA) and Rosin Mildly Active (RMA) flux – the main difference between these two variants is the concentration of activators. Residues from the soldering process can be removed by using a suitable solvent such as alcohol.

(b) No clean (NC) fluxes: In this case, the flux residues are benign (i.e. non-hygroscopic, non-conductive and non-corrosive) and hence there is no need for cleaning of the flux residues.

Experimental test method

Hysteresis loop test

The thixotropic behaviour can be studied through the hysteresis loop test, also known as the thixotropic loop. In the hysteresis loop test, the shear rate is ramped up to a maximum shear rate, γ_m and then reversed back to the first (original) shear rate. In this study, the shear rates were increased from $0.01s^{-1}$ to $50s^{-1}$ (step-up) and the second curve was a result of decreasing shear rate $50s^{-1}$ to $0.01s^{-1}$ (step-down).

Constant shear rate test

The constant shear rate test is used to investigate the paste sample's dependency on time. For a given constant shear rate, the viscosity of the paste sample decreases over time, ultimately reaching a steady value. In this study the sample is subjected to six different shear rates; 0.01 s^{-1}, 0.1 s^{-1}, 1 s^{-1}, 10 s^{-1} and 50 s^{-1} and each of the tests was carried out for a period of 180 seconds (Table 2). When the samples were sheared longer than 180 seconds, it was observed that the pastes were slowly creeping out of the parallel plates causing a massive drop in the viscosity.

RESULTS AND DISCUSSION

Hysteresis loop

As expected, the viscosity of the pastes drops with increasing shear rate, which indicates shear thinning behaviour of the pastes. The pastes exhibit thixotropic behaviour as the presence of a hysteresis area between the step-up curve (0.01 to 50 s^{-1}) and step-down curve (50 to 0.01 s^{-1}). The region between the up curve and down curve in hysteresis curve is an indication of the thixotropic behaviour of the pastes. Based on the area between the two curves, sample P1 showed the largest structural breakdown followed by sample P3 and P2 (Fig. 3). Samples P2 and P3 seemed to show good recovery after gradual drop in the shear rates. In addition, the recovery (%) between the step-up (breakdown) and step-down (build-up) was measured using the equation Recovery (%) = {[viscosity (step-up) – structural recover] / [viscosity (step-down) – structural breakdown]} x100. The calculated recovery was 4.6%, 70.3% and 38.9% for samples P1, P2 and P3 respectively (Table 3). From the results, it is clear that sample P2 showed a good recovery compared to P1 and P3. As a concentrated suspension, the rheology

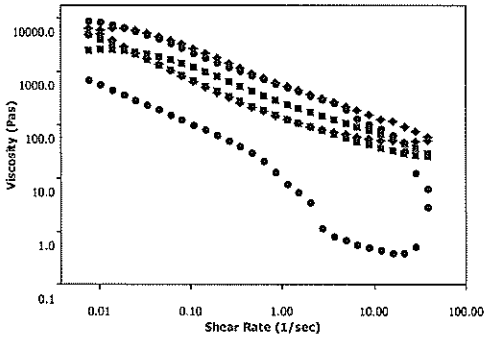

Figure 3. Thixotropic flow curve of sample P1 (•); P2 (■); P3 (♦).

Table 2. Constant shear rate test parameters.

Shear rate (s^{-1})	Shearing Time (sec)
0.01	180
0.1	180
1	180
10	180
50	180

Table 3. Recovery of samples P1, P2 and P3.

Sample	Recovery (%)
P1	4.6
P2	70.3
P3	38.9

of solder pastes is dominated both by the flux-vehicle system and the solid content, the solid volume fraction and the particle size distribution of the solder powders [16]. In this study, all the above mentioned parameters were constant except flux-vehicle system. Based on the results, the good recovery shown by sample P2 could be attributed to the strong interaction between the flux-vehicle system and the particle which gives the paste highly elastic behaviour as opposed to the P1 and P3.

The sample P2 consists of RA flux, solvent, activators and thickeners. The RA flux-vehicle system usually has a higher activator content compared to P1 and P2 samples to enhance the wetting behaviour of the solder pastes. However the major contributing factor to the high elasticity of sample P2 could be due to the solvent itself. Solvents are generally non-volatile and are used to dissolve the flux and other active constituents in the solder paste. The selection of the solvent blend must take into account several conflicting properties – for example, the solder paste must be able to flow well for good printing performance, and it must also have good tackiness for component placement performance, yet it must not be too tacky to prevent the squeegee from separating easily from the stencil after the print stroke. Again, the solvent should have a low evaporation rate to ensure that it does not dry out quickly, particularly during the stencil printing; and once deposited, the solvent must not cause cold slump or bleeding of the paste deposit on the PCB. A good recovery after the removal of shear rate or stress can help to maintain the structure of the pastes deposits on the printed circuit board.

Constant shear

In the step-down experiment (0.01 s^{-1} and 0.1 s^{-1}), the viscosity of the paste gradually increased with time (Fig. 4a,b). When the sample was sheared at 0.01 s^{-1}, the viscosity rose steeply in the first 50 sec; after this period, the paste viscosity continued to increase. The sharp rise in viscosity could be due to the paste resisting flow due to the presence of strong flocculation within the suspension. The strong flocculation is common in concentrated suspensions due to closely packed structure [17]. As the shear rate is increased in one order of a magnitude, the viscosity reaches a steady state after the period of 20 sec. With an increase in the shear rate, some of the paste structure is gradually broken. It is interesting to note that at both shear rates, sample P1 recorded the highest viscosity followed by sample P3 and P2. The sample P1 showed the lowest recovery compared to the other two samples. This could indicate that the RMA flux-vehicle system used in the formulation of paste P1 could be causing the paste to be 'tacky'.

In constant shear rate test, the paste viscosity is expected to reach a steady state value as measured for 0.1 s^{-1}. However, the viscosity curve did not follow this trend when the shear rate was increased to 1 s^{-1} (Fig. 4c). Sample P1 showed the most drop viscosity as opposed to samples P2 and P3. The drop in viscosity could indicate that the sample P1 has the least stable structure compared to samples P2 and P3. In order to strengthen this argument, the solder pastes were subjected to a higher shear rate of 10 s^{-1} and 50 s^{-1} (Fig. 4d,e). It is interesting to note that the samples P1 and P3 showed a drastic drop in viscosity whilst there was no significant change in the viscosity of sample P2, which seems to show a good resistance to structural breakdown. The sample P2 with the RA flux-vehicle system, which consists of rosin, solvent, and aggressive activators could provide a strong resistance to structural breakdown compared to the RMA and NC flux-vehicle systems. The build-up of structure at low shear rates could be attributed to the kinetic process, which is dependent on the effectiveness of the colliding particles to form a bind between them, as opposed to high shear rates. The results obtained support this idea for all three samples.

Equations (4) and (5) were used to determine the structure parameter values for breakdown (λ_u) and build-up (λ_d) of the solder paste samples. The structural parameter value in the step-down experiment (λ_d) was higher for the shear rate of 0.1 s^{-1} compared to 0.01 s^{-1} (Fig. 5a). The results seem to suggest that at lower shear rates, the paste was resilient to structural breakdown. Therefore in a step-down (build-up) experiment, lower structural parameter, λ_d, will indicate a structured paste material. From the constant shear rate test, sample P1 recorded the highest viscosity and a highest structural parameter value. Therefore, we can assume that sample is more structured as the viscosity is higher but more study is needed to prove this assumption.

In the step-up (breakdown) experiment, the structural parameter values were close to zero, which indicates structural breakdown in the paste material. As expected, samples P1 and P3 showed the greatest structural breakdown with increasing shear. However,

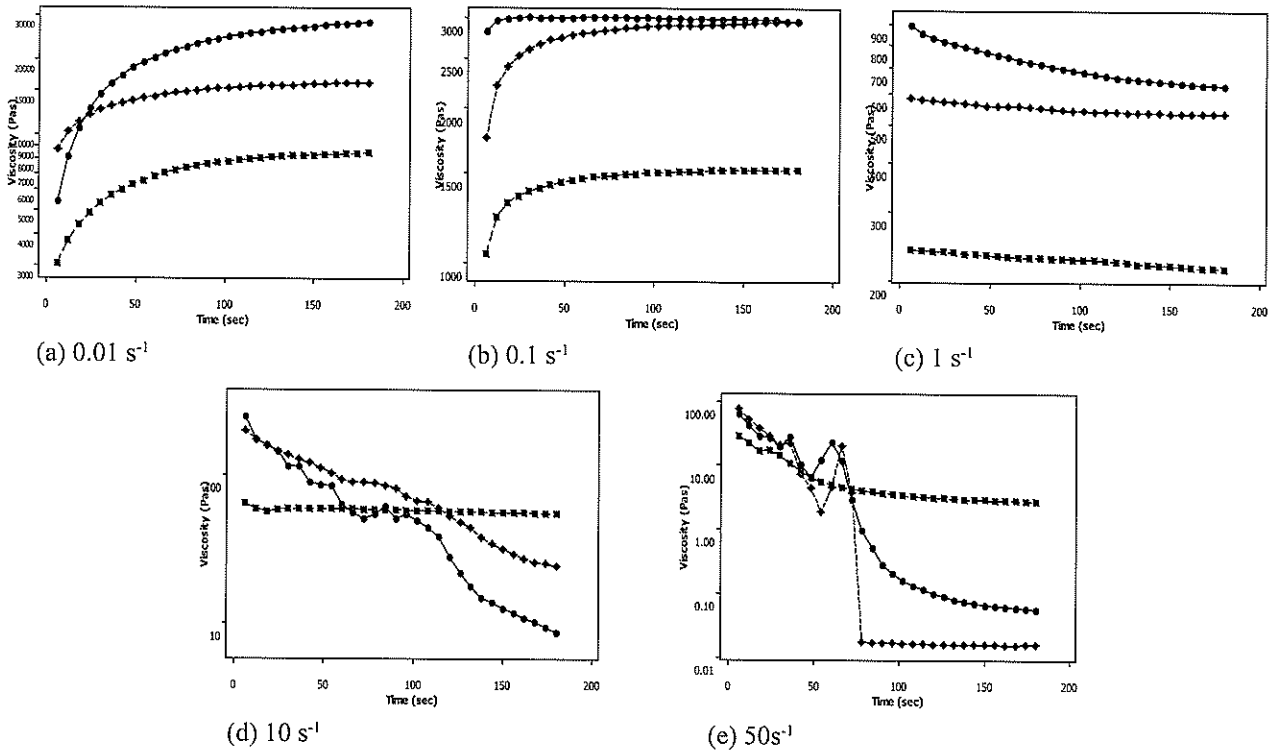

Figure 4. Constant shear flow curve: (a) 0.01 s^{-1}; (b) 0.1 s^{-1}; (c) 1 s^{-1}; (d) 10 s^{-1}; (e) 50 s^{-1} for samples P1 (●); P2 (■); P3 (♦).

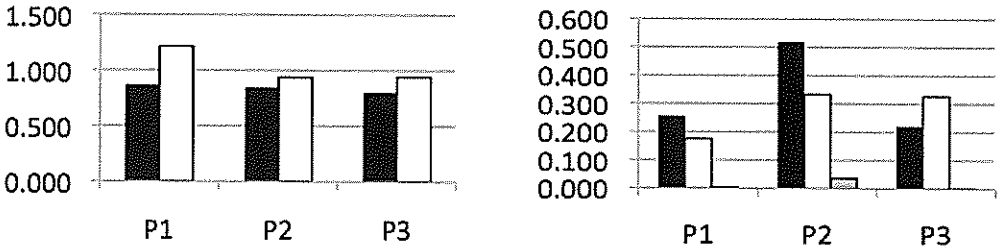

Figure 5. Structural parameter values for (top) step-down (build-up), λ_d, and (bottom) step-up (breakdown), λ_u of samples P1, P2 and P3 for applied shear rates. Top: 0.01 s^{-1} (■), 0.1 s^{-1} ( ) ; Bottom: 1 s^{-1} (■), 10 s^{-1} ( ) and 50 s^{-1} (▨).

it is interesting to note that sample P2 had the largest structure parameter value, which typically can be interpreted as a strong structure despite P2 having a lower viscosity when compared to P1. Hence, the earlier assumption that higher viscosity could yield a structured parameter is no longer valid in the case of solder pastes. One of the contributions of this study also showed that the structural parameter value could be used to predict the stability of the sample at high shear rates. This is important because of the various shear rates the pastes experience during the stencil printing process.

Conclusion

The thixotropic behaviour of the three solder pastes samples with different flux-vehicle system was investigated in this study. The samples were subjected to hysteresis loop test and constant shear test in order to quantify the extent of structural breakdown and build-up in the solder paste samples. In the hysteresis test, the area between the flow curve of the increasing shear rate and decreasing shear rate could be used as good indicator of the past recovery. The structural parameter value obtained from the structural kinetic model could be used as a parameter to study the paste breakdown and build-up. The study also found that

the structural parameter for step-up could be used to determine the stability of the solder paste suspensions. This information could be used by solder paste manufacturers to ascertain the paste behaviour during the stencil printing process and dispersion quality.

Acknowledgements – The authors wish to thank the UTAR Research Fund for financial support of this work.

REFERENCES

1. Ferguson, J. and Kemblowski, Z. (1991) *Applied Fluid Rheology*. Elsevier Applied Science, London.
2. Hwang J.S. (1989) *Solder paste in electronics packaging*. Van Nostrand Reinhold, New York.
3. Johnson C.C. and Kevera J. (1989) *Solder Paste Technology: Principles and Applications*. TAB Books Inc.
4. Currie M.A. (1997) *Characterisation of solder pastes used in the reflow soldering of surface mount assembly*. Ph.D. Thesis, University of Salford.
5. Barnes H.A. (1997) Thixotropy a review. *Journal Non-Newtonian Fluid Mechanic* **70**: 1-33.
6. Cheng D.H. and Evans F. (1965) Phenomenological characterization of the rheological behavior of inelastic reversible thixotropic and antithixotropic fluids. *British Journal of Applied Physics* **16**: 1599-1617.
7. Rosales F.J.G. and Hernandez F.J. R. (2006) Structural breakdown and build-up in bentonite dispersions. *Applied Clay Science* **33**: 109-115.
8. Ogata S., Kanazawa J. and Takei T. (1991) A study of the rheology and printability of solder paste. *OKI Technical Review* **56**: 5-10.
9. Lapasin R. (1994) Rheological characterisation of solder pastes. *Journal of Electronic Materials* **23**: 525-532.
10. Nguty T.A., Ekere N.N. and Adebayo A. (1999) Correlating solder paste composition with stencil printing performance. In: *IEEE/CPMT International Electronics Manufacturing Technology Symposium*, pp 304-309. Austin, Texas.
11. Durairaj R., Ekere N.N. and Salam B. (2004) Thixotropy flow behaviour of solder and conductive adhesives paste. *Journal of Material Science: Materials in Electronics* **15**: 677–683.
12. Durairaj R., Mallik S. and Ekere N.N. (2008) Solder paste characterisation: towards the development of quality control (QC) tool. *Journal of Soldering Surface Mount Technology* **10**: 33–40.
13. Durairaj R., Jackson G.J., Ekere N.N., Glinsk G. and Bailey C. (2002) Correlation of solder paste rheology with computational simulations of the stencil printing process. *Journal of Soldering Surface Mount Technology* **14**: 11–17.
14. Jackson G.J., Hendriksen M.W., Kay R.W., Desmulliez M., Durairaj R.K. and Ekere N.N. (2005) Sub process challenges in ultra fine pitch stencil printing of type-6 and type-7 Pb-free solder pastes for flip chip assembly applications. *Journal of Soldering and Surface Mount Technology* **17**: 24–32.
15. Nguty T.A. and Ekere N.N. (2000) The rheological properties of solder paste and solar pastes and the effect on stencil printing. *Rheologica Acta* **39**: 607-612.
16. Ekere N.N., He D. and Cai L. (2001) The influence of wall slip in the measurement of solder paste viscosity. *IEEE Transactions on Components and Packaging Technologies* **24**: 468-473.
17. Buscall R., McGowan J.I., Jones A.J.M. (1993) The rheology of concentrated dispersions of weakly attracting colloidal particles with and without wall-slip. *Journal of Rheology* **34**: 621-641.

Journal of Science and Technology in the Tropics (2009) **5**: 87-99

Vertebrate species diversity in the Broga and Sungai Lallang Forest Reserves, Hulu Langat, Selangor, Peninsular Malaysia

B. L. Lim[1], Dennis Yong[2], Mano Tharmalingam[2], Chai Koh Shin[3] and C. C. Lim[1]
[1]12 Jalan Koop Cuepacs 3E, Taman Cuepacs, 43200 Cheras, Selangor, Malaysia
(E-mail:limbooliat@yahoo.co.uk)
[2]Kingfisher Tours Sdn. Bhd. (E-mail: birds@tm.net.my)
[3]4 Jalan Indah 3, Taman Indah Sungei Jolok, 43000 Kajang, Selangor, Malaysia

Received 05-06-2009; accepted 22-06-2009

Abstract A vertebrate fauna (amphibians, reptiles, mammals, birds) survey was conducted during the periods 23-30 May and 7-16 September 2003 in the Broga Forest Reserve (BFR) and the adjoining Sungai Lallang Forest Reserve (SLFR) in the Hulu Langat District, Selangor, Peninsular Malaysia. A total of 264 species comprising 27 species of amphibians, 28 species of reptiles, 74 species of small mammals and 135 species of birds were recorded from these two forest areas. The overall species diversity in the BFR was 24.2% lower than that of the SLFR (i.e. 160 and 224 species, respectively). The difference between the two locations is discussed in relation to the environmental status of the forests.

Keywords species diversity – amphibians – reptiles – mammals – birds

INTRODUCTION

Little is known of the vertebrate fauna in BFR. In the 1950s, during the monkey export boom, BFR was one of the main trapping grounds for the export trade. In the process, occasional wildlife species, such as the common wild cat *Prionailurus bengalensis*, civet *Paradoxurus hermaphroditus*, linsang *Prionodon linsang* and a bamboo rat *Rhizomys sumatrensis* were captured by the Orang Asli there [1].

The results of our survey of the vertebrate fauna, though not extensive or intensive (as it covered only two weeks), are presented here to provide baseline information for the area.

STUDY AREAS

The Broga Forest Reserve (BFR) is located at N 02° 57', E 101° 54' 09" with its highest elevation at about 352 m asl, and its lowest at about 52 m asl. The site is bounded on two sides by Sungai Saringgit that flows in a westerly direction along the southern boundary and Sungai Tekali which flows in a southwest direction along the north western boundary. Adjoining the BFR on the east is the Sg. Lallang Forest Reserve (N 02° 57' 32", E 101° 54' 02") comprising undulating forested hills with elevations ranging from 200 m to 500 m asl. Both the study sites were logged-over forests.

Broga Forest Reserve is a highly disturbed forest type covered with thick undergrowth and lower tree species forming a rich under-canopy layer. The vegetation here is mostly scrub (dry bushes and small trees) and some secondary regeneration forest (tall trees with lush ground vegetation of palms, bananas and gingers etc.) It has also been severely disturbed by illegal cultivation of fruit trees (such as durian, star fruit and rambutan). There are many small and large streams, some with crystal clear water. Human traffic is rather heavy, comprising mainly farmers tending their orchards.

In the more hilly parts of Sg. Lallang Forest Reserve, the habitat type is also heavily disturbed with thick undergrowth, giving a similar structure of a regenerating forest type. The habitat is always dry compared to the seemingly moist riparian condition of the Broga Forest Reserve. There are some small streams and rivers that are crystal clear, but these are hard to come by within the forest areas. Patches of the area are sparsely planted with durian and banana by the Orang Asli communities, and there

Journal of Science and Technology in the Tropics (2009) **5**: 133-139

3D medial axis approximation through Delaunay triangulation

Lee Kok Yong
Faculty of Engineering and Science, Universiti Tunku Abdul Rahman, Setapak,
53300 Kuala Lumpur, Malaysia
(Email: lkyong@utar.edu.my)

Received 14-11-2009; accepted 17-11-2009

Abstract The medial axis or skeleton representation of a 3D solid has many applications in engineering. However its full potential in applications such as mesh generation, feature recognition, robot path has been hindered by the lack of robust and general medial axis algorithm. A discrete approach of computing the medial axis is presented. This algorithm exploits the Delaunay triangulation empty sphere property. Along with this algorithm, the medial axis and its associated topological entities are defined. This algorithm adopted an adaptive approach toward medial axis computing, in that the boundary point set of the Delaunay triangulation is refined where necessary to guarantee a correct topological representation of the medial axis.

Keywords medial surface – medial axis – skeleton – idealisation – dimensional reduction

INTRODUCTION

The medial axis, known as skeleton in other publications [1], has many unique characteristics that attracted the attentions of many researchers throughout the world. There are literally hundreds of articles written on various aspects of the medial axis transform (MAT), since its first introduction by Blum [4]. It has shown its potential in many engineering applications, such as finite element meshing [6]; font design [9]; and tool path generation [10]. The uniqueness of the medial surface also prompted a possible complimentary representation [11] alongside Boundary Representation and Constructive Solid Geometry, in CAD.

Given the vast research on MATs on various aspects, there is no single definition for the medial surface. A survey of different kinds of algorithm for the construction of the medial axis can be found in [3]. With that in mind, we define the medial axis as follow:

> The medial axis a 3D object is described by the closure of the locus of the centres of all maximal inscribed spheres (Fig. 1). A sphere is maximal if it is contained within the object but not within any other sphere within the object.

The medial axis has applications in idealisation for the Finite Element Analysis (FEA). FEA often requires the object to be abstracted in the context of its structural behaviour. The geometric model is transformed into an abstracted model through the removal of details and structural idealisation for better and faster analysis as well as to increase the efficiency of mesh generation.

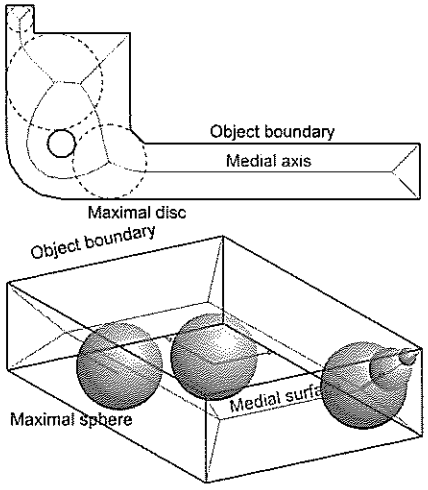

Figure 1. Medial axis and maximal sphere.

This is where the medial axis abstraction steps in to alleviate the many limitations by providing a complementary representation which captures the geometric proximity of the boundary elements in

Journal of Science and Technology in the Tropics (2009) 5: 133-139

a simple form. It provides a unique description of shape that is of lower dimension than the original object[13].

Unlike the exact computation algorithm proposed in [15], which is computationally intensive and limited to only polyhedron, this work proposed an approximation algorithm in deriving medial axis.

DELAUNAY TRIANGULATION

A fundamental property of the Delaunay triangulation of a set of distinct points is the empty circumsphere property. The circumsphere associated with each Delaunay tetrahedron does not contain any other point in its interior. This property will form the basis of the dicretization algorithm presented in this paper.

Consider a set of points S, created on the boundary of an object, **W**. As h tends to 0, where h is the length of the longest edge of the discretization of the boundary of **W**, the circumsphere associated with each tetrahedron in the triangulation tends to a maximal circle within the object. In other words, the medial axis is obtained by joining the circumcentre of the tetrahedra in the triangulation [16]. This description can be more easily visualized by examining the 2D counterpart (Fig. 2). As the Delaunay edge on the object boundary of the triangles shrinking from right to left the circumcircle also tend to become a maximal disc in the object.

There are several algorithms for constructing the Delaunay triangulation of a point set in $\mathbf{R}^3$ and it can be considered a solved problem. The triangulation algorithm implemented in this paper for the construction of Delaunay triangulation is the randomised incremental flip algorithm by Mücke [18].

ASSOCIATING TETRAHEDRA TO TOPOLOGICAL ELEMENTS OF MEDIAL AXIS

All the tetrahedra within the triangulation can be uniquely identifiable with a particular element of the medial axis topology. The distinction between the topological elements of the medial axis is dependent on the manner in which the inscribed sphere interacts with the object boundary. Therefore, some definitions relevant to the boundary maximal sphere interaction are defined below.

Definition 1 A **site** is a distinct point, finite line interval or finite area at which a maximal sphere touches the object boundary tangentially.

Definition 2 The **order** of a sphere is the number of sites at which the sphere touches the boundary.

The domain of the solids being considered in this work will only permit distinct point tangencies between the sphere and the solid boundary. This imposes restriction on the maximum curvature of the solid boundary.

A maximal sphere is quasi-tangent at a site if a boundary element in the site is contained in the closure of one or more other elements and the sphere is tangential to the geometries of all elements concerned. Thus, the condition of tangency is relaxed so that, for example, a sphere which is tangential to the geometry of a face (or edge) at its bounding edge (or vertex) is considered to be tangential to both elements. Hence, the sphere is quasi-tangential to *e1* and *f3* (Fig. 3).

A sphere in space is specified by four parameters, the three coordinates of its centre and its radius. Hence, from four distinct tangent points four equations can be formulated from which these parameters may be determined. This is sufficient provided the four equations are linearly independent, i.e. the tangent points are non-coplanar. Three distinct tangent points

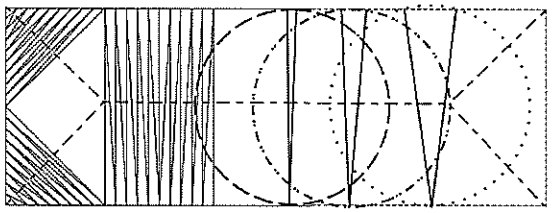

Figure 2. The circumcircle of a Delaunay triangle approximates an inscribed circle.

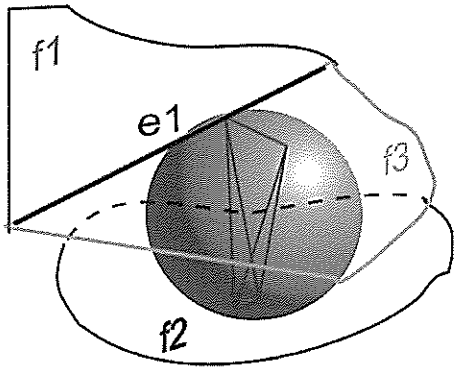

Figure 3. Inscribed sphere is quasi-tangential to e1 and f3.

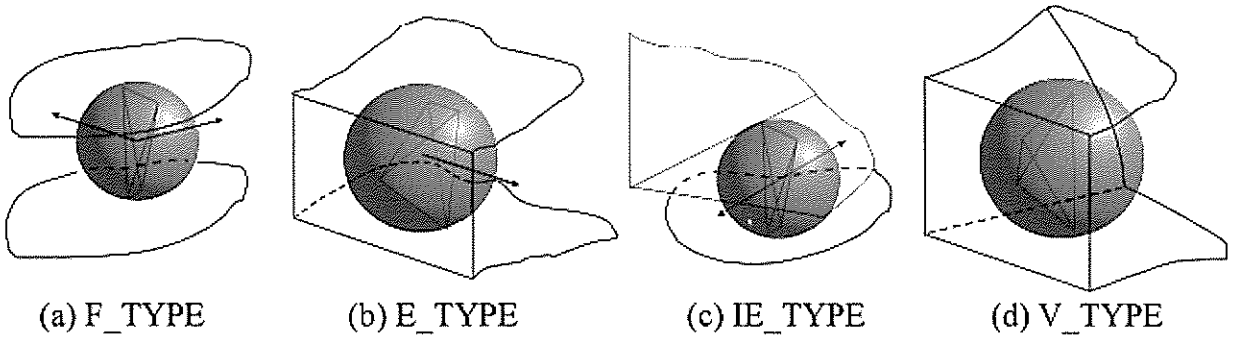

Figure 4. Tetrahedra classification.

introduces a one-dimensional freedom to the solution space. Two distinct tangent points will introduce a two-dimensional freedom in the solution space. In a similar manner, a point on the medial surface is classified according to the order and the degree of translative freedom of its associated sphere.

F_TYPE: tetrahedron associated with the face of the medial surface, the equivalent topological sphere is second order, no touching site is quasi-tangential. Hence the tetrahedron interacts with the object boundary at two disjoint boundary elements, which do not bridge topologically adjacent elements (Fig. 4a).

E_TYPE: tetrahedron associated with a normal medial edge. The equivalent topological sphere is of third order and no touching site is quasi-tangential. The tetrahedron interacts with the object boundary at three disjoint boundary elements (Fig. 4b).

IE_TYPE: tetrahedron associated with an intermediate medial edge. The equivalent topological sphere is of third order and is quasi-tangent at one or more touching sites. The tetrahedron interacts with the object boundary at two disjoint boundary elements, one of which bridges topologically adjacent elements (Fig. 4c).

V_TYPE: tetrahedron associated with a normal medial surface vertex. The equivalent topological sphere is of fourth order and is quasi-tangent free (Fig. 4d).

Equation formulation

Computing the exact position of the medial vertex can be formulated as a system of equations based on the conditions which a maximal sphere should satisfy at the points of contact: equidistant, tangency, perpendicularity etc. At any given site the sphere may touch an individual face, edge or vertex tangentially or it may touch a group of these elements quasi-tangentially. In this section six fundamental tangency cases are identified to which all the more complex cases are reducible using simple rules.

For each medial surface vertex, the following unknowns will be solved: the coordinates of its circumcentres, x_c, y_c, z_c, the sphere radius r, and the position of the exact tangent points in parameter space (u,v) on a surface and t on a curve.

It is assumed that the surface on which each face lies is represented by a continuous, single valued, bi-parametric mapping with continuous second order derivatives, and is expressed in the form: $x=x(u,v)$, $y=y(u,v)$, $z=z(u,v)$. $\mathbf{P}(u,v)$ is a vector to a point on the surface and $\mathbf{n}(u,v)$ the inward pointing unit normal at that point.

The curve associated with each edge is represented by a continuous, single valued, single-parametric mapping with continuous second order derivatives and is expressed in the form: $x=x(t)$, $y=y(t)$, $z=z(t)$. $\mathbf{P}(t)$ is a vector to a point on the surface and $\mathbf{t}(t)$ the unit tangent at that point.

In the following analysis $\mathbf{p}_c$ is a vector to the position of the centre of the sphere.

Case (a). Tangency to a surface

There are two unknowns, the parameter u and v at the point of tangency (Fig. 5). The sphere must satisfy the following vector equation.

$$\mathbf{p}(u,v)+r\mathbf{n}(u,v)-\mathbf{p}_c=0 \qquad (1)$$

Case (b). Tangency to a curve

There is one unknown variable in this case, the parameter t at the exact tangent point, (Fig. 6). The sphere must satisfy the following vector equation.

$$(\mathbf{p}_c-\mathbf{p}(t))\cdot(\mathbf{p}_c-\mathbf{p}(t))=r^2 \qquad (2)$$

$$(\mathbf{p}_c-\mathbf{p}(t))\cdot\mathbf{t}(t)=0 \qquad (3)$$

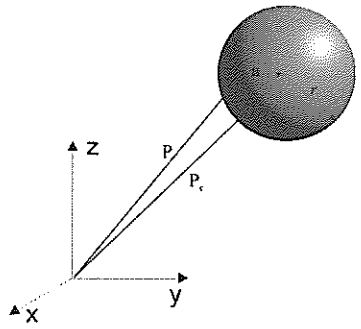

Figure 5. Tangency to a surface.

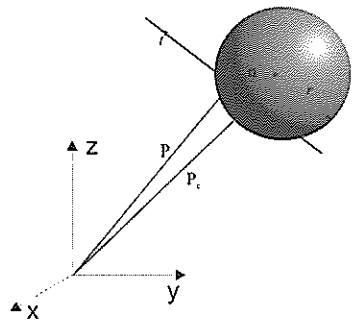

Figure 6. Tangency to a curve.

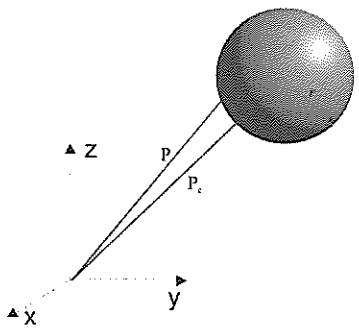

Figure 7. Contact at a point.

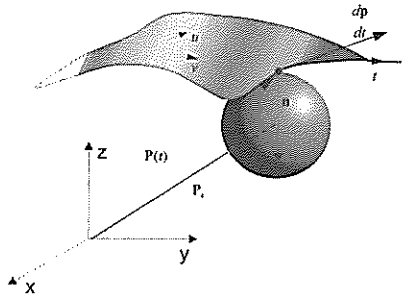

Figure 8. Tangential to a surface at an object edge.

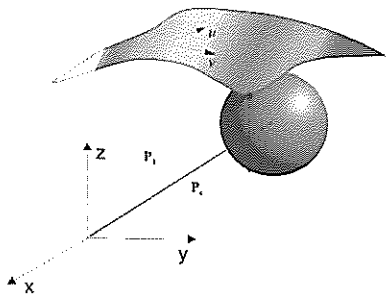

Figure 9. Tangential to a surface at an object vertex.

Case (c). Contact at a vertex

The position of the vertex is fully fixed and does not vary (Fig. 7), if $\mathbf{p}_1$ is the vector to the position of the vertex then the sphere must satisfy the scalar equation.

$$(\mathbf{p}_c - \mathbf{p}_1)\cdot(\mathbf{p}_c - \mathbf{p}_1) = r^2 \qquad (4)$$

In the following cases of quasi-tangency the lower order boundary element inherits the tangency constraints of the higher boundary element. Therefore the surface edge quasi-tangency equation will resemble the tangency to the face equation, and the curve-vertex quasi-tangency equation will resemble the tangency to the edge equation and etc.

Case (d) Sphere tangential to a surface at an object edge

The sphere must satisfy the equation

$$\mathbf{p}(t) + r\mathbf{n}(t) - \mathbf{p}_c = 0 \qquad (5)$$

where $\mathbf{p}(t)$ is a vector to a point on the curve and $\mathbf{n}(t)$ is the unit normal to the surface at a parametric point t on the curve (Fig. 8). This equation forces the sphere to be tangential to the surface at a point on the curve.

Case (e) Sphere tangential to a surface at an object vertex

The position of the vertex (Fig. 9) is fully fixed and does not vary, $\mathbf{p}_1$ is a vector to the position of the vertex and $\mathbf{n}_1$ is the normal to the surface at the position of the vertex.

$$\mathbf{p}_1 + r\mathbf{n}_1 - \mathbf{p}_c = 0 \qquad (6)$$

This equation enforces a tangency to the surface constraint at the vertex.

Case (f) Sphere tangential to a curve at an object vertex

The position of the vertex is fully fixed and does not vary, $\mathbf{p}_1$ is a vector to the position of the vertex and $\mathbf{t}_1$ is the unit tangent to the curve at the position of the vertex

$$(\mathbf{p}_c - \mathbf{p}_1)\cdot(\mathbf{p}_c - \mathbf{p}_1) = r^2 \qquad (7)$$

$$(\mathbf{p}_c - \mathbf{p}_1)\cdot\mathbf{t}_1 = 0 \qquad (8)$$

The appropriate set of equations is assembled for the tetrahedron in question based on the boundary entity which it touches and the nature of the tangency at each touching site.

Adaptive refinement

The main limitation of using Delaunay triangulation to approximate the medial axis is it is impossible to pre-determine the boundary point set required in order to generate an accurate medial axis. As the feature list grows and the object geometry gets complicated, the approximation fails to capture fine details. It is simply because the triangulation generated is too sparse to capture local features. The typical result of this low resolution is illustrated in Figure 10 where a small medial face is lost due to poor resolution.

Ambiguity within the medial axis in these situations can be overcome by enforcing a higher resolution at a global level. However, it is more desirable to identify segments of the medial edges where ambiguity may be presented and refine the resolution in that particular area. The critical segments of the medial edges can be filtered out during the tracing process. Consider medial edge *me1*, it is governed by faces f_1, f_2 and f_3. For any tetrahedra around the shaded region in Figure 10a which also corresponds to the medial edge *me1*, the inscribed sphere of these tetrahedra will not be able to converge to a maximal sphere within the object (Fig. 10c). Clearly it will result in incorrect medial surface topology (Fig. 10b).

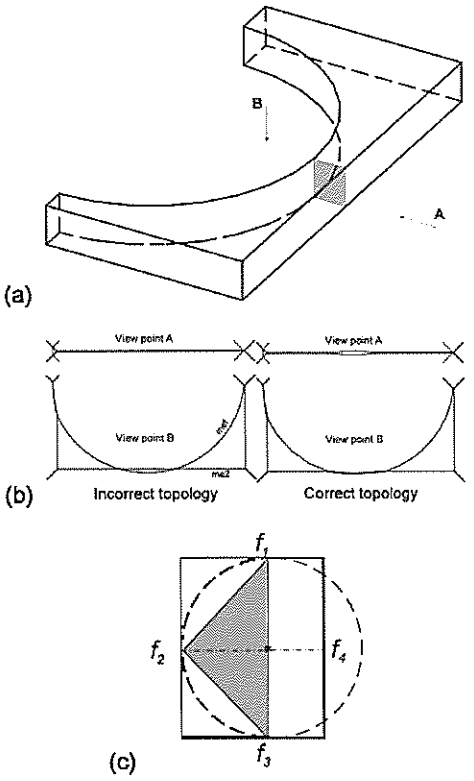

Figure 10. Ambiguity in medial axis due to poor resolution.

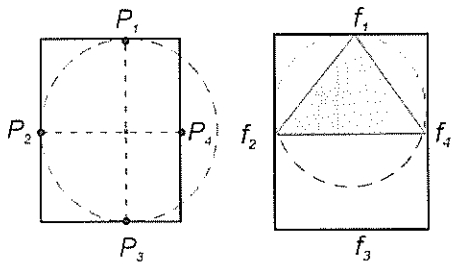

Figure 11. Points insertion and corrected inscribed sphere

Therefore, instead of computing the medial axis from the sparse triangulation directly, this work presents new algorithm where a tentative tracing will be carried out to eliminate any possible ambiguities regions. These ambiguities regions caused by the poor triangulation can be easily identified by performing a Boolean operation between the maximal sphere and the object itself. Subsequently inserting the exact tangent points of the maximal sphere into the triangulation, these tangent points will include the points on the three governor boundaries as well as the fourth boundary entity which is within the sphere radius. As for the case in Figure 11, the fourth boundary entity is the f_4.

Examples shown in Figure 12 are some results of the previous explained algorithm. (12a) is basically a block with a tapered cylinder cut out in the middle plus a torus cutout on the top surface of the block. (12b) is just half section of a hook. (12c) is again a block with half torus cutout in the first section of the block, followed by a sphere cutout in the middle of the block, then one slanted cylinder cutout near the bottom of the block. (12d) shows a simplified version of the piston crown.

SUMMARY AND CONCLUSIONS

This paper presents an algorithm which exploits the properties of the Delaunay triangulation while avoiding the need for a dense triangulation. With the tetrahedra classification scheme, a natural and intuitive association between tetrahedra and medial surface topologies is established. Then topology of the medial surface is assembled by tracing along the medial edges. During tracing, computation of the exact point on the medial surface is carried out on the fly for every tetrahedron. Should the object become complicated and a finer triangulation required, an adaptive triangulation refinement also introduces for

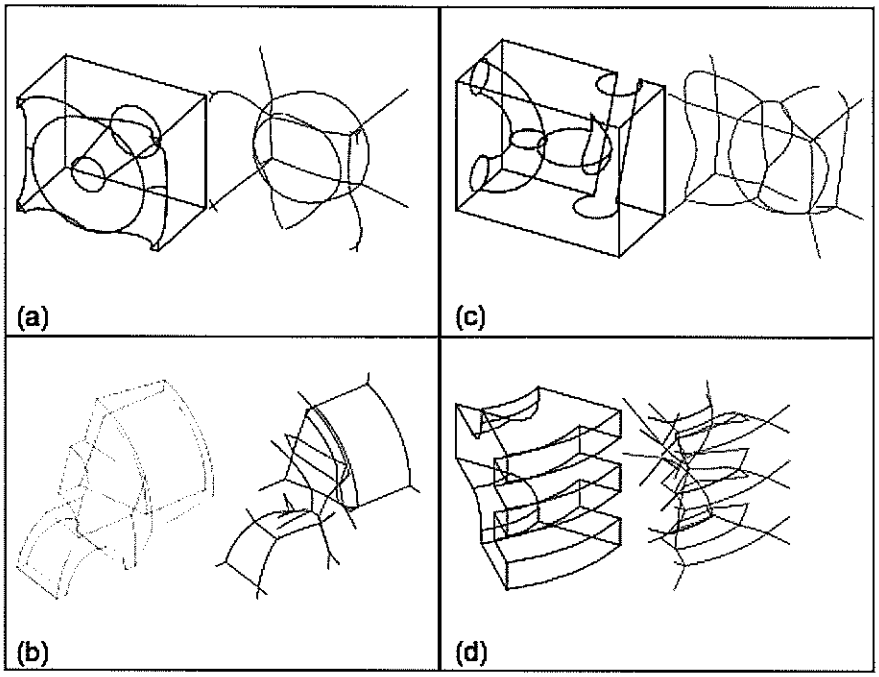

Figure 12. Medial axis examples.

the success of medial surface computations so that fine details can be captured.

The algorithm has been implemented for B-rep model (ACIS). Therefore it is possible to port the algorithm to other representation schemes, provided the interface is implemented. There are still many problems concerning the quality of the facetted medial surface. Although this issue again could be resolved if a denser triangulation was used, the final objective is to assemble the medial surface topology with the tracing algorithm from sparse triangulation, then the geometry will be computed in an adaptive way [19].

REFERENCES

1. Sherbrooke E.C, Patrikalkis N.M. and Brisson E. (1995) Computation of the medial axis transform of 3D polyhedral. *Proc. 3rd ACM Symposium on Solid Modeling and Applications*: 187-199.
2. Sherbrooke E.C., Patrikalkis N.M. and Wolter F. (1996) Differential and topological properties of medial axis transform. *Graphical Models and Image Processing* **58**(6):74-592.
3. Turkiyyah G.M., Storti D.W., Ganter M., Chen H. And Vimawala M. (1997) An accelerated triangulation method for computing the skeletons of free-form solid models *Computer-Aided Design* **29**(1): 5-19.
4. Blum H. (1967) A transformation for extracting new description of shape. In Wathen-Dunn W. (ed.) *Models for the perception of speech and visual form, MIT* 362-380.
5. Blum H. (1973) Biological shape and visual science. *Journal of Theoretical Biology* 38: 205-287.
6. Price M.A. and Armstrong C.G. (1997) Hexahedral mesh generation by medial surface subdivision: Part I. Solid with convex edges. *International Journal for Numerical Methods in Engineering* **40**: 111-136.
7. Gursoy H.N. and Patrikslakis N.M. (1992) An automatic coarse and fine surface mesh generation scheme based on the medial axis transform I: Algorithm. *Engineering with Computers* **8**(3): 121-137.
8. Tam T.K.H. and Armstrong C.G. (1991) 2D finite element mesh generation by medial axis subdivision. *Advances in Engineering Software* **13**: 313-324.
9. Choi H.I., Choi S.W., Moon H.P. and Wee N.S. (1997) New algorithm for medial axis transform of plane domain. *Graphical Models Image Process* **59**: 463-483.
10. Held M. (1991) On the Computational Geometry of Pocket Machining *Lecture Notes in Computer Science*, Springer-Verlag.
11. Wolter F.E. (1992) Cut locus and medial axis in

global shape interrogation and representation. Published in *MIT Design Laboratory Memorandum and MIT Sea Grant Report*.

12. Lee Y.G. and Lee K. (1997) Computing the medial surface of a 3-D boundary representation model. *Advances in Engineering Software* **28**: 593-605.
13. Bridget S.J. (1997) *Detail Suppression of stress analysis models*. PhD thesis, Queen's University of Belfast.
14. Donaghy R.J. (1998) *Dimensional reduction of stress analysis models*. PhD thesis, Queen's University of Belfast.
15. Culver T., Keyser J. and Manocha D. (2004) Exact computation of the medial axis of a polyhedron. *Computer Aided Geometric Design* **21**(1): 65-98.
16. Yu X., Goldak J.A. and Dong L. (1991) Constructing 3D discrete medial axis. *ACM Symposium Solid Modelling foundations and CAD/CAM Applications* pp. 481-485.
17. Dey T.K. and Zhao W. (2003) Approximating the medial axis from the Voronoi diagram with a convergence guarantee. *Algorithmica* **38**(1): 179-200.
18. Mücke E.P. (1993) *Shapes and implementations in three-dimensional geometry*. PhD thesis, Report UIUCDCSR-93-1836,DeptofComp.Sci.,University of Illinois, Urbana-Champaign.
19. Ang P.Y. and Armstrong C.G. (2001) Adaptive curvature-sensitive meshing for medial axis. *10th International Meshing Roundtable* pp. 155-166.

Journal of Science and Technology in the Tropics (2009) **5**: 141-150

Study of chaotic dynamics and hysteresis in ferromagnetic film via discrete model

Pek-Lan Toh and Siew-Choo Lim*
School of Physics, Universiti Sains Malaysia, 11800 USM, Pulau Pinang, Malaysia
(*Email: limsiewchoo1@yahoo.com)

Received 26-03-2009; accepted 30-10-2009

Abstract In this paper, the ferromagnetic Landau free energy expansion is rewritten in discrete form along the film thickness. Calculus of variation is then applied on the discretized free energy expansion. In equilibrium, the initial magnetization profile of the ferromagnetic film is calculated by imposing boundary conditions. With applied time dependence magnetic field, the dynamics in the ferromagnetic film are obtained by combining the variations of discretized Landau free energy expansion and Landau Lifshitz (LL) equation of motion. The resulting coupled first order nonlinear differential equations are solved numerically and presented graphically by using different surface parameters, thicknesses of the film, and various amplitudes and frequencies of the applied field.

Keywords discrete model – chaos – hysteresis – ferromagnetic film – magnetization profile – Landau free energy expansion

INTRODUCTION

In recent years, the use of ferromagnetic film has become widespread in engineering application. These applications include magnetic recording process, cores for electromagnets, transformers, etc [1]. Phase transition in ferromagnetic system has been studied extensively both theoretically and experimentally [2-5]. In 2001, Jang and Grimson [6] have reported the dynamics phase transition of ferromagnetic thin film by using Monte Carlo simulation. Liu and Garcia-Cervera [7] have studied the effects of incorporating thermal noise into LL equation of motion for the ferromagnetic thin films. They have reported the relation between the thermal noise and switching fields in the hysteresis loop. In experimental observations, Yan *et al.* [8] have reported the magnetization reversal of magnetic thin film by using a free boundary domain wall pinning model. Besides this, Nozaki and Matsuyama [9] studied the magnetization reversal in a single-domain magnetic particle. From the literature survey, it is obvious that most of the theoretical studies on magnetic films are based on Landau free energy expansion via continuous model, or magnetic Hamiltonian via Monte-Carlo simulations. It is of interest to carry out an alternative approach for the study of dynamics in ferromagnetic film, i.e. Landau free energy expansion via discrete model [10], which is more realistic in numerical simulations, and this is the main theme of this paper. The calculations and results in this paper is an extension of the research in bulk forromagnet [11, 12].

FORMALISM

For ferromagnetic system in finite geometry, i.e. a ferromagnetic film, its Landau free energy per unit area expansion is rewritten in integral form:

$$f = f_0 + \int_{-L/2}^{+L/2}\left[\frac{1}{2}\alpha_2\mathbf{M}^2 + \frac{1}{4}\alpha_2\mathbf{M}^4 + \frac{A}{2}\left(\frac{d\mathbf{M}}{dx}\right)^2 - \mathbf{B}(t)\cdot\mathbf{M}\right]dx + \frac{A}{2\lambda}\left(\mathbf{M}_{-L/2}{}^2 + \mathbf{M}_{+L/2}{}^2\right) \quad (1)$$

with the boundary conditions:

$$\frac{d\mathbf{M}}{dx} \pm \frac{1}{\lambda}\mathbf{M} = 0, \qquad x = \pm\frac{L}{2} \quad (2)$$

f_0 is the free energy other than the contribution of order parameter in ferromagnetic phase, α_0, α_2 and α_4 are the Landau coefficients, A is a constant, $\mathbf{M}$ is the magnetization, λ is the extrapolation length [2,

is constant traffic of Orang Asli visiting the forest in search of rattan and bamboo as well as hunting animals for food.

METHODOLOGY

A herpetologist, a mammalogist, two ornithologists, a parasitologist, two para-professionals and three Orang Asli comprised the field team. Two field trips were carried out in the periods 23-30 May 2003 and 7-15 September 2003.

Amphibians and reptiles were searched and captured during daylight hours and at night following established techniques [2].

The mammal survey, particularly of small mammals was conducted by using 200 collapsible traps, 100 for each of the trapping sites. To capture bats, two harp traps and four mist nets were deployed. The baiting of traps, placements, time of collection and direct and indirect methods of observations, followed established techniques and procedures [2].

The bird survey was carried out by two ornithologists. They noted down the birds seen or heard when walking along the existing tracks and foot paths. The birds seen were identified using 10x42 Swarovski binoculars and a Kowa scope. Bird songs were identified based on knowledge accumulated over 20 years of field experience. In the event where bird calls were unknown or unfamiliar, a tape recorder with a directional mike was used to record the call and then played back to lure the bird for sight identification. The time spent in the field varied but in general, observation started at 0700 hr until 1300 hr when bird activities started to slow down, with a second round of observations beginning around 1500 hr and ending at sunset. Occasional night forays were made to look for nocturnal species like owls, frogmouths, nightjars etc. The identification, taxonomic order, status and common and scientific names are based on existing literature [3-6].

RESULTS AND DISCUSSION

A total of 264 species of vertebrates was recorded during the survey in BFR and SLFR. There were 27 species of amphibians, 28 species of reptiles, 74 species of mammals and 135 species of birds (Table 1).

Table 1. Number of vertebrate species in Broga Forest Researve and Sg. Lallang Forest Reserve.

Taxon	Broga FR	Sg. Lallang FR	Total	Percentage
Amphibians	22	18	27	10.2
Reptiles	19	19	28	10.6
Mammals				
Volant mammals	24	30	33	12.5
Non-volant mammals	23	36	41	15.5
Birds	72	121	135	51.2
Total no. of species	160	224	264	

The number of species found in BFR was 24.3% lower than that in the adjacent SLFR. The higher number of species in SLFR was due to the bird and mammal groups, especially the birds. In the case of amphibians and reptiles, there was no marked difference between the two sites. The lower species diversity in BFR can be attributed to the constant disturbance due to the ongoing activities of contractors opening tracks into the forest to access certain areas both for drilling works (water tests) and seismic testing as well as the daily visits by the farmers to their orchards. In contrast the adjacent SLFR was only visited by the Orang Asli hunting for animals for food and collecting forest products (bamboo, canes).

Amphibians

A total of 27 species of frogs and toads from five families were collected from the BFR and adjacent SLFR (Appendix 1). Among these, only five species, the Tweedie's stream frog *Limnonectes tweediei*, the Wallace flying frog *Rhacophorus nigropalmatus*, Tunku's tree frog *Rhacophorus tunkui*, the Smooth-skin wart frog *Theloderma licin* and the Rufous-sided sticky frog *Kalophrynus pleurostigma* were interesting findings in both study sites. These five species though common are not as abundant in forested areas [2, 7, 8]. The rest of the 22 species are common and abundant in forest and open habitats [9].

Reptiles

The 28 reptilian species (Appendix 1) comprised 13 species of lizards from four families (Agamidae, Scinicidae, Geckonidae and Varanidae), 13 species of snakes from three families (Pythonidae, Colubridae

3, 5, 13, 14], and $\mathbf{B}(t)$ is the applied time dependent field. The thickness of the film is L, and is along the x - direction. The dimensions of the film are assumed as infinities along the y - and z - directions. In this approach, we consider the system in its ferromagnetic phase can be represented solely by the Landau free energy per unit area expansion in terms of its order parameter, i.e. **M**, its material constants and temperature. This means we have neglecting the microscopic effects, i.e. anisotropy, domain wall movements in the presence of applied field, and all the quantum mechanical interactions that usually considered in the research of ferromagnetic system. In equation (1), the surface energy has been considered into Landau free energy expansion. Based on equation (1), and a schematic sketch of discretized ferromagnetic film (Fig. 1), the Landau free energy per unit area expansion of a ferromagnetic film is reconstructed into discrete form:

$$G = G_0 + \frac{b}{2}\sum_{n=-N+1}^{+N-1}\left(\alpha_2\mathbf{M}_n{}^2 + \frac{1}{2}\alpha_2\mathbf{M}_n{}^4\right) + \frac{bA}{2}\sum_{n=-N}^{+N-1}\left(\frac{d\mathbf{M}}{dx}\right) - b\sum_{n=-N}^{+N}\left[\mathbf{B}(t)\cdot\mathbf{M}_n\right] + \frac{A}{2\lambda}\left(\mathbf{M}_{-L/2}{}^2 + \mathbf{M}_{+L/2}{}^2\right) \quad (3)$$

where $|N|$ is the number of slices from the centre to the left and right of the film, $-N \le n \le +N$, n is position index along the thickness of the film from $-N$ to $+N$, $b = L/h$ is the thickness of a slice, with h is the total number of slices, and L is the thickness of the film. The magnetization, $\mathbf{M}_n$, in each slice is considered as a 3-dimesional vector with Cartesian components $\mathbf{M}_n = M_{n,x}\hat{i} + M_{n,y}\hat{j} + M_{n,z}\hat{k}$. The spatial dependence term, i.e. $d\mathbf{M}/dx$, is expanded by forward difference truncated at the first order. In equilibrium, the variation of free energy per unit area is minimum, i.e.

$$\frac{\delta G}{\delta M_{n,i}} = 0 \quad (4)$$

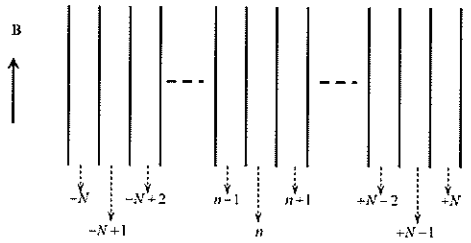

Figure 1. Schematic sketch of ferromagnetic film in discrete model.

where $i = x$, y, and z. With zero applied field, equation (4) gives the equations of state of every slice of the film. For the left surface of the film, $n = -N$, these are:

$$\frac{A}{b}\left(M_{-N,i} - M_{-N+1,i}\right) + \frac{A}{\lambda}M_{-N,i} = 0 \quad (5)$$

Similarly, the equations of state of the right surface of the film, $n = +N$, are:

$$\frac{A}{b}\left(M_{-N,i} - M_{-N+1,i}\right) + \frac{A}{\lambda}M_{-N,i} = 0 \quad (6)$$

and the equations of state of inner part of the film, $-N < n < +N$, are:

$$\alpha_2 M_{n,i} + \alpha_4 M_{n,i}\left(M_{n,x}{}^2 + M_{n,y}{}^2 + M_{n,z}{}^2\right) + \frac{A}{b^2}\left(2M_{n,i} - M_{n-1,i} - M_{n+1,i}\right) = 0 \quad (7)$$

Based on the equations (5) to (7), the discrete magnetization profiles are presented graphically by using YIG parameters. With positive extrapolation length, i.e. $\lambda = a$, where a=12.376×10^{-10}m is the lattice constant of YIG, the magnetization profiles

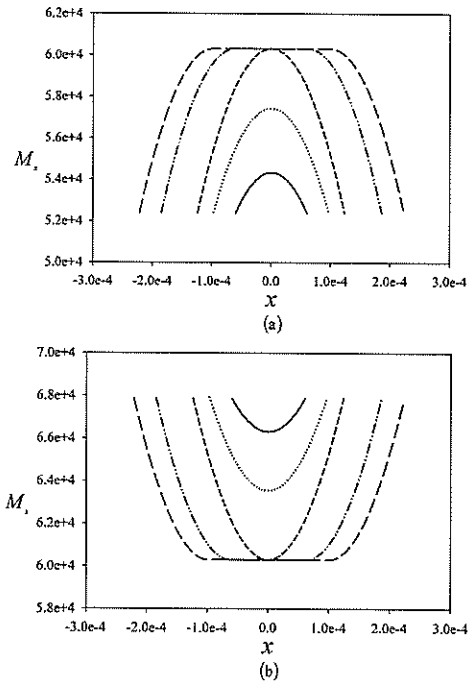

Figure 2. Magnetization profiles of x-component for five thicknesses, i.e. L_1(solid line), L_2 (dotted line), L_3 (dash line), L_4(dash-dot-dot line), and L_5(long dash line), (a) with positive extrapolation length, λ=a, and (b) with negative extrapolation length, λ=-a.

of x - component for five different thicknesses of the film are shown in Figure 2(a). These are $L_1 = 1.0\times1.0^5 a$, $L_2 = 1.6\times1.0^5 a$, $L_3 = 2.0\times1.0^5 a$, $L_4 = 3.0\times1.0^5 a$, and $L_5 = 3.6\times1.0^5 a$. As the thickness of the film increases, the magnetization profile increases. For the thick film, the slices in the middle are assumed as bulk values. For negative extrapolation length, i.e. $\lambda = -a$, the magnetization profiles of the x- component for the same set of thicknesses are shown in Figure 2(b). As the thickness of the film increases, the magnetization profile decreases. This is opposite if compared with the films with positive extrapolation length. Again, for the thick film, the magnetization of the middle slices is assumed as bulk values. The results in Figure 2 clearly show the effects of the surface parameters and thicknesses of the film to the magnetization profiles. The magnetization profiles of y - and z - components are similar to x - component. These magnetization profiles will be used as the initial values in the numerical simulations of the dynamics in ferromagnetic film.

The dynamic responses of the magnetization in each slice of the ferromagnetic film are described by the phenomenological LL equation of motion:

$$\frac{d\mathbf{M}_n}{dx} = -\gamma \mathbf{M}_n \times \Gamma \mathbf{M}_n \times \left(\mathbf{M}_n \times \mathbf{B}_{eff,n}\right) \tag{8}$$

With applied magnetic field, the effective field derived from the variation of the free energy per unit area in equation (3) is:

$$B_{eff,n,i} = -\frac{\delta G}{\delta M_{n,i}} = -\left[\frac{d}{dx}\left(\frac{\partial G}{\partial \dot{M}_{n,i}}\right) - \frac{\partial G}{\partial M_{n,i}}\right] \tag{9}$$

Since the free energy per unit area does not contain $M_{n,i}$, the first term on the right of equation (9) is zero. The effective field is simplified to

$$B_{eff,n,i} = \frac{\partial G}{\partial M_{n,i}} \tag{10}$$

In vector form, this is:

$$\mathbf{B}_{eff,n} = \frac{\partial G}{\partial M_{n,x}}\hat{i} + \frac{\partial G}{\partial M_{n,y}}\hat{j} + \frac{\partial G}{\partial M_{n,z}}\hat{k} \tag{11}$$

Explicit evaluation of (10) or (11) gives the effective fields of the left surface of the film, $n = -N$,

$$B_{eff,-N,j} = \frac{A}{b}\left(M_{-N,j} - M_{-N+1,j}\right) + \frac{A}{\lambda}M_{-N,j} \tag{12a}$$

where $j = x$ and y, and

$$B_{eff,-N,z} = \frac{A}{b}\left(M_{-N,z} - M_{-N+1,z}\right) + \frac{A}{\lambda}M_{-N,z} - bB_z(t) \tag{12b}$$

Similarly, the effective fields of the right surface of the film, $n = -N$, are:

$$B_{eff,+N,j} = \frac{A}{b}\left(M_{+N,j} - M_{+N-1,j}\right) + \frac{A}{\lambda}M_{+N,j} \tag{13a}$$

where $j = x$ and y, and

$$B_{eff,+N,z} = \frac{A}{b}\left(M_{+N,z} - M_{+N-1,z}\right) + \frac{A}{\lambda}M_{+N,z} - bB_z(t) \tag{13b}$$

Besides these, the effective fields of inner part of the film, $-N < n < +N$, are:

$$B_{eff,n,j} = b\left[\alpha_2 M_{n,j} + \alpha_4 M_{n,j}\left({M_{n,x}}^2 + {M_{n,y}}^2 + {M_{n,z}}^2\right) + \frac{A}{b^2}\left(2M_{n,j} - M_{n-1,j} - M_{n+1,j}\right)\right] \tag{14a}$$

where $j = x$ and y, and

$$B_{eff,n,z} = b\left[\alpha_2 M_{n,z} + \alpha_4 M_{n,z}\left({M_{n,x}}^2 + {M_{n,y}}^2 + {M_{n,z}}^2\right) + \frac{A}{b^2}\left(2M_{n,z} - M_{n-1,z} - M_{n+1,z}\right) - B_z(t)\right] \tag{14b}$$

Substitution of equations (12) to (14) into (8) yields the dynamic equations or equations of motion of the discrete magnetization of the film, and these are summarized in the following equations:

$$\begin{aligned}\frac{dM_{-N,x}}{dt} = {} & \left(\gamma M_{-N,y} + \Gamma M_{-N,x} M_{-N,z}\right)x \\ & \left[\frac{A}{b}M_{-N+1,z} - \frac{A}{\lambda}M_{-N,z} + bB_z(t)\right] \\ & + \left(\Gamma M_{-N,x} M_{-N,y} - \gamma M_{-N,z}\right)\left[\frac{A}{b}M_{-N+1,y} - \frac{A}{\lambda}M_{-N,y}\right] \\ & - \left(\Gamma {M_{-N,y}}^2 + \gamma {M_{-N,z}}^2\right)\left[\frac{A}{b}M_{-N+1,x} - \frac{A}{\lambda}M_{-N,x}\right]\end{aligned} \tag{15a}$$

$$\begin{aligned}\frac{dM_{-N,y}}{dt} = {} & \left(\gamma M_{-N,z} + \Gamma M_{-N,x} M_{-N,y}\right)\left[\frac{A}{b}M_{-N+1,x} - \frac{A}{\lambda}M_{-N,x}\right] \\ & + \left(\Gamma M_{-N,y} M_{-N,z} - \gamma M_{-N,x}\right)\left[\frac{A}{b}M_{-N+1,z} - \frac{A}{\lambda}M_{-N,z} + bB_z(t)\right] \\ & - \left(\Gamma {M_{-N,x}}^2 + \gamma {M_{-N,z}}^2\right)\left[\frac{A}{b}M_{-N+1,y} - \frac{A}{\lambda}M_{-N,y}\right]\end{aligned} \tag{15b}$$

$$\frac{dM_{-N,z}}{dt} = \left(\gamma M_{-N,x} + \Gamma M_{-N,x} M_{-N,z}\right)\left[\frac{A}{b} M_{-N+1,y} - \frac{A}{\lambda} M_{-N,y}\right] + \left(\Gamma M_{-N,x} M_{-N,z} - \gamma M_{-N,y}\right)\left[\frac{A}{b} M_{-N+1,x} - \frac{A}{\lambda} M_{-N,x}\right] - \left(\Gamma M_{-N,x}^{\,2} + \gamma M_{-N,y}^{\,2}\right)\left[\frac{A}{b} M_{-N+1,z} - \frac{A}{\lambda} M_{-N,z} + bB_z(t)\right] \quad (15)$$

for the left surface slice, and

$$\frac{dM_{+N,x}}{dt} = \left(\gamma M_{+N,y} + \Gamma M_{+N,x} M_{+N,z}\right)\left[\frac{A}{b} M_{+N-1,z} - \frac{A}{\lambda} M_{+N,z} + bB_z(t)\right] + \left(\Gamma M_{+N,x} M_{+N,y} - \gamma M_{+N,z}\right)\left[\frac{A}{b} M_{+N-1,y} - \frac{A}{\lambda} M_{+N,y}\right] - \left(\Gamma M_{+N,y}^{\,2} + \gamma M_{+N,z}^{\,2}\right)\left[\frac{A}{b} M_{+N-1,x} - \frac{A}{\lambda} M_{+N,x}\right] \quad (16a)$$

$$\frac{dM_{+N,y}}{dt} = \left(\gamma M_{+N,z} + \Gamma M_{+N,x} M_{+N,y}\right)\left[\frac{A}{b} M_{+N-1,x} - \frac{A}{\lambda} M_{+N,x}\right] + \left(\Gamma M_{+N,y} M_{+N,z} - \gamma M_{+N,x}\right)\left[\frac{A}{b} M_{+N-1,z} - \frac{A}{\lambda} M_{+N,z} + bB_z(t)\right] - \left(\Gamma M_{+N,x}^{\,2} + \gamma M_{+N,z}^{\,2}\right)\left[\frac{A}{b} M_{+N-1,y} - \frac{A}{\lambda} M_{+N,y}\right] \quad (16b)$$

$$\frac{dM_{+N,z}}{dt} = \left(\gamma M_{+N,x} + \Gamma M_{+N,y} M_{+N,z}\right)\left[\frac{A}{b} M_{+N-1,y} - \frac{A}{\lambda} M_{+N,y}\right] + \left(\Gamma M_{+N,x} M_{+N,z} - \gamma M_{+N,y}\right)\left[\frac{A}{b} M_{+N-1,x} - \frac{A}{\lambda} M_{+N,x}\right] - \left(\Gamma M_{+N,x}^{\,2} + \gamma M_{+N,y}^{\,2}\right)\left[\frac{A}{b} M_{+N-1,z} - \frac{A}{\lambda} M_{+N,z} + bB_z(t)\right] \quad (16c)$$

for the right surface slice, and

$$\frac{dM_{n,x}}{dt} = b\left(\gamma M_{n,y} + \Gamma M_{n,x} M_{n,z}\right)\left[\frac{A}{b^2}\left(M_{n-1,z} + M_{n+1,z}\right) + B_z(t)\right] + b\left(\Gamma M_{n,x} M_{n,y} - \gamma M_{n,z}\right)\left[\frac{A}{b^2}\left(M_{n-1,y} + M_{n+1,y}\right)\right] - b\left(\Gamma M_{n,y}^{\,2} + \gamma M_{n,z}^{\,2}\right)\left[\frac{A}{b^2}\left(M_{n-1,x} + M_{n+1,x}\right)\right] \quad (17a)$$

$$\frac{dM_{n,y}}{dt} = b\left(\gamma M_{n,z} + \Gamma M_{n,x} M_{n,y}\right)\left[\frac{A}{b^2}\left(M_{n-1,x} + M_{n+1,x}\right)\right] + b\left(\Gamma M_{n,y} M_{n,z} - \gamma M_{n,x}\right)\left[\frac{A}{b^2}\left(M_{n-1,z} + M_{n+1,z}\right) + B_z(t)\right] - b\left(\Gamma M_{n,x}^{\,2} + \gamma M_{n,z}^{\,2}\right)\left[\frac{A}{b^2}\left(M_{n-1,y} + M_{n+1,y}\right)\right] \quad (17b)$$

$$\frac{dM_{n,z}}{dt} = b\left(\gamma M_{n,x} + \Gamma M_{n,y} M_{n,z}\right)\left[\frac{A}{b^2}\left(M_{n-1,y} + M_{n+1,y}\right)\right] + b\left(\Gamma M_{n,x} M_{n,z} - \gamma M_{n,y}\right)\left[\frac{A}{b^2}\left(M_{n-1,x} + M_{n+1,x}\right)\right] - b\left(\Gamma M_{n,x}^{\,2} + \gamma M_{n,y}^{\,2}\right)\left[\frac{A}{b^2}\left(M_{n-1,z} + M_{n+1,z}\right) + B_z(t)\right] \quad (17c)$$

for the inner part of the film, with $-N < n < +N$. Equations (15) to (17) are solved numerically by using forth order Runge-Kutta Method, and the results are presented graphically in Section 3.

NUMERICAL RESULTS AND DISCUSSION

Frequency effects

In the numerical simulations of equations (15) to (17), the material constants of YIG has been used. These are a=12.376×10^{-10}m for lattice constant, M_S=1.39×10^5 Am^{-1} for saturation magnetization, T_C=560K for transition temperature, γ =1.76×10^{11}T^{-1}S^{-1} for gyromagnetic ratio, and the damping constant is assumed as η = 0.01. With applied sinusoidal magnetic field, the simulated results after each time slice are taken as the average of the magnetization in the film, and these are given as:

$$\overline{M}_i(t) = \frac{1}{h}\sum_{n=-N}^{+N} M_{i,n}(t) \text{ and } \frac{d\overline{M}_i(t)}{d} = \frac{1}{h}\sum_{n=-N}^{+N} \frac{dM_{i,n}(t)}{d} \quad (18)$$

where $i = x$, y, and z.

Initially, the extrapolation length is set to a positive value, i.e. $\lambda = a$. In order to see the effects of applied frequencies, the thickness is fixed at $L_2 = 1.6\times1.0^5\, a$ and three different frequencies, i.e. f = 25 Hertz, 50 Hertz, and 10 Hertz are chosen in the numerical simulations. Figure 3 shows a full cycle of time dependent applied field for f=25 Hertz, with amplitude B_0=1.0×10^{-15} Tesla. The information of the dynamic behaviors with respect to the applied field is based on the numerical curves of $\overline{M}_i$ versus t, $\overline{M}_i$ versus $B_z(t)$, and $d\overline{M}_i/dt$ versus $\overline{M}_i$. The graphs with significant effects of B_0 are shown in Figures 4 to 6. The numerical simulations show that there is no change in $\overline{M}_x$, $\overline{M}_y$, and $\overline{M}_z$ for $B_0 \le 3.0\times10^{-12}$ Tesla, because of the applied field is too weak. This is followed by gradual increase in the amplitude of applied field. For $B_0 \le B_C$, where B_C=5.0×10^{-4} Tesla, the period of the dynamic responses of $\overline{M}_z$

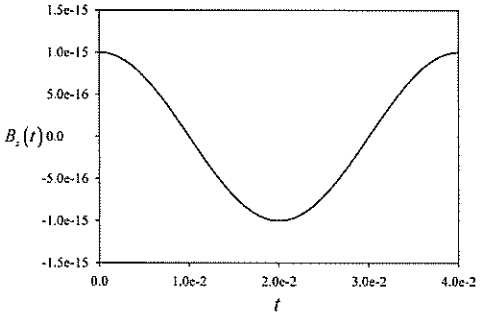

Figure 3. A full cycle of $B_z(t) = B_0\cos(\omega t)$ versus t. The amplitude is B_0=1.0×10^{-15} Tesla with f=50 Hertz.

are the same as input frequencies. These are shown in Figure 4(a) for three different input frequencies. The corresponding phase portraits are shown in Figures 4(b) and 4(c). The dynamic behaviors of $\overline{M}_x$ and $\overline{M}_y$ are similar to $\overline{M}_z$. This means that the amplitude of this applied field is still too weak to excite any nonlinear behavior. These quasi-periodic responses remain for the higher frequencies, i.e. f=50 Hertz and 10 Hertz. However, the amplitudes of $\overline{M}_z$ decrease as the frequency increase. This can be seen in Figure 4(a), with $\overline{M}_z(t)_{f=100\,\text{Hertz}} < \overline{M}_z(t)_{f=50\,\text{Hertz}} < \overline{M}_z(t)_{f=25\,\text{Hertz}}$. This means as the frequency increases, the response of the ferromagnetic film decreases. The corresponding phase portraits in Figures 4(b) and 4(c) show the same features, with the size of the loops decreasing with increasing frequencies.

The onset of chaotic responses or non-periodicity are observed only in $\overline{M}_x$ and $\overline{M}_y$ components for $B_0 > B_C$. The quasi-periodic response remains in $\overline{M}_z$ component. For B_0=20.0B_C, the period of dynamic responses in $\overline{M}_x$ are being eight-folded for f =25 Hertz, four-folded for f =50 Hertz, and two-folded for f = 100 Hertz. These are shown in Figure 5(a). The corresponding phase portraits are shown in Figures 5(b) and 5(c). These responses are chaotic because the phase portraits neither repeat nor overlap. The dynamic behavior of $\overline{M}_y$ are similar to $\overline{M}_x$. Further numerical simulations show that when

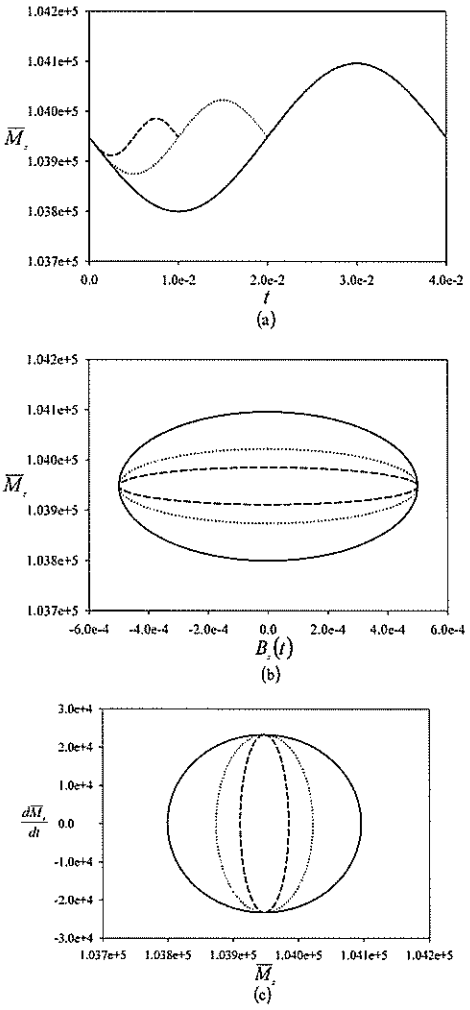

Figure 4. Phase portrait of magnetization for three frequencies, f=25 Hertz (solid line), f=50 Hertz (dotted line), and f = 100 Hertz (dash line) with B_C=5.0×10^{-4} Tesla. (a) $\overline{M}_z$ versus t, (b) $\overline{M}_z$ versus $B_z(t)$, (c) $d\overline{M}_z/dt$ versus $\overline{M}_z$.

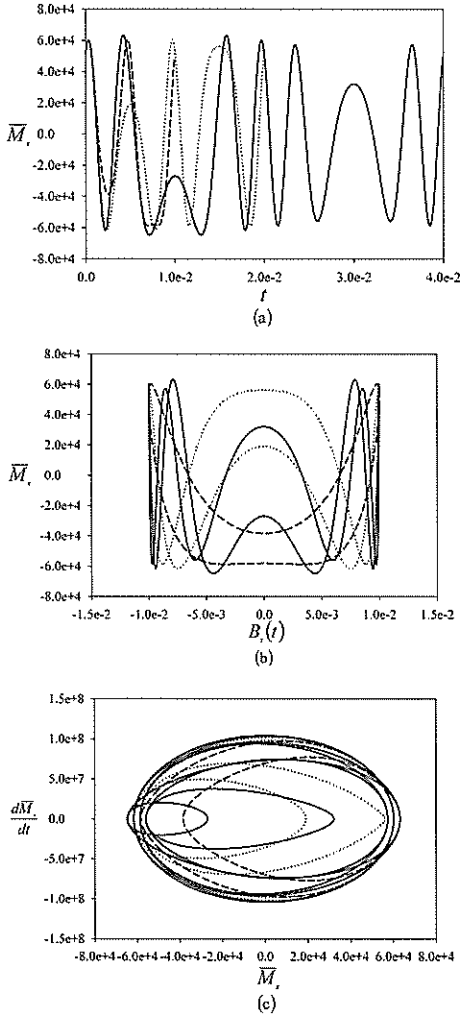

Figure 5. Phase portrait of magnetization for three frequencies, f =25 Hertz (solid line), f =50 Hertz (dotted line), and f =100 Hertz (dash line) with B_0=20.0B_C. (a) $\overline{M}_x$ versus t, (b) $\overline{M}_x$ versus $B_z(t)$, (c) $d\overline{M}_x/dt$ versus $\overline{M}_x$.

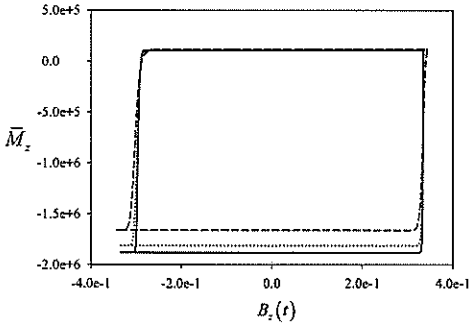

Figure 6. $\overline{M}_z$ versus $B_z(t)$ with $B_0 = 669.7B_C$ for f=25 Hertz (solid line), $B_0 = 675.0B_C$ for f =50 Hertz(dotted line), and $B_0 = 685.9B_C$ for $f = 100$ Hertz (dash line).

the amplitude of applied field is being increased, the chaotic responses become more intense. These chaotic responses of $\overline{M}_x$ and $\overline{M}_y$ can be observed only with $B_0 < 670.1B_C$ for f=25 Hertz, $B_0 < 675.3B_C$ for f=50 Hertz, and $B_0 < 668.4B_C$ for $f = 100$ Hertz.

The range of B_0 for $\overline{M}_z$ to show nonlinear responses is different as compared to $\overline{M}_x$ and $\overline{M}_y$ components. For $B_0 > 160.0B_C$, the quasi-periodic responses in $\overline{M}_z$ disappear. When $B_0 \geq 650.0B_C$, the hysteresis effects become obvious. The hysteresis loops can be observed with $669.7B_C \leq B_0 \leq 670.1B_C$ for f =25 Hertz, $674.9B_C \leq B_0 \leq 675.3B_C$ for f =50 Hertz, and $685.9B_C \leq B_0 \leq 686.4B_C$ for $f = 100$ Hertz. Complete hysteresis loop for three different frequencies are shown in Figure 6 with $B_0 = 669.7B_C$ for f =25 Hertz, $B_0 = 675.0B_C$ for f =50 Hertz, and $B_0 = 685.9B_C$ for $f = 100$ Hertz.

Thickness effects

In order to see the effects of thicknesses of the film, the frequency is fixed at f=25 Hertz, and five different thicknesses of the film are chosen, these are $L_1 = 1.0\times1.0^5 a$, $L_2 = 1.6\times1.0^5 a$, $L_3 = 2.0\times1.0^5 a$, $L_4 = 3.0\times1.0^5 a$, and $L_5 = 3.6\times1.0^5 a$, which are the same as the thicknesses of the magnetization profiles in Figure 2. The numerical simulations show that there is no change in $\overline{M}_x$, $\overline{M}_y$, and $\overline{M}_z$ with $B_0 \leq 3.0\times10^{-12}$ Tesla. This is followed by gradual increase in the amplitude of applied field. The period of the dynamic responses of $\overline{M}_x$ are the same as input frequency with $B_0 \leq B_C$. These are shown in Figure 7(a) for five different thicknesses of the film with B_0=20.0B_C. The corresponding phase portraits are shown in Figures 7(b) and 7(c). The dynamic behaviors of $\overline{M}_y$ and $\overline{M}_z$ are similar to $\overline{M}_x$. This means that the amplitude of

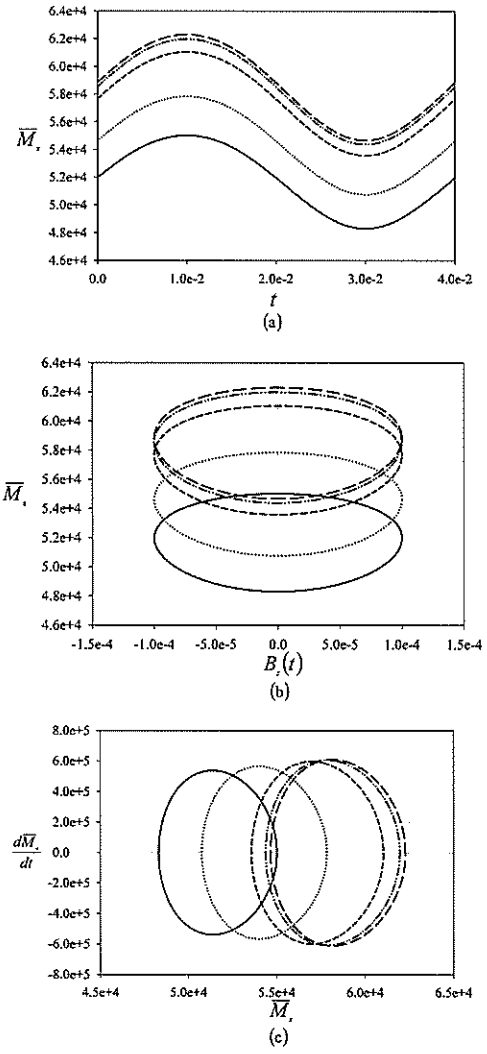

Figure 7. Phase portrait of magnetization for five thicknesses, i.e. L_1 (solid line), L_2 (dotted line), L_3 (dash line), L_4 (dash-dot-dot line), and L_5 (long dash line) with $B_0 = 0.2B_C$ and positive extrapolation length, $\lambda = a$. (a) $\overline{M}_x$ versus t, (b) $\overline{M}_x$ versus $B_z(t)$, (c) $d\overline{M}_x/dt$ versus $\overline{M}_x$.

this applied field is still too weak to excite any nonlinear behavior. However, the amplitude of $\overline{M}_x$ increases as the thickness of the film increases. The corresponding phase portraits show the same features in Figures 7(b) and 7(c), with the loops is being raised and increased in size as the thicknesses of the film increases. These results clearly show the effects of amplitudes of the applied field and the thicknesses of the film to the dynamic responses of $\overline{M}_x$.

The onset of chaotic responses are observed only in $\overline{M}_x$ and $\overline{M}_y$ components for $B_0 > B_C$. The quasi-periodic response remains in $\overline{M}_z$ component. For $B_0 = 4.0B_C$, the period of dynamic responses in

$\overline{M}_x$ are two-folded with five different thicknesses of the film. These are shown in Figure 8(a). The corresponding phase portraits are shown in Figures 8(b) and 8(c). These responses are chaotic because the phase portraits neither repeat nor overlap. The dynamic responses of $\overline{M}_y$ are similar to $\overline{M}_x$. Further numerical simulations show that as the amplitude of applied field is being increased, the chaotic responses become more intense. These chaotic responses of $\overline{M}_x$ and $\overline{M}_y$ can be observed only with $B_0 < 670.1B_C$ for L_1, $B_0 < 669.9B_C$ for L_2, and $B_0 < 69.7\ B_C$ for L_3, L_4 and L_5.

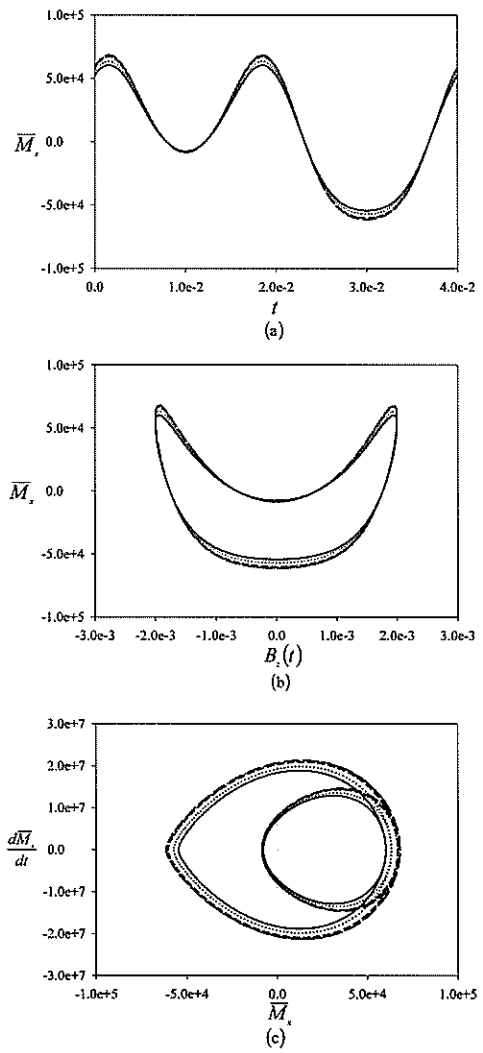

Figure 8. Phase portrait of magnetization for five thicknesses, i.e. L_1 (solid line), L_2 (dotted line), L_3 (dash line), L_4 (dash-dot-dot line), and L_5 (long dash line) with $B_0 = 4.0B_C$ and positive extrapolation length, $\lambda = a$. (a) $\overline{M}_x$ versus t, (b) $\overline{M}_x$ versus $B_z(t)$, (c) $d\overline{M}_x/dt$ versus $\overline{M}_x$.

The range of B_0 for $\overline{M}_z$ to show nonlinear responses is different as compared to $\overline{M}_x$ and $\overline{M}_y$ components. For $B_0 > 160.0B_C$, the quasi-periodic responses in $\overline{M}_z$ disappear. When $B_0 > 650.0B_C$, the hysteresis effects become obvious. The hysteresis loops can be observed with $669.7B_C \le B_0 < 670.1B_C$ for L_1, $669.6B_C \le B_0 < 669.7\ B_C$ for L_2, $669.5B_C \le B_0 < 669.7\ B_C$ for L_3, $669.4B_C \le B_0 < 669.7B_C$ for L_4 and L_5. Complete hysteresis loop for five different thicknesses of the film are shown in Figure 9 with $B_0 = 669.6B_C$.

Negative extrapolation length

In order to observe the effects of negative extrapolation length, it is fixed at a negative value, i.e., $\lambda = -a$, and the frequency is fixed at f=25 Hertz, and the same set of five different thicknesses of the film are chosen. The numerical simulations show that there is no change in $\overline{M}_x$, $\overline{M}_y$, and $\overline{M}_z$ with $B_0 \le 3.0\times10^{-12}$ Tesla. As the amplitude of applied field increases, the quasi-periodic responses of $\overline{M}_x$ are observed with $B_0 \le B_C$, where the periods are the same as input field. These are shown in Figure 10(a) for five different thicknesses of the film with $B_0 = 0.2B_C$. However, the amplitudes of $\overline{M}_x$ decreases as the thickness of the film increases. These are opposite as compared with the results with positive extrapolation length. These results clearly show the effects of the surface parameters. As the thicknesses of the film increased, the magnetization profiles decreased. The corresponding phase portraits show the same features in Figures 10(b) and 10(c), with the loops is being dropped and decreased in size as the thicknesses of the film increases. The dynamic behaviors of $\overline{M}_y$ and $\overline{M}_z$ are similar to $\overline{M}_x$.

The onset of chaotic responses are observed

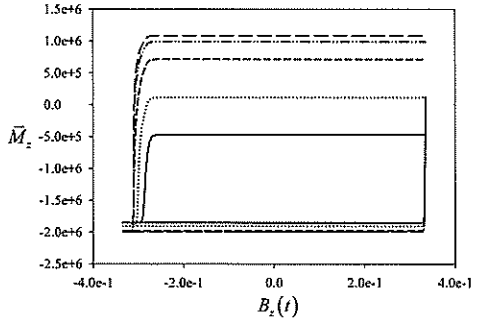

Figure 9. $\overline{M}_z$ versus $B_z(t)$ with $\lambda = a$ for L_1 (solid line), L_2 (dotted line), L_3 (dash line), L_4 (dash-dot-dot line), and L_5 (long dash line) with $B_0 = 669.6B_C$.

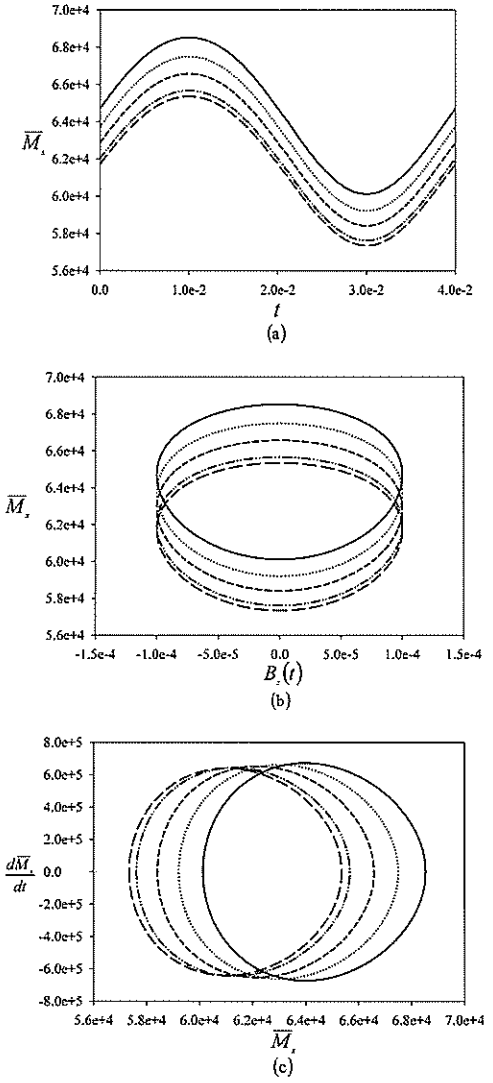

Figure 10. Phase portrait of magnetization for five thicknesses, i.e. L_1 (solid line), L_2 (dotted line), L_3 (dash line), L_4 (dash-dot-dot line), and L_5 (long dash line) with $B_0 = 0.2B_C$ and negative extrapolation length, $\lambda = -a$. a) $\overline{M}_x$ versus t, (b) $\overline{M}_x$ versus $B_z(t)$, (c) $d\overline{M}_x/dt$ versus $\overline{M}_x$.

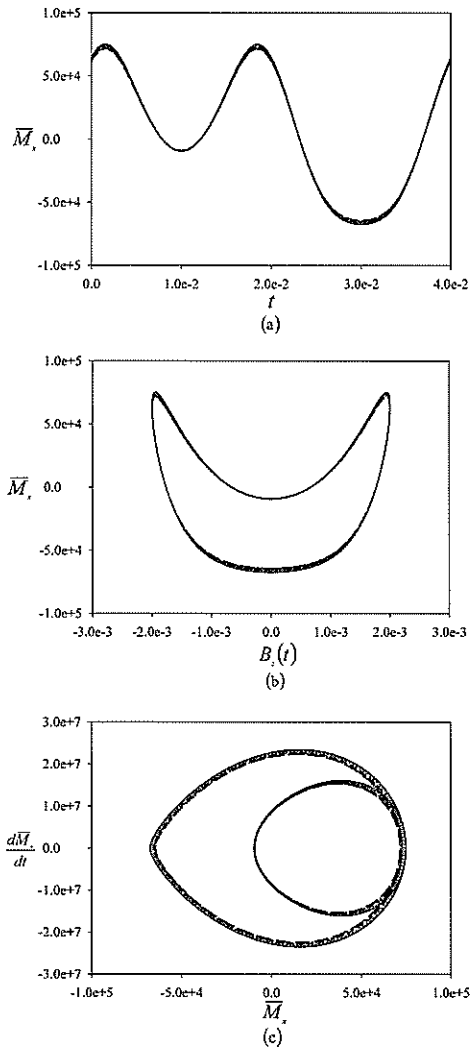

Figure 11. Phase portrait of magnetization for five thicknesses, i.e. L_1 (solid line), L_2 (dotted line), L_3 (dash line), L_4 (dash-dot-dot line), and L_5 (long dash line) with $B_0 = 4.0B_C$ and negative extrapolation length, $\lambda = -a$. a) $\overline{M}_x$ versus t, (b) $\overline{M}_x$ versus $B_z(t)$, (c) $d\overline{M}_x/dt$ versus $\overline{M}_x$.

only in $\overline{M}_x$ and $\overline{M}_y$ components for $B_0 > B_C$. The quasi-periodic response remains in $\overline{M}_z$ component. For $B_0 = 4.0B_C$, the period of dynamic responses in $\overline{M}_x$ are two-folded with five different thicknesses of the film. These are shown in Figure 11(a). The corresponding phase portraits are shown in Figures 11(b) and 11(c). The dynamic responses of $\overline{M}_y$ are similar to $\overline{M}_x$. Further numerical simulations show that as the amplitude of applied field is being increased, the chaotic responses become more intense. These chaotic responses of $\overline{M}_x$ and $\overline{M}_y$ can be observed only with $B_0 < 669.9B_C$ for L_1 to L_5.

The range of B_0 for $\overline{M}_z$ to show nonlinear responses is different as compared to $\overline{M}_x$ and $\overline{M}_y$ components. For $B_0 > 160.0B_C$, the quasi-periodic responses in $\overline{M}_z$ disappear. When $B_0 > 650.0B_C$, the hysteresis effects become obvious. The hysteresis loops can be observed with $669.0B_C \le B_0 < 669.3B_C$ for L_1, $669.1B_C \le B_0 < 669.3B_C$ for L_2, $669.2B_C \le B_0 < 669.3B_C$ for L_3 and L_4, $B_0 = 669.3B_C$ for L_5. With $B_0 = 669.2B_C$, hysteresis loop for five different thicknesses of the film are shown in Figure 12.

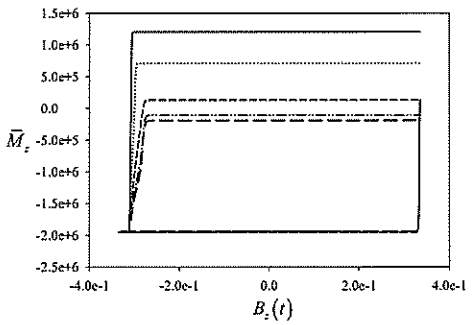

Figure 12. $\overline{M}_z$ versus $B_z(t)$ with $\lambda = -a$ for L_1 (solid line), L_2 (dotted line), L_3 (dash line), L_4 (dash-dot-dot line), and L_5 (long dash line) with $B_0 = 669.2B_C$.

CONCLUSION

The main focus of the study is the formulation of dynamic equations of a ferromagnetic film via discrete model. By using the forth-order Runge-Kutta method, the observation of chaotic responses in the average magnetization is determined by proper selection of initial conditions of $\overline{M}_i$. The dynamic behaviours of the entire film are extracted from the average magnetizations versus time and the corresponding phase portrait.

The effects of applied frequencies are exhibited by fixing the extrapolation length, $\lambda = a$, and thickness, $L_2 = 1.6\times1.0^5 a$. The chosen three different frequencies, i.e. f=25 Hertz, 50 Hertz , and 10 Hertz in the numerical simulations show that as the frequency increases, the bifurcations of the periods in $\overline{M}_x$ and $\overline{M}_y$ are decreased. This means the chaotic responses is weaker as the frequency increases. In other words, in order to see the same amounts of period bifurcations as the frequency increases, the amplitude of the applied field has to increase as well. For $\overline{M}_z$ component, the analysis shows that the size of the hysteresis curve depends on frequencies of the applied field, as the frequency increases, the hysteresis curve become narrower.

In order to see the effects of thicknesses of the film, the extrapolation length and frequency are fixed at $\lambda = a$ and f=25 Hertz, and five different thicknesses of the film are chosen, i.e. L_1 to L_5 in the numerical simulations. The range of B_0 for the occurrence of chaotic responses and hysteresis effects decreases as the thickness increases. For films with negative extrapolation length, i.e. $\lambda = -a$, the conclusion is the same.

From the numerical simulations, we managed to conclude that with the presence of low frequencies and low amplitudes of applied fields, which can be generated easily in research laboratory, can excite various nonlinear responses in the ferromagnetic films, e.g. multiple-folded of input frequencies or period bifurcations, chaotic dynamics of the magnetizations, and hysteresis effects, which are strongly dependent on initial conditions. Besides these, the surface parameters and thicknesses of the film also show distinctive effects in the chaotic responses of a ferromagnetic film. We conclude that the Landau phenomenological model and classical approaches, i.e. Landau free energy expansions, calculus of variations, and LL torque equation of motion, can exhibit the rich intrinsic nonlinear and chaotic phenomena in the ferromagnetic system.

Acknowledgements – This study was supported by USM Fellowship, Institute of Postgraduate Studies, Universiti Sains Malaysia and FRGS Grant, Ministry of Higher Education, Malaysia.

REFERENCES

1. Gerber R., Wright C.D. and Asti G. (1994) *Applied Magnetism*. Klumer Academic Publishers, Netherlands.
2. Kaganov M.I. and Omel' Yanchuk A.N. (1972) Phenomenological theory of phase transition in a thin ferromagnetic plate. *Soviet Physics JETP* **34**(4): 895-898.
3. Binder K. and Hohenberg P.C. (1972) Phase transitions and static spin correlations in Ising Models with free surfaces., *Physical Review* B **6**(9): 3461-3487.
4. Binder K. and Hohenberg P.C. (1974) Surface effects on magnetic phase transitions. *Physical Review* B **9**(5): 2194-2214.
5. Sukiennicki A. (1976) Magnetic phase transition in thin films. *IEEE Transactions on Magnetics Mag.* **12**(12): 90-95.
6. Jang H. and Grimson M.J. (2001) Hysteresis and

the dynamic phase transition in thin ferromagnetic films. *Physical Review* E **63**: 066119-1-066119-10.

7. Liu D. and Garcia-Cervera C. (2005) Magnetic switching of ferromagnetic thin films under thermal perturbation. *Journal of Applied Physics* **98**: 023903-1-023903-10.
8. Yan S.S., Garmestani H., Tian Y.F., Hu R.W., Chen Y.X., Liu G.L. and Mei L.M. (2006) Free boundary domain wall pinning model for the magnetization reversal in magnetic thin films. *Japanese Journal of Applied Physics* **45**(1A): 93-98.
9. Nozaki Y. and Matsuyama K. (2006) Numerical analysis of successive ballistic rotation of magnetization caused by an application of sinusoidal magnetic fields. *Japanese Journal of Applied Physics* **45**(29): L758-L760.
10. Ooi P.C., Ishibashi Y., Lim S.C. and Osman J. (2007) Numerical investigation of polarization reversal characteristics in a ferroelectric thin film. *Ferroelectrics* **355**: 1-7.
11. Borisov A.B., Filippov B.N., Zverev V.V. and Rubinstein B.Y. (1992) On the magnetization chaotic dynamics in the ferromagnetic resonance region. *Journal of Magnetism and Magnetic Materials* **110**: 202-208.
12. Toh P.L. and Lim S.C. (2009) Study of chaotic dynamics and hysteresis in ferromagnetic film. *Jurnal Fizik Malaysia* **30**(1&2) (in press).
13. Kumar P. (1974) Magnetic phase transition at a surface: Mean field theory. *Physics Review* B **10**(7): 2928-2933.
14. Lubensky T.C. and Rubin M.H. (1975) Critical phenomena in semi-infinite systems. I. ε Expansion for positive extrapolation length. *Physical Review* B **11**(11): 4533-4546.

Journal of Science and Technology in the Tropics (2009) **5**: 151-155

Cytotoxic chemical constituents of *Artocarpus kemando* (Moraceae)

Siow Hwa Teo[1], Gwendoline Cheng Lian Ee[1*], Marwadi Rahmani [1], Chan Kiang Lim[2] and Choon Fah Joseph Bong[3]

[1]Department of Chemistry, Faculty of Science, Universiti Putra Malaysia, 43400 Serdang, Selangor, Malaysia

[2]Department of Chemical Science, Faculty of Science, Engineering & Technology, Universiti Tunku Abdul Rahman, 31900 Kampar, Perak, Malaysia

[3]Department of Crop Science, Faculty of Agriculture & Food Sciences, Universiti Putra Malaysia Bintulu Campus, 97008 Bintulu, Sarawak, Malaysia

(*E-mail: gwen@fsas.upm.edu.my)

Received 02-12-2009; accepted 10-12-2009

ABSTRACT The stem bark of *Artocarpus kemando* furnished 24-methylenecycloartenyl acetate (fatty acyl ester) **(1)** together with cycloartobiloxanthone **(2)**. Compound **1** was obtained for the first time from this species. The structures of both compounds were determined using NMR and MS analysis. A cytotoxic study showed that the crude extract of the stem bark of *Artocarpus kemando* was significantly active against the HL-60 (Human promyelocytic leukemia cell) and IRM-32 (Human neuroblastoma cell) cell lines. This is the first report on the cytotoxic activity of *Artocarpus kemando*.

Keywords *Artocapus kemando* – triterpenoid – xanthone – cytotoxic

INTRODUCTION

The genus *Artocarpus* from the Moraceae family which consists of approximately 50 species is widely distributed in the tropical and subtropical regions, including Indonesia [1, 2].

Various triterpenes have been previously reported from the genus *Artocarpus* [3]. A majority of the phenolic compounds from this species are primarily flavonoids, apart from the stilbenoids and 2-arylbenzofuran [4]. Flavonoids from this plant and other species of *Artocarpus* have been shown to exhibit anti-inflammatory [5], antioxidative [6], antiplatelet aggregation [7], 5α-reductase activities [8], inhibition of cathepsin K [9], and cyctotoxicity [10]. These activities are mainly contributed by the phenolic constituents from the plant.

The wood is locally used as light-weight hard-wood, especially for household utensils and the fruits are edible. This paper reports the isolation and the identification of 24-methylenecycloartenyl acetate **(1)** and cycloartobiloxanthone **(2)** from the stem bark of *Artocarpus kemando* as well as the cytotoxic activities of the extracts.

MATERIALS AND METHODS

General

Melting points were determined on a melting point apparatus and are uncorrected. IR spectra were recorded in KBr pellet on a Perkin-Elmer FT-IR Spectrum BX spectrophotometer. Mass spectral measurement was obtained on a Shimadzu GCMS-QP5050A spectrometer. ^{1}H and ^{13}C NMR spectra were recorded in $CDCl_3$ using TMS as internal standard on a JOEL JNM-LA 400 spectrometer at 400 and 100 MHz, respectively. VLC was carried out using Merck Kieselgel 60 PF_{254} (containing gypsum), gravity liquid chromatography with Merck Kieselgel 60 Mesh 230-400 (40-63 microns), and TLC analysis on precoated Si-gel plates (Merck Kieselgel 60 F_{254}, 0.25 mm).

Plant material

Samples of the stem bark of *A. kemando* were collected in May 2007, from Sri Aman, Sarawak, Malaysia.

Extraction and isolation

The milled, air-dried stem bark (4.7 kg) was extracted exhaustively with n-hexane and then with ethanol.

and Viperidae) and two species of turtles from two families (Trionychidae and Bataguridae).

All except two species were hand caught. The exceptions were the Water monitor lizard *Varanus salvator* and the Reticulated python *Python reticulatus* which were sighted. All these reptilian species are common in forested areas throughout the peninsula [10-13].

Mammals

A total of 74 mammal species was identified (Appendix 2). These comprised of 41 non-volant mammals from 17 families, and 33 volant mammals from 8 families. Of these 15 species were sighted, 3 species were based on tracks and vocalization, and two species were shot by the resident Orang Asli.

Non-volant mammals

The 41 non-volant mammals comprised of flying lemur, insectivores, tree-shrews, primates, rodents small carnivores and hoofed mammals (Appendix 2). All the species identified are of common occurrence in forest areas throughout the mainland [2, 14, 15]. However, the presence of some interesting mammals such as the Moonrat, three species of flying squirrels, the small carnivores (Malay weasel, Linsang and Flat-headed cat) suggests that the forests still provide sustainable food resources and habitat niches for the survival of these less common animals despite the deteriorating conditions, particularly that of BFR.

The total absence of the four species of cercopithecid monkeys (Long-tailed and Pig-tailed macaques and the Dusky and banded Leaf monkeys) in BFR was due to disturbance factor (blasting and drilling) as these monkeys are normally associated and commonly seen in highly disturbed environments, such as degenerated secondary forest type [16]. Hunting, using shot guns for animals, like mouse-deer and other animals by the Orang Asli and also by orchard owners for pest animals was another factor for larger mammals moving out to the adjacent SLFR where there were less deleterious activities. This is evidenced by the lower number of non-volant mammals trapped and sighted at BFR compared to SLFR.

During the period of study, large mammals, such as the tiger, panther, deer, etc. were not detected apart from the primates, in both the forest areas. It is very probable that most of these large mammals had moved uphill into the SLFR on the Ulu Langat side.

Volant mammals

The 33 chiropteran species from both the forest areas comprised 8 species of fruit bats and 25 species of insectivorous bats (from eight families). All the bat species examined are commonly found in forest areas [3, 17, 18]. According to the orchard farmers there, three species of fruit bats were serious pests of orchards during flowering and fruiting seasons. Many of these species were captured and sold to gourmet restaurants.

Birds

A total of 135 species of birds was identified (Appendix 3). Of these 121 species were recorded in SLFR compared to 72 in BFR. The lower species number in the BFR was probably related to the high intensity of disturbances from preliminary construction activities during the survey periods. Of the 135 species, 126 were resident species, 4 migrants and 5 both residents and augmented by migrants. The survey recorded only four birds of prey. This may partly be attributed to the very wet and gloomy weather during the survey. Five hornbill species were recorded mainly from the forested hill slopes of SLFR with at least one group of hornbill in the area due to the fruiting season. During our stay, two Rhinoceros hornbills were shot by an Orang Asli.

Among the 135 recorded species, two are 'Not Protected' (Appendix 3: Nos. 78, 135), seven are 'Protected' (Appendix 3: Nos1, 40, 50-52, 79, 81) with the rest of the 126 species classified as 'Totally Protected' under the Protection of Wildlife Act 1972 (Act 76), 1994. Twenty five of the species in the BFR and SLFR are globally classified as being of international conservation concern (Appendix 3: LR (nc)). This represents 17.0% of the birds listed for Malaysia in Birdlife International's 2001's Red Data Book on the "Threatened Birds of Asia" where 147 species (including birds from Sabah and Sarawak) are given that category. However, in the Malaysian context, all these 25 species are quite common and widely distributed throughout the country, including several conservation areas such as Taman Negara, Krau Wildlife Reserve, Endau Rompin National Park and Danum Valley.

The n-hexane and ethanol extracts, on removal of solvent under reduced pressure, gave light brown residues, weighing 23 g and 50 g, respectively. The ethanol extract of *A. kemando* was chromatographed on a silica gel vacuum column chromatography using a stepwise gradient system (hexane/$CHCl_3$, $CHCl_3$/EtOAc, EtOAc/Me_2O and MeOH) to give 20 fractions. Fractions 4-6 which appeared as a yellow sticky solid were combined. It was boiled with methanol and cooled. This afforded 24-methylenecycloartenyl acetate (50 mg) **(1)** after repeated washing with methanol.Recrystallization from methanol resulted in a white solid. Combination and purification of fractions 13-16 by column chromatography (SiO_2; n-hexane/ $CHCl_3$, $CHCl_3$/ Me_2O and Me_2O gradient) gave subfractions 8 and 10 which showed promising spots on the TLC plate. Elution with $CHCl_3$ and $CHCl_3$/ Me_2O (19 : 1) on both fractions afforded cycloartobiloxanthone **(2)**. The structures of compounds **1** and **2** were elucidated using IR, NMR and MS data.

Cell cultures

Two human cancer cell lines were used. They were HL-60 and the IRM-32 cell lines. The HL-60 cell line was obtained from National Cancer Institute (NCI), USA and IRM-32 was provided by Health Science Research Resources Bank, Japan. Cells were cultured in Dulbecco's Modified Eagle's Medium (DMEM) with 5% fetal bovine serum (FBS), 100 IU/mL penicillin and 100 g/mL streptomycin by using 25 cm^2 flask in a 37 °C incubator with 5 % CO_2.

Cytotoxicity assay

The exponential growing HL-60 and IRM-32 cells were obtained by plating each well with 100 µL of stock culture (1×10^5 cells/mL) in 96-well microliter plate and incubated at 37°C for 24 hours. The stock solution was prepared at a concentration of 10 mg/mL by dissolving 10 mg of sample (compound) in 10 mL of dimethylsulfoxide (DMSO). Serial dilution of the stock solution in the growth medium provided seven sample solutions at concentrations of 2.5, 5.0, 7.5, 10.0, 20.0, 30.0 and 40.0 µg/mL. The growth medium was removed from the wells, washed well and the treated with 100 µL of varying concentration of sample solution. Controls contained only untreated cell population in 100 µL of growth medium.

MTT assay

HL-60 and IRM-32 cells growing exponentially in 96-well micro plate were treated with a range of concentrations (2.5-40.0 µg/mL) of each sample for 3 days. Each concentration of sample was performed in triplicate and the culture plate was incubated for 3 days at 37 °C, 5 % CO_2 and 90 % humidity. After treatment, 10 µL of the MTT labeling reagent (0.5 mg/mL) was added to each well. The plate was then incubated further for 4 hours at 37 °C with 5 % CO_2. After that, 100 µL of the solubilized solution was added to each well and the plate was allowed to stand overnight in the incubator at 37 °C with 5% CO_2. Absorbance was measured using ELISA spectrophotometer (EL_x 800) at wavelength 550 nm. The percentage of MTT reduction was calculated by comparing the absorbance of treated cells to that of untreated control cells.

24-methylenecycloartenyl acetate (1): white solid; mp 116-119°C (Lit. 114-117 °C) [11]; IR (KBr) υ_{max} cm^{-1}: 2942 (OH), 1734 (C=O group of an ester), 1456 (C=C), 1374, 1248, 1094 (C-O); EIMS m/z: 483 $[M]^+$, 422, 408, 175, 125, 109, 95, 81, 69; ^1H NMR (400 MHz, $CDCL_3$): δ 4.57 (1H, m, H-3), 0.97 (1H, s, H-18), 0.34 (1H, d, *J*= 3.7, H-19a), 0.58 (1H, d, *J*= 3.7, H-19b), 0.90 (1H, d, *J*= 4.6, H-21), 1.04 (1H, d, *J*= 1.8, H-26), 1.03 (1H, d, *J*= 2.8, H-27), 0.90 (1H, d, *J*= 4.6, H-28), 0.85 (1H, d, *J*= 4.6, H-29), 0.85 (1H, s, H-30), 4.66, 4.71 (2H, s, H-31) and ^{13}C NMR (100 MHz, $CDCl_3$): δ31.57 (C-1), 25.78 (C-2), 80.63 (C-3), 39.41 (C-4), 47.12 (C-5), 20.90 (C-6), 28.12 (C-7), 47.80 (C-8), 20.90 (C-9), 25.92 (C-10), 26.46 (C-11), 35.50 (C-12), 45.25 (C-13), 48.77 (C-14), 32.82 (C-15), 26.77 (C-16), 52.21 (C-17), 17.95 (C-18), 29.75 (C-19), 36.10 (C-20), 18.28 (C-21), 34.95 (C-22), 31.29 (C-23), 156.83 (C-24), 33.76 (C-25), 21.85 (C-26), 21.98 (C-27), 19.27 (C-28), 15.12 (C-29), 25.39 (C-30), 105.92 (C-31'), 21.31 ($\underline{CH_3}$-CO), 170.95 (CH_3-$\underline{CO}$).

Cycloartobiloxanthone (2): dark yellow solid; mp 271-273 °C (Lit. 270 °C) [12]; IR (KBr) υ_{max} cm^{-1}: 3434 (brs), 2976, 1650, 1476, 1358, 1272; EIMS m/z (rel. int.): 434 $[M]^+$, 421, 419, 391, 377, 361, 347, 332, 293, 203, 189, 177, 152, 135, 105, 91, 77, 69, 54. ^1H NMR and ^{13}C NMR data (Table 1).

Table 1. ^{1}H NMR and ^{13}C NMR data for **2** (400 and 100 MHz, acetone-d_6)

No.	^{1}H (δ)	^{13}C (δ)	HMBC correlations
2	-	161.4	-
3	-	112.7	-
4	-	181.4	-
4a	-	105.3	-
5	-	162.6	-
6	6.11 (1H, s)	99.9	C-5, C-7, C-8, C-4a
7	-	159.5	-
8	-	101.8	-
8a	-	152.0	-
9	6.90 (1H, d, *J*= 10.0 Hz)	115.9	C-7, C-8a, C-11
10	5.65 (1H, d, *J*= 10.0 Hz)	127.9	C-8, C-11
11	-	78.7	-
12	1.43 (3H, s)	28.4	C-10, C-11, C-13
13	1.43 (3H, s)	28.2	C-10, C-11,C-12
14	2.34 ($1H_b$, t, *J*= 15.6 Hz) 3.19 ($1H_a$, dd, *J*= 15.6, 7.3 Hz)	20.3	C-2, C-3, C-4, C-15, C-2' C-2, C-3, C-15, C-16
15	3.40 (1H, dd, *J*= 15.6, 7.3 Hz)	47.5	C-14, C-16, C-17, C-13, C-2'
16	-	93.7	-
17	1.31 (3H, s)	22.8	C-15, C-16, C-13
18	1.63 (3H, s)	28.2	C-15, C-16, C-17
1'	-	104.9	-
2'	-	133.7	-
3'	-	137.9	-
4'	-	146.9	-
5'	6.39 (1H, s)	105.3	C-1', C-3', C-4', C-6'
6'	-	151.5	-
1-OH	13.36 (1-OH, s)	-	-

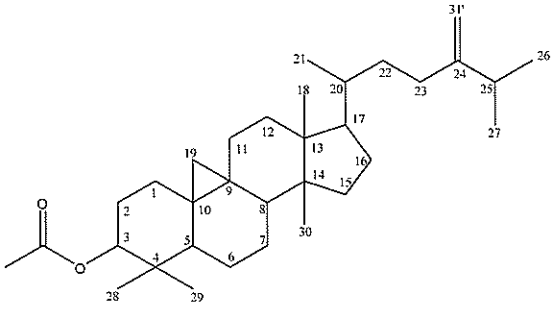

Compound **1**

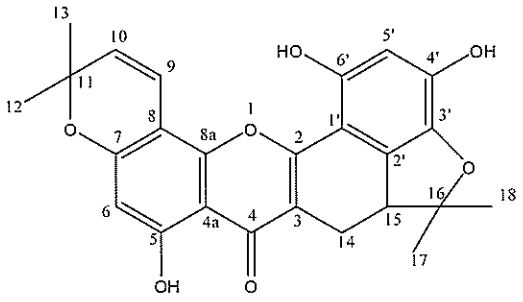

Compound **2**

RESULTS AND DISCUSSION

Compound **1** was obtained from the ethanol extract as a white solid with mp 116-119 °C (Lit. 114-117 °C) [11]. The compound showed signals corresponding to a cyclopropane ring, characteristic of a cycloartane skeleton in the NMR spectrum. It gave a molecular mass of 482 which corresponded to the molecular formula $C_{33}H_{54}O_2$.

The ^{13}C NMR assignment of **1** was made by performing HMQC and DEPT NMR experiments and by comparison with the corresponding data of **1** from *Euphorbia broteri* [11]. The ^{13}C NMR spectrum also showed a total of 33 resonances, comprising eight methyls, twelve methylenes, six methines and seven quaternary carbon atoms which are in agreement with the molecular formula.

Based on literature search, this is the first isolation of 24-methylenecycloartenyl acetate (**1**) from this *Artocarpus* species. This compound was further confirmed by comparison of spectroscopic data with literature values [11].

Compound **2** was purified as a least polar yellow pigment with R_f value 0.39 in $CHCl_3$/ Me_2O (4 : 1), mp 271-273 °C (Lit. 270°C) [12]. Mass spectrometry revealed a $[M]^+$ at m/z 434 and analysed for the molecular formula $C_{25}H_{22}O_7$. The IR spectrum showed hydroxyl and xanthone carbonyl absorptions at 3434 and 1650 cm^{-1}, respectively.

The ^{1}H NMR spectrum of **2** exhibited a low field singlet signal for a chelated hydroxyl group at δ 13.36 (1-OH). The superimposed singlet at δ 1.43 (6H, s) indicated two chromene methyl groups, together with two doublet signals at δ 6.90 (1H, d, J = 10.0 Hz) and δ 5.65 (1H, d, J = 10.0 Hz), each due to olefinic

protons indicating the presence of a 2,2-dimethyl chromene. Other than that, the two singlet signals at δ 6.11 and δ 6.39 are assigned to H-6 and H-5', respectively. Furthermore, the upfield singlet signals at δ1.31 (3H, s, H-17) and δ 1.63 (3H, s, H-18) were respectively attributed to two tetrahydrofuran methyl groups.

The ^{13}C NMR spectrum showed one signal of a conjugated carbonyl group at δ181.4, signals of twelve substituted aromatic carbons at δ 161.4 (C-2), δ 112.7 (C-3), δ 105.3 (C-4a), δ 162.6 (C-5), δ 159.5 (C-7), δ 101.8 (C-8), δ 152.0 (C-8a), δ 104.9 (C-1'), δ 133.7 (C-2'), δ 137.9 (C-3'), δ 146.9 (C-4'), and δ 151.5 (C-6') which were assigned accordingly based on information from the HMQC experiment. Meanwhile, two signals at δ 99.9 and δ 105.3 were assigned to two protonated aromatic carbons which are C-6 and C-5' respectively.

The DEPT spectrum showed the presence of 25 carbons which consisted of four methyl carbons, one methylene carbon, four methine carbon and 16 quartenary carbons. The signal for the carbonyl group at δ 181.4 was assigned to C-4.

In the HMBC spectrum, the singlet at δ 6.11 gave cross peaks with four carbon signals at δ 105.3, δ 162.6, δ 159.5 and δ 101.8, which further confirmed the assignment of δ 6.11 to H-6. Besides that, the location of the two tetrahydrofuran methyl groups (17-CH_3 and 18-CH_3) were further elucidated by the long-range ^3J correlations between δ 1.63 (methyl proton at H-18) with δ 47.5 (C-15) and δ 93.7 (C-16) and δ 22.8 (C-17) via ^2J and ^3J correlations respectively. The presence of the pyrano ring attached to C-7 and C-8 was deduced from the long-range connectivity between the doublet at δ 6.90 (H-9) and δ 78.7 via a ^3J correlation and between δ 5.65 (H-10) and δ 101.8 also via a ^3J correlation in the HMBC spectrum. Hence, the signals at δ 78.7 and δ 101.8 were assigned to C-11 and C-8 respectively and δ 5.65 and δ 6.90 to H-10 and H-9 respectively. This assignment was further confirmed by the coupling between δ 6.90 and δ 5.65 in the ^1H-^1H COSY experiment. Compound **2** was therefore assigned cycloartobilixanthone **(2)**. The spectral data are summarized in Table 1.

Table 2. Cytotoxic activities of ethanol, acetone and methanol extract against HL-60 and IMR-32 cell lines.

	IC_{50} Value (μg ml^{-1})	
Compounds	HL-60	IMR-32
Ethanol extract	31.5	12.0
Acetone extract	15.0	13.0
Methanol extract	17.5	N/A

N/A= Not active

Cytotoxic activities towards the HL-60 and IMR-32 cell lines were conducted. All the crude extracts indicated cytotoxicity towards both cell lines. The acetone extract gave LC_{50} values of 15.0 μg/mL and 13.0 μg/mL towards the HL-60 and IMR-32 cell lines respectively. The ethanol extract on the other hand gave a much lower LC_{50} value of 12.0 μg/mL towards the IMR-32 cell line. However, the methanol extract showed a slightly higher LC_{50} value of 17.5 μg/mL towards the HL-60 cell line. The cytotoxic results of the crude extracts are summarized in Table 2.

Acknowledgements – The authors wish to thank Associate Professor Dr Jegak Uli for collection of plant samples and the Ministry of Higher Education for financial support under the FRGS research fund.

REFERENCES

1. Wang Y., Xu K., Lin L., Pan Y.J. and Zheng X.X. (2007) Geranyl flavonoids from the leaves of *Artocarpus altilis*. *Phytochemistry* **68**: 1300-1306.
2. Amarasinghe N.R., Jayasinghe L., Hara N. and Fujimoto Y. (2008) Chemical constituents of the fruits of *Artocarpus altilis*. *Biochemical Systematics and Ecology* **36**: 323-325.
3. Altman L.J. and Zrro S.W. (1976) Sterols and triperpenes from the fruit of *Artocarpus altilis*. *Phytochemistry* **15**: 829-830.
4. Hakim E.H., Achmad S.A., Juliawaty L.L., Makmur L., Syah Y.M., Aimi N., Kitajima M., Takayama H. and Ghisalberti E.L. (2006) Prenylated flavonoids and related compounds of the Indonesian *Artocarpus* (Moraceae). *Journal of Natural Medicine* **60**: 161-184.
5. Wei B.L., Weng J.R., Chiu P.H., Hung C.F., Wang J.P. and Lin C.N. (2005) Anti-inflammatory flavonoids from *Artocarpus heterophyllus* and *Artocarpus communis*. *Journal of Agriculture Food and Chemistry* **53**: 3867-3871.
6. Toshio F., Kazue S., Taro N. and Hiroshi S. (2003)

Antinephritis and radical scavenging activity of prenylflavonoids. *Fitoterapia* **74**: 720-724.

7. Lin C.N., Lu C.M., Lin H.C., Fang S.C., Shieh B.J., Hsu M.F., Wang J.P., Ko F.N. and Teng C.M. (1996) Novel antiplatelet constituents from Formosan Moraceous plants. *Journal of Natural Product* **59**: 834-838.
8. Shimizu K., Kondo R., Sakai K., Buabarn S. and Dilokkunanant U. (2000) A geranylated chalcone with 5α-reductase inhibitory properties from *Artocarpus incisus*. *Phytochemistry* **54**: 737-739.
9. Patil A.D., Freyer A.J., Killmer L., Offen P., Taylor P.B., Votta B.J. and Johnson R.K. (2002) A new dimeric dihydrochalcone and a new prenylated flavone from the bud covers of *Artocarpus altilis*: potent inhibitions of cathepsin K. *Journal of Natural Product* **65**: 624-627.
10. Tati S., Sjamsul A.A., Norio A., Euis H.H., Mariko K., Hiromitsu T. and Koichi T. (2001) Artoindonesianin L, a new prenylated flavone with cyctotoxic activity from *Artocarpus rotunda*. *Fitoterapia* **72**: 912-918.
11. Teresa J.D.P., Urones J.G., Marcos I.S., Basabe P., Cuadrado M.J.S. and Moro R.F. (1987) Triterpenes from *Euphorbia broteri*. *Phytochemistry* **26**: 1767-1776.
12. Jayasinghe U.L.B., Samarakoon T.B., Kumarihamy B.M.M., Hara N. and Fujimoto Y. (2008) Four new prenylated flavonoids and xanthones from the root bark of *Artocarpus nobilis*. *Fitoterapia* **79**: 37-41.

Journal of Science and Technology in the Tropics (2009) **5**: 157-165

Radical inspirations: A review on free radical chemistry

S. H. Goh
UTAR Global Research Network, No. 13, Jalan 13/6, 46200 Petaling Jaya, Selangor, Malaysia

Received 03-12-2009; accepted 10-12-2009

Abstract This review mainly focuses on the free radical research carried out in the formative years of the Chemistry Department of the University of Malaya. It was during the period of 1950s that the important class of radical reactions was becoming to be understood as a "new organic chemistry". Rather than being the "black sheep" of reactions, radical behaviour and reactive characteristics became better understood and controllable. The chemistry of free radicals has now provided important information to many industrial processes (notably in the manufacture of polymers, chemicals and synthetic drugs), ways to combat undesirable and ravaging effects (e.g. chlorine, CFC and lipid oxidation) and further promotes further development for biology and medicine (nitric oxide, some antibiotics and natural antioxidants). Details on radical and singlet/triplet carbene chemistry are given, including peroxide decomposition, singlet/triplet carbenes, metal-carbenes (carbenoids), radical cyclisations, P450 oxidation of aromatic hydrocarbon carcinogens, chain-breaking antioxidants such as tocotrienols, and radical mechanisms in controversially unexplained reactions.

Keywords radicals – carbenes – nitric oxide – aromatic hydrocarbon carcinogenesis – cyclisations – antioxidants – tocotrienols – radical mechanisms

INTRODUCTION

This review is based on the lecture delivered at the Symposium of Science, Oct 25th 2008, Kuala Lumpur, in honour of Rayson L. Huang on his 88th birthday. The chemistry of free radicals had been the focus of many researchers at the University of Malaya Chemistry Department for a substantial period of time since the establishment of the department in Kuala Lumpur, culminating in the publishing of the book "Chemistry of Free Radicals" [1]. Originally published by Edward Arnold, translated copies in Chinese were later found to be in wide circulation in mainland China.

In the early 1950s, a free radical was just perceived as a chemical curiosity with an unpaired electron and attendant high reactivity. In many ways the radical species was viewed as a totally different reactive entity at that time compared to the better understood ions in ionic reactions of organic chemistry and thus provided for a "new organic chemistry" or a second class of organic reactions. Being relatively neutral and can be highly reactive, the radical species is responsible for starting off uncontrolled chain reactions, sometimes leading to unexpected explosions. In a way they can be the "black sheep" of organic reactions responsible for many unnecessary laboratory accidents.

Free radical reactions are now considered as a dominant class of chemical reactions and the free radical is now established as a species with an unpaired electron, usually reactive and able to give rise to characteristic radical-type reactions. Radicals are thus associated to transient and reactive species with the tendency to couple up (bond) or dimerise with other radicals to provide stable electron-paired products. As a general rule compounds, chemicals and living matter remain stable under terrestrial conditions when all the electrons in the molecules are paired. However, there are some exceptional radicals (e.g. natural NO, oxygen and some specially designed radicals) which can be relatively stable for various structural, steric or electronic reasons. With an unpaired electron, a radical has a spin phenomenon associated with it; hence radicals can be detected by electron paramagnetic (or spin) resonance spectroscopy. The stable oxygen molecule is a diradical (two unpaired electrons) and the two electrons in parallel spins give rise to a triplet species (Fig. 1).

Over the years many applications from controlled

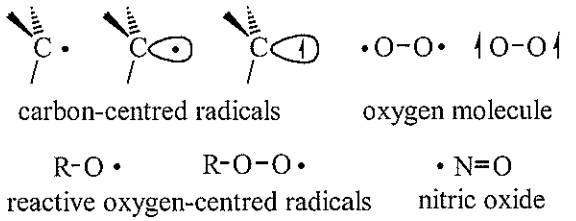

Figure 1. Representation of radical species.

radical reactions have benefited mankind with useful polymer materials, fine chemicals, synthetic pharmaceuticals, etc. The understanding of the chemistry of radicals has also opened up new avenues at the interface of biochemistry and medicine, e.g. biochemical pathways involving radicals, redox biochemistry and use of antioxidants. The small molecule NO is a natural free radical and has made profound impacts in biochemistry and medicine (R.F. Furchgott, L.J. Ignarro and F. Murad, 1998 Nobel laureates). Once an elusive "endothelium relaxing factor or EDRF", nitric oxide has been the natural signalling molecule for the relaxation of blood vessels, the agent from nitro-drugs for angina relief and the agent to be inhibited enzymatically from degradation in designed recreation drugs for males.

Radicals and radical reactions are now recognized to be widespread. For the environment, important contributions have been made in the recognition that chlorofluorohydrocarbons (CFCs) which are useful chemicals and refrigerants but because of their high stability, can unfortunately become environmental hazards due to their resistance to environmental degradation. Chlorine radical chain reactions can result in the stratosphere with initiation by ultraviolet radiation (Fig. 2). The demonstration by Paul Crutzen (shared the Nobel Prize with F. Sherwood Rowland and Mario Molina) that such reactions can deplete the earth's protective ozone layer has led to the ban on some chlorofluorocarbon compounds.

$$Cl\text{-}CF_2Cl \xrightarrow{h\nu} Cl^{\bullet} + {}^{\bullet}CF_2Cl$$

$$Cl^{\bullet} + O_3 \longrightarrow Cl\text{-}O^{\bullet} + O_2$$

$$2\,Cl\text{-}O^{\bullet} \longrightarrow Cl\text{-}O\text{-}O\text{-}Cl \longrightarrow 2\,Cl^{\bullet} + O_2$$

$$\left[\text{Net } 2\,O_3 \longrightarrow 3\,O_2\right]$$

Figure 2. Ozone destruction by chlorine radicals.

Peroxides

Peroxo-compounds were later established to be unstable compounds with weak O-O bonds which break homolytically to give highly reactive oxygen-centred radicals on thermal and photochemical decomposition. Uncontrolled induced decomposition of peroxides formed from autoxidation of common solvents such as diethyl ether has been the cause of many laboratory accidents while in oils and fats autoxidation has been the major cause of rancidity. A schematic of autoxidation may be exemplified as for oils and fats as shown in Figure. 3. After initiation of radical formation, e.g. the homolysis or cleavage of peroxide bonds by thermolysis or radiation, reactive oxygen-centred radicals are generated which start chain reactions by hydrogen abstraction to form new radicals which with air or oxygen lead to hydroperoxy radicals, and to continue further with chain reactions. The problem of radical chain reactions is that once they start they consume a large number of molecules and chain-breaking antioxidants are needed to put an end to such runaway reactions. Also, the products of autoxidation are normally peroxo- or hydroperoxy-compounds which are susceptible to cause further radical cleavages and hence the need to avoid autoxidation of useful materials as early as possible (Fig. 3). Antioxidants are thus important to break or terminate the proliferating radical chain reactions.

Peroxo-compounds range from being very explosive to completely stable chemicals. Simple alkyl and alkanoyl peroxides are explosive but di-*tert*-butyl and benzoyl peroxides, being hindered and stabilized respectively, can be homolytically decomposed controllably and used as radical initiators in the laboratory. Peroxodiphosphate salts are thermally stable and only hydrolyse by acid catalysis, i.e. ionically, and not homolytically to the peroxymonophosphate [2]. Subsequent pH-dependent decomposition of the peroxymonophosphate is

$$R\text{-}O\text{-}O\text{-}R \longrightarrow R\text{-}O^{\bullet} + {}^{\bullet}O\text{-}R$$

$$R\text{-}O^{\bullet} + -CH_2\text{-}CH{=}CH- \longrightarrow -\underset{\bullet}{C}H\text{-}CH{=}CH- + ROH$$

$$-\underset{\bullet}{C}H\text{-}CH{=}CH- + O_2 \longrightarrow -\underset{O\text{-}O^{\bullet}}{C}H\text{-}CH{=}CH-$$

$$-\underset{O\text{-}O^{\bullet}}{C}H\text{-}CH{=}CH- \longrightarrow \text{Peroxides + Hydroperoxides}$$

Figure 3. Autoxidation.

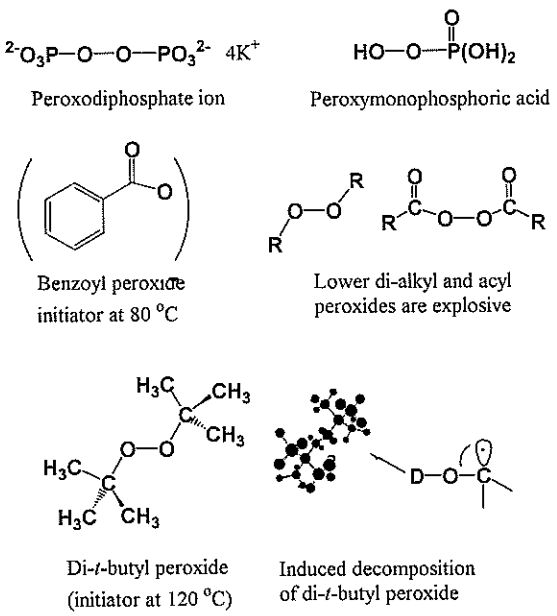

Figure 4. Peroxo-compounds, induced decomposition of di-*t*-butyl peroxide.

bimolecular by a pericyclic reaction (a third class of chemical reactions) to lead to hydrogen peroxide.

Di-*tert*-butyl peroxide is a special case of peroxide with bulky *t*-butyl groups which prevent induced decomposition that occurs in many peroxides. The compound becomes useful for photo-induced or thermal (>110 °C) generation of *t*-butoxy radicals. Only under special conditions (e.g. with a small α-hydroxyl-radical) can a measurable induced decomposition of the peroxide occur with an observed kinetic deuterium isotope effect (Fig. 4) [3, 4].

CLASSIFICATION OF REACTION TYPES

Organic chemistry was previously perceived as providing an endless proliferation of reactions which can arise from cations, anions, radicals, cyclic electronic arrays and various catalyses. By late 1960s, mainly through the efforts of R.B. Woodward (Nobel laureate, 1965), all reactions can be classified as falling into three categories: ionic, radical and pericyclic (involving electron rearrangements) reactions. The hydrolysis of peroxophosphates by water molecules alluded to above is ionic while the simplest ionic reaction could be by SN_1 bond heterolysis of trityl chloride, e.g. $Ph_3C\text{-}Cl \rightarrow Ph_3C^+ + Cl^-$, to give a triphenylmethyl carbocation. Specific examples of radical chemistry have been adequately exemplified above from bond homolysis of peroxides and their subsequent reactions. Pericylic reactions depend on

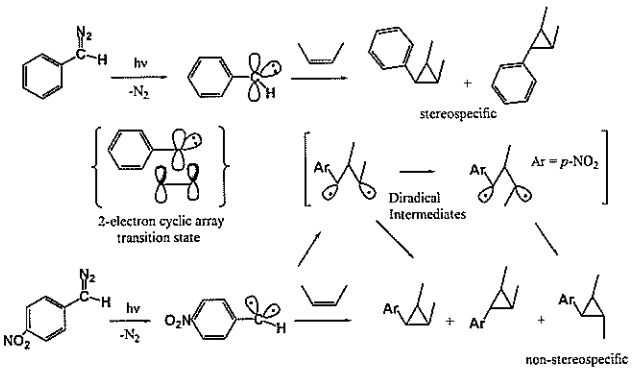

Figure 5. Singlet and triplet carbene additions.

the rearrangement of a cyclic array of electrons and can be exemplified by a singlet carbene reaction with an olefin.

Carbenes

Carbenes are very reactive species, once referred to as the most reactive species known in organic chemistry, and they can exist in as a singlet (paired electrons) or a triplet (two electrons unpaired, diradical-like) state. The photolysis of aryldiazomethanes provided arylcarbenes which can be trapped by olefins to cyclopropanes. The singlet carbene added to olefins stereospecifically in a concerted transition state in this class of pericylic reactions. The triplet can be viewed as a diradical with electrons possessing parallel spins and in the reaction with olefins proceeds through intermediate diradical species. With definite lifetimes, bond rotation in these intermediates and further ring closure provided non-stereospecific cyclopropane products (Fig. 5) [5-7]. As characteristic of reactive diradicals other allylic H-abstraction products were also provided from this reaction.

Cyclopropane formation is usually characteristic of carbene and carbenoid intermediates. Under certain conditions, however, ionic types of reactions can also provide cyclopropane products albeit with tell-tale signs of other ionic products. The example of the decomposition of diazo-compounds by acid catalysis as well as in many other undefined but possibly due to the presence of acidic catalysts, can be exemplified by phenyldiazomethane with trifluoroacetic acid in the presence of olefins. Isotopic labelling and partial D-scrambling supported the ionic mechanism of reaction (Fig. 6) [8, 9].

In general, the diversity of chemical reactions can broadly be shown to fall into the three classes of reaction types: ionic, radical or pericyclic. While

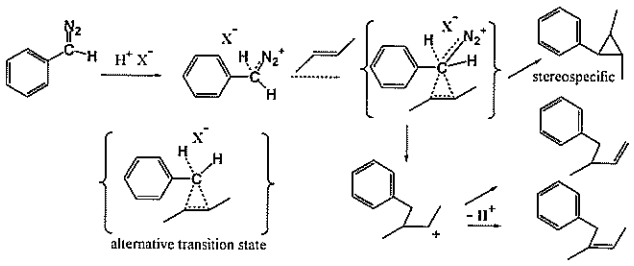

Figure 6. Ionic acid-catalysed decomposition of phenyldiazomethane.

radical reaction mechanisms became established in the late 1950s, the "no-mechanism" pericyclic reactions were only explained more than a decade later and were much dependent on the recognition of orbital symmetry in the reorganisation of electrons in a cyclic array typically found in rearrangement reactions.

Metal-carbene complexes

Whereas singlet and triplet carbenes are among the most reactive intermediates of organic chemistry, they can be tamed in the form of metal complexes where many applications have emerged. Early forays into the detection of metal-carbene complexes were on intermediates of lithium and zinc. Indeed carbenoids such as these were formed as intermediates from various precursors and could be trapped as familiar cyclopropane products among others [10-12].

Earlier work by R. Noyori (2001 Nobel laureate) achieved some degree of asymmetric cyclopropanation with metal-carbene complexes with chiral ligands but his later work using chiral phosphorus ligands managed to achieve high degrees of asymmetric hydrogenations. Since the first demonstration of relatively stable metal-carbene complexes, significant advances in metal-carbene catalytic chemistry have resulted in the recognition of the works of Y. Chauvin, R.R. Schrock and R.H. Grubbs (1995 Nobel laureates). Indeed, apart from metal-complexing, *N*-stabilized heterocyclic carbenes have been made as stable crystalline compounds and popularised since 1991 [13].

RADICAL CYCLISATIONS

Cyclisation reactions can result from the three main classes of reactions but it has been in the realm of radical chemistry that formation of 5-membered rings has been commonly found whereas 6-membered rings are more characteristic of cationic reactions. Radical cyclisations to create 5-membered rings were later much employed in synthetic chemistry.

One of the more curious examples of an undetermined mechanism was the dehalogenation of aryl halides with lithium aluminium hydride. The hydride is better known to function ionically as a nucleophilic hydride in most reactions yet in the case of *o*-allyloxyphenyl halides reductions they occur to provide typically a 5-membered ring product. To study if the mechanism involved hydride displacement, carbanion or free aryl radical several experiments were carried out. Initial experiments showed that experimental conditions were poorly reproducible which could be indicative of (but not necessarily) a radical reaction but may have been dependent on initiators, in this case from environmental or unnoticed impurities. Reproducible reductions were only found by using photo-initiation of *t*-butyl peroxide to provide *t*-butoxy radicals as initiators. Indeed the bromide and iodide compounds could be smoothly converted to 5-membered ring compounds as expected from the generation of an initial aryl radical cyclisation mechanism (Fig. 7).

Once the radical nature of the lithium aluminium hydride reaction had been resolved, it had been possible to design experiments to directly observe the radical intermediate by electron paramagnetic resonance spectroscopy. As expected at liquid nitrogen temperatures, the photo-initiated reactions produced a 5-membered ring cyclised intermediate radical (>CH-CH_2·) with simple doublet of triplet hyperfine structure. The precursor aryl radical presumably cyclised rapidly and 5-membered radical cyclisations are noted to be among the fastest "clocks" at ~10^{-5} sec,

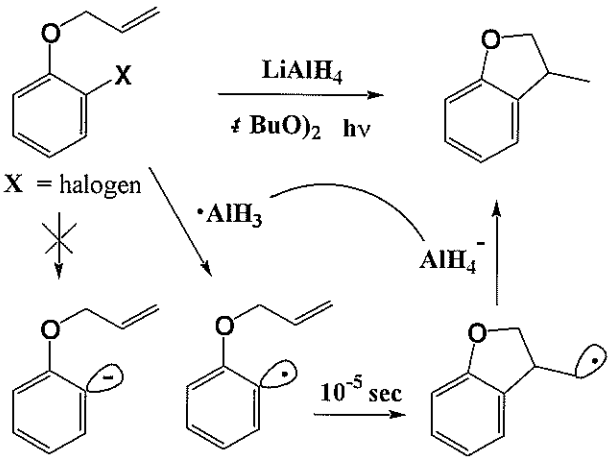

Figure 7. Hydride dehalogenations of aryl halides.

exceeded only by the cyclopropane radical cyclisation "clock" at ~10^{-7} sec.

Radical induced dehalogenations of aryl halides, including fluorides, can be achieved by the methodology found. The intermediate aluminium-centred radical must have a high affinity towards halides. Of lesser efficiency some boron hydrides could also effect similar dehalogenations [14-16].

A number of natural products contain 5-membered rings which may or may not be the result of radical cyclisations. Prostaglandin derivatives and their intermediates are probably the best examples of natural products from radical precursors. There are many complex natural products with 5-membered rings which perhaps could benefit from synthetic radical methodology; in fact in some cases radical-cyclisations had to be gainfully employed. Several advantages of synthetic radical methodology may be cited: 5-member rings can present a great difficulty using ionic reagents, the radical cyclisation reaction is highly specific, polar functionalities remain untouched by radicals, and useful radical initiators are now available.

RADICALS IN BIOLOGY

Radicals play a major role in reactions of organic chemistry and they are likewise important in almost all biological systems. Redox systems can involve one-electron processes which are essentially radical in nature. The cytochrome P450 oxygenase enzyme contains metallo-iron and the chrome pigment absorbing at 450 nm is capable of oxidising various substrates

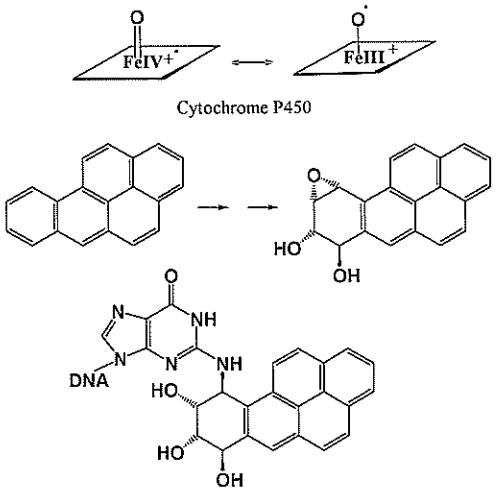

Figure 8. Cytochrome P450 oxidation of aromatic hydrocarbons in cancer induction.

including activation of C-H bonds and epoxidation of aromatics. One important function of the enzymes is the detoxification of undesirable chemicals. The epoxidation of aromatic hydrocarbons is one such reaction but could cause their activation to carcinogens. Interestingly, the epoxidation of the powerful polycyclic aromatic hydrocarbon carcinogen, benzopyrene, led to an ultimate carcinogen diol epoxide. It has now been established over the years that aromatic hydrocarbons are activated by epoxidation to the ultimate carcinogenic intermediates which presumably can subsequently react with nucleophilic centres of DNA in the carcinogenic process. The oxidation of benzopyrene to the diol-epoxide is illustrated (Fig. 8); the large protein fragment is omitted in cytochrome P450 as the biochemical reagent essentially is a radical at the active site [17, 18].

Radicals have played important roles in biology and medicine in controlled biochemical pathways. Nitric oxide, described earlier as an important molecule for blood vessel relaxation, play other roles, e.g. as cytotoxic agent against foreign bodies. Quinone-semiquinone pairs are involved in redox pathways. Many natural products are also involved in the multitude of biochemical reactions. Dihydroxyindole and gambirine alkaloids are readily oxidizable compounds with cytotoxic and bioactive activities. Notably are the numbers of antioxidant natural compounds which have vital roles to play as vitamins, antioxidants or other functions [19].

ANTIOXIDANTS

Among the plethora of natural products that have generated considerable interest are the antioxidants which originate naturally from fruits, vegetables and herbal plants. These compounds encompass many classes of phenolic compounds (polyphenols, flavonoids, xanthonoids, curcuminoids, and vitamin E analogues) and also other minor classes such as carotenoids, ascorbic acid and some sulphur compounds [19]. Compounds which can act as radical sinks or as radical chain breakers can function as antioxidants. The phenolic compounds are effective antioxidants, capable of terminating radical chain reactions and common ones are used as vitamins and antioxidant supplements. Tocopherol and tocotrienol analogues (e.g. from palm oil and natural rubber) and other examples of common phenolic antioxidants

CONCLUSION

BFR was relatively less habitable than the adjacent SLFR during the periods of study. This was primarily due to BFR being partially cultivated with orchard plantations and prevailing construction work, during which the habitat was constantly subjected to flow of human and machinery. BFR recorded a total of 160 species (or 60.6%) out of all the species found in the survey while SLFR recorded 224 species (or 84.8%). All the species identified are common and are widely distributed throughout Peninsular Malaysia. None of the species identified is threatened or endangered though a small number are classified as 'Protected' or 'Totally Protected' under the Protection of Wildlife Act 1972 (Act 76) 1994.

The fact that 60.6% of 264 vertebrate species was still recorded in the BFR during a period of intense disturbance indicates that the various habitat types (riparian, mixed scrub, regenerated forest, crystal clear riverine system) could still sustain the survival of small vertebrates. With the forest now preserved as a catchment area, it is possible that the forest with time could regenerate into a good secondary forest. We propose some recommendations below.

Forest reclamation

The extension of the orchard plantations should be discouraged. This is to enable the fringe habitat to regenerate faster. Tapping of the forest stream and river water for agriculture and orchard plantations should also be discouraged, so that forest aquatic and semi-aquatic vertebrates could be sustained.

Wildlife law enforcement

Apart from hunting of animals in the BFR and SLFR by Orang Asli for food, hunting by outsiders and orchard farmers for wild pigs and other medium sized animals, like mouse deer, porcupines, civet cats was quite common as evidenced by the empty cartridges found in the BFR. During our visits there, we observed shot specimens of two species of mouse-deer (*Tragulus napu, T. javanicus*) and the Rhinoceros hornbill (*Buceros rhinoceros*). To maintain the vertebrate species diversity in the two forest areas, strict law enforcement and monitoring is needed.

Acknowledgements – We dedicate this study to the late Orang Asli friend of ours, Ti'ee anak Sipang who passed away last month in the Gombak Forest Reserve. Ti'ee anak Sipang like his late father Sipang Ecoin (died in 1975) had been working with the senior author for nearly four decades in field activities, and through their mentoring, the senior author had gained a wealth of zoological knowledge (ecology of small mammals) during his life time. To Hamid anak Busu and Halim anak Kisom who always accompanied our field activities, we express our gratitude to them.

We are also grateful to Kelvin K.P. Lim and T.M. Leong of the Raffles Museum of Biodiversity Research, National University of Singapore for the confirmation of the amphibian and reptile species. To the Director-General of the Department of Wildlife and National Parks, Kuala Lumpur, Dato' Abdul Rasid bin Samsudin for permission to access the Department's vertebrate collections for comparison of our materials and allowing us to deposit all voucher specimens in their museum, for which we are grateful.

We also wish to thank Oi Soo Chin (Malaysian Environmental Consultants Sdn Bhd) for her assistance in the preparation of the final draft and Lim Meng Tsai (MEC) for his assistance in suggesting improvements for the final draft of this manuscript.

REFERENCES

1. Lim B.L. and Heyneman D. (1965) Systematic and distribution studies of helminthes of Malaysian mammals. *Medical Journal of Malaya* **20**: 54 (poster).
2. Lim B.L., Mohd. Khan M.K., Chai K.S. and Lim C.C. (2008) Pre-logging survey of herpetological and mammal fauna at Lakum Forest Reserve, Raub, Pahang, Malaysia. *Journal of Science and Technology in the Tropics* **4**: 99-116.
3. Medway Lord and Wells D.R. (1976) *The birds of the Malay Peninsular* Vol V. H.F. and G. Witherby and Penerbit Universiti Malaya, London & Kuala Lumpur.
4. Jeyarajasingam A. and Pearson A. (1999) *A field guide to the birds of West Malaysia and Singapore*. Oxford Univ. Press, London.
5. Wells D.R. (1999) *The birds of the Thai-Malay Peninsula Vol. 1 Non-passerines*. Academic Press, London.
6. Robson C. (2000) *A field guide to the birds of South East Asia*. New Holland Publishers (UK) Ltd., London.
7. Norsham Y., Norhayati A., Faud Shariff, Nordin M. and Lim B.L. (2005) Pre-logging survey on vertebrate fauna species diversity at Sungei Weng Sub-catchment, Ulu Muda Forest Reserve, Kedah: Amphibian fauna. *Malayan Nature Journal* **57**: 47-55.
8. Kiew B.H. (1987) An annotated checklist of the herpetofauna of Ulu Endau, Johore, Malaysia. *Malayan Nature Journal* **41**: 413-423.

(e.g. curcumin from turmeric and EGCG from tea) are given in Figure 9.

Tocotrienols

Tocotrienols have generated exceptional interest because of three reasons: they are actually produced in enormous quantities in natural rubber latex and palm oil, especially in the S. E. Asian region. They are important lipid soluble antioxidants and apart from Vitamin E activity they also possess several other useful medicinal properties including neuro-protection.

As antioxidants, tocotrienols are better antioxidants than the more common saturated analogues (α-tocopherol from synthetic sources and soybean oil distillate). The radical derived from its oxidation can be readily observed by electron paramagnetic resonance (Fig. 10) [20]. The stability and inactivity of the radical form the basis of the chain-breaking antioxidant action for oils and fats and natural latex/rubber and thus prevent the ravages of oxidative degradation. Within the human lipid system, the smaller tocotrienol molecules (when folded) are more mobile than the tocopherols and accounts in part to their better potency. However, tocotrienols suffer from faster loss by metabolism whereas α-tocopherol has the selective tendency to be accumulated in the liver. α-Tocopherol radicals can also be reductively recycled by vitamin C in the human system.

It is increasingly clear from research findings that tocotrienols can act more than just good antioxidants as more useful bioactivities have now been discovered. In preventive medicine antioxidants have been stressed as useful against cardiovascular diseases as well as cancer. Prevention of oxidation of lipoprotein cholesterol particles with which tocotrienols are associated, could be the main function even though the reduction of cholesterol levels have been observed on some individuals. More interestingly neuro-protective mechanisms have been unraveled and could be potential for useful drugs. The earliest study of tocotrienols against induced carcinogenesis had led to later findings on apoptotic properties against cancer cells [21]. The useful bioactivities of tocotrienols may be due to their structures showing partial similarities to steroids as shown in Figure 11.

Tocotrienols isolated from palm oil had provided some useful chemistry. The gamma isomer when

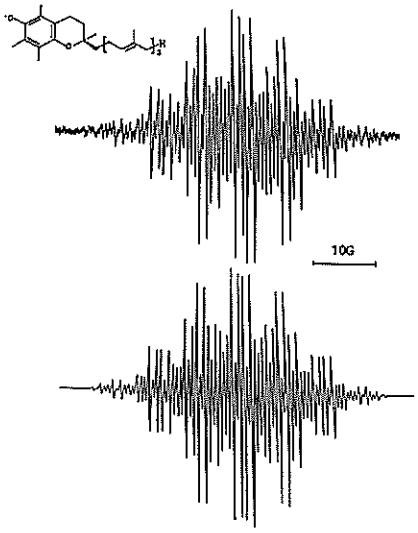

Figure 10. α-Tocotrienoxy radical and simulated spectra.

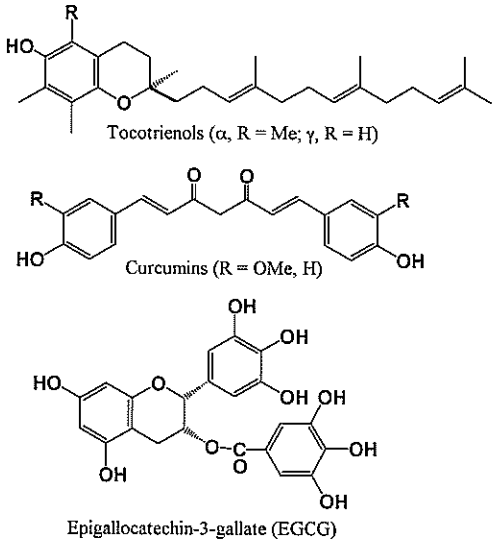

Figure 9. Naturally occurring phenolic antioxidants.

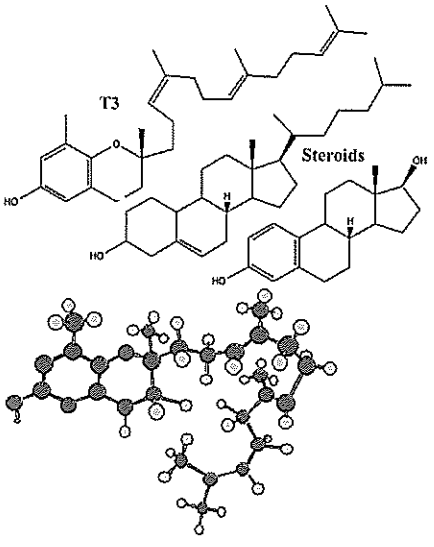

Figure 11. Structures of tocotrienols and steroids.

oxidised provided the radical intermediate which dimerised to biphenyl derivatives and because of the inherent hindered rotation provided two distinct isolable diastereoisomers. Since the natural γ-tocotrienol has the *R*-configuration much like natural α-tocopherol, dimerisation will create "biphenyl-type" structures with hindered rotation and therefore provide *R,R,R*- and *R,S,R*-diastereoisomers (Fig. 12). These were isolable chromatographically but they isomerised over time and the structures had to be quickly determined by NMR techniques [22].

RADICAL MECHANISMS

There are many reactions which may apparently have mechanisms that may not be definitive as radical or ionic. One such reaction was the reaction of *p*-nitrobenzyl chloride with sodium hydroxide which definitely produced the carbanion intermediate because of the relative acidity of the compound. Further reaction may be rationally expected to proceed by SN_2 or even by alpha-elimination to a carbene and the product could be the dinitrostilbene. However the kinetics was more closely that of a second-order reaction rather than first order (for a carbene or reaction with air). Furthermore products were indicative of radical formation such as the formation of an acetylenic product apart from stilbene. Apparently the reaction was better described as an electron transfer from carbanion to the neutral precursor and products were formed from further reactions of the radicals produced [23-27].

In many instances it can be much more obvious that radical intermediates were involved as in the action of organic halides by some organometallic reagents. At a time when there was interest in the stability of bridgehead radicals, the generation of such from bridgehead halides by pentacyanocobaltate provided these intermediates and also the organocobalt-bridgehead compounds (Fig. 13). However in the case of chromium (II) reductions of organic halides the radical and ionic natures of the intermediates were less definite [28-30].

Another intriguing reaction was that of lithium diisopropylamide with some organic halides which from theoretical predictions should not favour electron-transfer but yet showed some unexplained possibly radical characteristics. Careful experimentation using various hindered and deuterated dialkyl amides on a chosen substrate trityl chloride provided some definitive results. Firstly the trityl radical as well as the typical peroxide product with air were observed which verified that a radical reaction was possible. The trityl radical was interesting, especially its high stability and its dimeric form (rather than the wrong conclusions from very early Gomberg chemistry). The more hindered perchlorotrityl radical was even more remarkable as being totally stable and existing in separable enantiomeric *R* and *S* forms (propeller-shaped). In the lithium dialkylamide-trityl chloride reaction the kinetics was first order in the presence of excess base, an indication that the SN_1 dissociation to trityl carbocation had occurred before the electron-transfer step can rationally take place (Fig. 14).

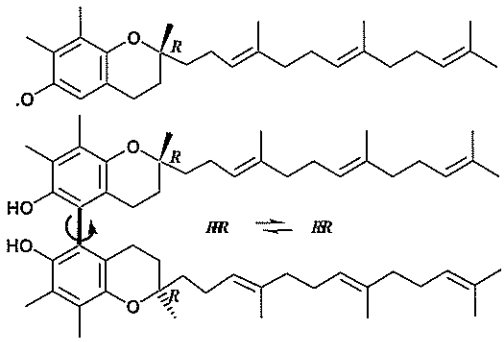

Figure 12. γ-Tocotrienoxy radical and dimers in diastereomeric forms.

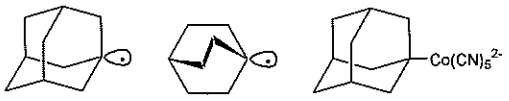

Figure 13. Bridgehead radicals and organometal intermediates.

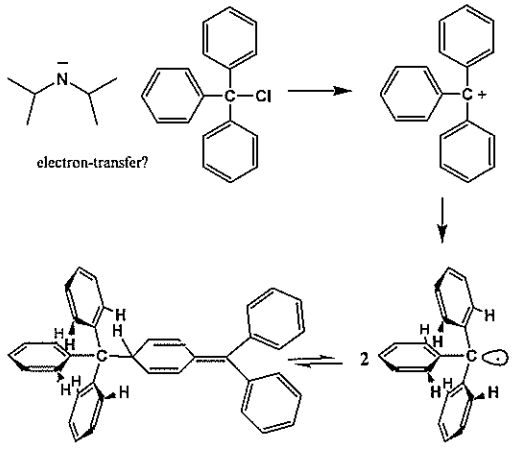

Figure 14. Radical formation from lithium dialkylamide and trityl chloride.

RETROSPECT AND FUTURE PROSPECTS

Much of the understanding of classes of organic reactions is now in place and free radical reactions form a major class. The theoretical aspects and their characteristics have now been applied wherever the situation may arise, e.g. initiation, polymerization, oxidation-reduction, radical cyclisations, use of metal-radicaloids and natural antioxidants. Chemical and industrial aspects of radical chemistry have been well documented, even though much of environmental sulphur and toxic metal chemistry will need attention. A lot still remains to be understood in biology and medicine in terms of radical processes as well as the action of radicals on biological molecules. Some of nature's processes involving one-electron-transfer and unique metal-radicaloid systems have still to be properly unravelled before synthetic analogues can be designed. Some examples include C-H activation, one-electron transfer steps in photosynthesis, enzymatic cyclisations/reactions and nitrogen fixation.

The limelight had fallen on metal-carbenes catalysts for synthesis for which Nobel prizes have been awarded. Metal-carbenes and metal-radicaloids are capable of further surprises in producing novel chemistry. Atom transfer radical polymerisation has evolved to provide a major living/controlled radical methodology to precision polymer production. Several named catalysts for C-C couplings no doubt will be highlighted and evaluated in the near future. Over the years reactive carbenes have been made into stable entities by using steric and electronic control, e.g. stable *N*-heterocyclic-carbenes, which can be employed as catalysts in organometallic synthetic applications.

REFERENCES

1. Huang R.L., Goh S.H. and Ong S.H. (1974). *The Chemistry of Free Radicals*, Edward Arnold Publishers (London), 244 pp.
2. Goh S.H., Heslop R.B. and Lethbridge J.W. (1966) Hydrolysis of peroxophosphates. *J. Chem. Soc.(A)*, 1302-1305.
3. Goh S.H. and Ong S.H. (1970) The Induced Decomposition of *t*-butyl peroxide in solution. Part II. A Kinetic Study. *J. Chem. Soc. (B)*, 870-872.
4. Goh S.H. (1972) The induced decomposition of *t*-butyl peroxide. A nuclear magnetic resonance study. *J. Org. Chem.* **37:** 3089.
5. Goh S.H. (1971). Nitrophenylcarbenes. Part 1. The catalytic and photolytic decomposition of α-diazo-3-nitrotoluene in the presence of olefins. *J. Chem. Soc. (C)*, 2275.
6. Goh S.H. (1972) Nitrophenylcarbenes. Generation and reactions with *cis*-butene. *J. Chem. Soc. (C)*, 512.
7. Goh S.H. and Gian H.L. (1979) *Triplet State Nitrophenylcarbenes. J. Chem. Soc. Perkin I*, 1625-1627.
8. Closs G.L., Goh S.H. and Moss R.A. (1966) Formation of cyclopropanes in the acid-catalysed decomposition of phenyldiazomethanes in olefins. *J. Amer. Chem. Soc. Communications* **88**: 364.
9. Goh S.H. and Closs G.L. (1974) Acid-induced reaction of aryldiazomethanes with olefins. Mechanism of reaction *J. Org. Chem.* **28:** 381-384.
10. Goh S.H., Closs L.E. and Closs G.L. (1969). Carbenoid decompositions of aryldiazomethanes with lithium and zinc halides. A convenient synthesis of cyclopropanes. *J. Org. Chem.* **34:**24-28.
11. Goh S.H. and Goh L.Y. (1970). α-halobenzylzinc halides. *J. Organometal. Chem.* **23:** 5-8.
12. Chan K.C., Goh S.H. and Gian H.L. (1976). Dicarbenes. Dicarbenoid species from the reaction of 1,3-bis(diazomethyl)benzene with zinc halides. *Aust. J. Chem.* **29**:1699-1702.
13. Arduengo A.J., Harlow R.L and Kline M. (1991) A stable crystalline carbene. *J. Amer. Chem. Soc.* **113:** 361-363.
14. Beckwith A.L.J. and Goh S.H. (1983) Intermediacy of aryl radicals and arylmetal compounds in the reductive dehalogenation of halogenoarenes with Lithium Aluminium Hydride, *J. Chem. Soc. Chem. Comm.* 905-906.
15. Beckwith A.L.J. and Goh S.H. (1983) Homolytic reductive dehalogenation of aryl and alkyl halides by lithium aluminium hydride, J. Chem. Soc. Chem. Comm. 907.
16. Goh S.H. and Choy C.K. (1990) Fragmentation of arylalkoxyalane radical anions: Deoxygenation of aralkanols and facile reduction of cinnamyl alcohol via cyclisation of a cinnamyloxyalane radical anion. *Tetrahedron Letters* **31**(4): 553-554.
17. Goh S.H. and Harvey R.G. (1973) Arene oxides of carcinogenic aromatic hydrocarbons. *J. Amer. Chem. Soc.* 95: 242-243.
18. Harvey R.G., Goh S.H. and Cortez C. (1975)

K-ring oxides and related oxidized metabolites of carcinogenic aromatic hydrocarbons. *J. Amer. Chem. Soc.* **97:** 3468-3470.

19. Chuah C.H., Mok J.S.L., Liew S.L., Ong G.H.C., Yong H.S. and Goh S.H. (2007) *101 Plants to fight cancer.* Sarawak Biodiversity Centre Publications, 208 pp.
20. Goh S.H., Hew N.F., Ong A.S.H., Choo Y.M. and Brumby S. (1990) Tocotrienols from Palm oil: Electron spin resonance spectra of tocotrienoxy radicals. *J. Amer. Oil Chem. Soc.* **67**(4): 250-253.
21. Goh S.H., Hew N.F., Yadav M. and Norhanom A.W. (1994) Anti-tumour promoting activity of tocotrienols from palm oil. *Internat. Jour. Cancer* **57:** 529-531.
22. Goh S.H., Hew N.F. and Lee M. (1992) Stereochemistry of bichromanyl dimers from γ-tocopherol and γ-tocotrienol. *Tetrahedron Letters* **33:** 4613-4616.
23. Closs G.L. and Goh S.H. (1972) Nitrophenylcarbenes. Part II. The generation and reactions of 4-nitrophenylcarbenes. The nature of the reactions of 4-nitrobenzyl derivatives with sodium hydroxide. *J. Chem. Soc. Perkin I*, 2103-2106.
24. Closs G.L. and Goh S.H. (1972) Nitrophenylcarbenes. Part III. Kinetics of the decomposition of 4-nitrobenzyl chloride and dimethyl-4-nitrobenzylsulphonium ion in sodium hydroxide. A reinvestigation, *J. Chem. Soc. Perkin II*, 1473-1376.
25. Chan K.C., Goh S.H., Teoh S.E. and Wong W.H. (1974) Radical nature of the reaction of 4-nitrobenzal chloride with sodium hydroxide. *Aust. J. Chem.* **27:** 421-424.
26. Goh S.H. and Kam T.S. (1978) Kinetics and mechanism of the reaction of 4-nitrobenzylidene dichloride with sodium hydroxide. *J. Chem. Soc. Perkin II*, 648-650.
27. Goh S.H. and Kam T.S. (1981) Base-induced reactions of nitrobenzal chlorides, *J. Chem. Soc. Perkin I*, 423-426.
28. Goh S.H. and Goh L.Y. (1972) 1-Adamantylpentacyanocobaltate (III), *J. Organometal. Chem.* **43:** 401-403.
29. Goh S.H. and Goh L.Y. (1980) Reactivity of bridgehead halides with pentacyanocobaltate (II), *J. Chem. Soc.* Dalton 1641-1943.
30. Loo C.T., Goh L.Y. and Goh S.H. (1972) Formation and kinetics of the decomposition of monoaquobis(ethylenediamine)-chromium(III) complexes, *J. Chem. Soc. Dalton* 585-587.

9. Berry P.Y. (1975) *The amphibian fauna of Peninsular Malaysia*. Tropical Press, Kuala Lumpur.
10. Tweedie M.W.F. (1983) *The snakes of Malaya 3rd ed.* Singapore National Printers (Pte) Ltd., Singapore.
11. Lim B.L. and Das I. (1999) *Turtles of Borneo and Peninsular Malaysia*. Natural Hist. Publ. (Borneo), Kota Kinabalu.
12. Grismer L.L. (2008) A revised and updated checklist of lizards of Peninsular Malaysia. *Zootaxa* 1860: 28-34.
13. Grismer L.L., Sukumaran J., Grismer J.L., Youmans T.M., Wood Jr. P.I. and Johnson R. (2004) Report on the herpetofauna from the Temengor Forest Reserve, Perak, West Malaysia. *Hamadryad* **29**: 15-32.
14. Medway Lord (1983) *The wild mammals of Malaya (Peninsular Malaysia) and Singapore*. Oxford University Press, Kuala Lumpur.
15. Othman S. and Lim B.L. (2000) Non-volant mammals. *Journal of Wildlife and Parks* **18**: 21-28.
16. Marsh C.W. and Wilson W.L. (1981) *A survey of primates in Peninsular Malaysian forests*. (Final report for Malaysian primate researches programme, July 1981). Universiti Kebangsaan Malaysia, Bangi and University of Cambridge, U.K.
17. Kingston T., Lim B.L. and Akbar Z. (2006) *Bats of Krau Wildlife Reserve*. Penerbit Universiti Kebangsaan Malaysia, Bangi.
18. Francis C.M. (2008) *A field guide to the mammals of South-east Asia*. New Holland Publishers (UK) Ltd., London.

Appendix 1. Amphibian and Reptile species examined and sighted in Broga and Sungai Lallang Forest Reserves, Hulu Langat during May and September 2003. Figure denotes hand caught, figure in bracket sighted, VSC, voucher specimen collected. P: Protected; TP: Totally protected; NP: Not Protected.

No.	Family/Species	Broga FR	Sg. Lallang FR	Remarks	Legal Status
	ANURA				
	AMPHIBIANS				NP
	Megophryidae				
1	*Megophrys nasuta*	1	4	Forest floor (1 VSC)	NP
2	*Xenophrys longipes*	-	1	Forest shrub (1 VSC)	NP
3	*Leptobrachium hendricksoni*	2	1	(1 VSC)	NP
	Bufonidae				
4	*Phrynoidis aspera*	4	4	Released.	NP
5	*Ingerophrynus parvus*	5	1	Forest floor near stream. (2 VSC)	NP
6	*Leptophryne borbonica*	1	4	Forest floor. (1 VSC)	NP
7	*Duttaphrynus melanostictus*	2	-	Under dead log forest floor.	NP
	Ranidae				
8	*Amolops larutensis*	3	2	Banks of fast flowing stream. (1 VSC)	NP
9	*Limnonectes blythii*	3	2	Banks of forest streams. Released.	NP
10	*L. laticeps*	15	12	Banks of forest streams. (2 VSC)	NP
11	*L. plicatellus*	2	-	Water puddles near forest stream. (1 VSC)	NP
12	*L. tweediei*	1	1	Banks of forest stream. (1 VSC)	NP
13	*Fejervarya limnocharis*	10	-	Water puddles along forest trail and bank of streams. (2 VSC)	NP
14	*Hyarana raniceps*	14	2	Leaves of plants along forest streams. (2 VSC)	NP
15	*Odorrana hosii*	2	-	Banks of forest stream. (1 VSC)	NP
16	*H. erythraea*	5	-	In pools of water near forest stream. Released.	NP
17	*H. glandulosa*	-	1	Banks of forest stream. Released.	NP
18	*H. picturata*	-	2	Banks of forest stream. (1 VSC)	NP
	Rhacophoridae				
19.	*Polypedates leucomystax*	9	1	Branches of small plants along trails. Released.	NP
20	*P. macrotis*	1	4	Tree branches near forest stream. (1 VSC)	NP
21	*P. colletti*	-	2	Tree branches along forest stream. (1 VSC)	NP